

## ABSTRACT

SUN, TIANLEI. Realizing Advanced Thin Film Micro-Electronics: Development of Corrugated Thermoelectric Generators and Stretchable Organic Semiconductors. (Under the direction of Dr. Brendan T. O'Connor)

This thesis contains two separate parts:

I: Novel thermoelectric generators design.

The global energy demand to support the modern society has been increasing rapidly along with the economic development. Increasing the energy usage efficiency is a promising approach to solve the global resource scarcity problem. Thermoelectric generators (TEG) offer a route to reuse the waste heat being generated. This work presents two thin film TEG design based on corrugated architecture. The first work focuses on optimizing the fabrication process by using heat-shrink PET and is presented as a cost-effective method that can be potentially used in large area applications. Proof of concept devices are fabricated followed by analytical and simulative exploration to explore performance optimization. Secondly, a similar woven structure that can be fabricated into fabric and power wearable electronics is considered. The performance is theoretically explored using analytical tools.

II: Stretchable polymer semiconductors.

Intrinsically stretchable semiconductors will facilitate the realization of seamlessly integrated stretchable electronics. In this thesis, we employ two different approaches to improve the stretchability of thin film semiconductor polymers. The first approach is to blend a rigid high-performance donor-acceptor polymer semiconductor poly[4(4,4dihexadecyl4Hcyclopenta [1,2b:5,4b'] dithiopen2yl) alt [1,2,5] thiadiazolo [3,4c] pyridine] (PCDTPT) with a ductile polymer semiconductor poly(3hexylthiophene) (P3HT).

Morphology and charge carrier mobility are characterized during the cyclic strain process. The second approach is to modify the elastomer substrate with UV/ozone treatment. Peeling test is used to explore the adhesion energy between thin film and oxidized substrate. Changes in surface morphology of thin film under cyclic strain, when on modified elastomer substrates, are measured with quasi in-situ atomic force microscopy. We find that the substrate tension, surface adhesion, and near surface modulus has a significant impact on film morphological stability.

© Copyright 2017 by Tianlei Sun

All Rights Reserved

Realizing Advanced Thin Film Micro-Electronics: Development of Corrugated  
Thermoelectric Generators and Stretchable Organic Semiconductors

by  
Tianlei Sun

A dissertation submitted to the Graduate Faculty of  
North Carolina State University  
in partial fulfillment of the  
requirements for the Degree of  
Doctor of Philosophy

Mechanical Engineering

Raleigh, North Carolina

2017

APPROVED BY:

---

Dr. Brendan T. O'Connor  
Committee Chair

---

Dr. Scott Ferguson

---

Dr. Jun Liu

---

Dr. Tushar K. Ghosh

## **BIOGRAPHY**

Tianlei Sun was born in Qingdao, Shandong province in China. In 2010, he graduated from University of Science & Technology Beijing with a B. S. degree in Mechanical Engineering. In 2012, he graduated from University at Buffalo SUNY with M.S degree in Mechanical Engineering. The title of his M.S thesis is “Coagulation of Oil in Water Using Sawdust and Bentonite and the Formation of a Floating Coagulated Material”. In 2013, he joined the Energy Conversion and Transport lab in NC State University under the supervision of Dr. Brendan T. O’Connor at Department of Mechanical and Aerospace Engineering. His research interest includes unconventional thermoelectric generator design and developing stretchable organic semiconductors.

## ACKNOWLEDGMENTS

Foremost, I would like to express my sincere gratitude to my advisor, Dr. Brendan O'Connor, for his invaluable, brilliant and patient guidance and mentoring throughout my doctoral studies. Without his support and encouragement, this work would not have been possible.

I thank Prof. Scott Ferguson, Prof. Jun Liu and Prof. Tushar Ghosh for serving as my committee members and for their valuable comments and suggestions during my PhD and for my thesis.

I would also like to thank all the lab mates during my PhD here for their friendliness creating a comfortable work environment and the assistance with research including: Omar Awartani, Xiao Xue, Pratik Sen, Nrup Balar, Opeoluwa Owoele, Josh Scott, Ronald Booth, Zhanrui Zhang, Ronald Booth, Eshwar Ravishankar, Runqiao Song and Dominik Reich.

Finally, I would like to dedicate to my family who supported me during my long education abroad. Thanks to my Mom and Dad for their constant love and encouragement. And to my wife Yunting, thanks for being here and company with me every day. Your support, understanding and love has made this possible.

# TABLE OF CONTENTS

LIST OF TABLES .....	vi
LIST OF FIGURES .....	vii
NOMENCLATURE .....	xv
1 Unconventional thermoelectric generators (TEGs).....	1
1.1 Introduction .....	1
1.1.1 Thermoelectric technology and device performance .....	3
1.1.2 Novel thermoelectric device design.....	5
1.2 Heat shrink formation of a corrugated thin film thermoelectric generator .....	7
1.2.1 Introduction and motivation.....	7
1.2.2 Corrugated thermoelectric module fabrication .....	11
1.2.3 Results and Discussion .....	12
1.2.4 Conclusion .....	24
1.3 Performance expectations of a woven thermoelectric generator .....	26
1.3.1 Introduction and motivation.....	26
1.3.2 Device architecture and material properties .....	30
1.3.3 Analytical model.....	31
1.3.4 Results and discussion .....	35
1.3.5 Conclusion .....	45
1.4 Summary and potential future work.....	46
1.4.1 Summary of present work.....	46
1.4.2 Suggestion for future work .....	47
2 Stretchable organic semiconductors .....	48
2.1 Introduction .....	48
2.1.1 Conductive polymer.....	48
2.1.2 Stretchable polymer semiconductors .....	50

2.1.3	Characterization methods.....	58
2.2	Stretchable Film Approach.....	67
2.3	Plastic Deformation of Polymer Blends as a Means to Achieve Stretchable Organic Transistors .....	68
2.3.1	Introduction and motivation.....	68
2.3.2	Results and discussion .....	72
2.3.3	Conclusion .....	89
2.3.4	Experimental section.....	90
2.4	The role of elastomer substrate tension, interface stiffness, and adhesion on the behavior of a stretchable polymer semiconductor.....	93
2.4.1	Introduction.....	93
2.4.2	Results and Discussion .....	97
2.4.3	Conclusion .....	111
2.4.4	Experimental Section .....	116
2.5	Summary and potential future work.....	118
2.5.1	Summary for present work.....	118
2.5.2	Suggestion for future work .....	119
REFERENCES .....		121

## LIST OF TABLES

<b>Table 1.</b> A comparison of OTFT characteristics of stretchable organic semiconductors tested on rigid test-beds after cyclic strain. The reported range in charge mobility is for 100 strain cycles, except the block copolymer approach, which is for 1 time tensile strain only.....	89
---	----

## LIST OF FIGURES

- Figure 1** Estimated U.S. Energy Consumption in 2015 <sup>2</sup> .....2
- Figure 2** Schematic of Seebeck effect and Peltier effect<sup>6</sup> .....4
- Figure 3** (a) Evolution of the maximum ZT over time <sup>7</sup>. Summary of some of best ZT for (b) p-type and (c) n-type bulk thermoelectric materials as a function of temperature <sup>8</sup> .....5
- Figure 4.** (a) Schematic illustration of the fabrication process for the corrugated TEG device, including the stack of heat-shrink PET, the adhesives, and thermoelectric couples on a polyimide substrate. The layers are all combined forming a sandwiched structure that is then thermally formed into the corrugated TEG. (b) Simplified geometric model of corrugated TEG device, with thermoelectric leg dimensions including thermoelectric thickness ( $t_{TE}$ ), length ( $L$ ), width ( $w_{TE}$ ), and stacking angle ( $\alpha$ ). (c) Photos of the corrugated TEG device before and after being thermally formed.....10
- Figure 5.** (a) Open circuit voltage ( $V_{oc}$ ) as a function of the temperature difference across the couples ( $\Delta T$ ) for various thermocouple configurations, 3 TE couples in a flat sheet, 3 TE couples in the corrugated structure, and 10 TE couples in the corrugated structure. The linear fits to the data are used to determine the average Seebeck coefficient of the thermoelectric couple. (b) The maximum power output for different geometry of the thermoelectric thin film material in the corrugated structure for 3 thermocouples. The line fit to the experimental data is made using equation 2. ....15
- Figure 6.** (a) Voltage output (V) and (b) power output of 3-couples of the C-TEG as function of current ( $I$ ) for a temperature difference across the couple ( $\Delta T$ ) of 7.0 K. The measurement is compared to numerical finite element simulations.....16
- Figure 7.** The theoretical maximum power density ( $p_{max}$ ) of a C-TEG module as a function of the thermoelectric couple leg length and leg angle ( $\alpha$ ) when employing the Ag-Ni couples under the heat sink limited conditions. Experimental maximum power density under the same boundary conditions for the fabricated devices is also provided (dots). .20
- Figure 8.** Geometric analysis of the maximum power density for a C-TEG based on  $Bi_2Te_3$  thermoelectric couples. (a) Power density as a function of leg length and leg stacking

angle for a constant thermoelectric element thickness ( $t_{TE}$ ) of 75 $\mu\text{m}$ . (b) Power density as a function of leg length and $t_{TE}$ for a C-TEG with a constant leg stacking angle ( $\alpha$ ) of $68^\circ$ .....	21
<b>Figure 9.</b> Approaches to wearable TEG through (a) integration and (b) woven fabric .....	29
<b>Figure 10.</b> Schematic of (a) the textile TEG patch, (b) one unit of woven TEG and (c) side view of one-unit textile TEG.....	29
<b>Figure 11.</b> (a) Thermal resistance network for analytical model and (b) $\Delta T_{TE}$ as a function of contact resistance coefficient $h_{con}$ for both Analytical model and Finite Difference method (ANSYS). .....	33
<b>Figure 12.</b> Output power density as a function of (a) TE couple leg length, (b) TE couple thickness,(c) top fiber diameter, (d) bottom fiber diameter (e) TE fiber thickness and (d) TE fiber angle with different heat sink area ratio.....	38
<b>Figure 13.</b> Power density as a function of TE leg length and bottom fiber diameter with heat sink ratio of (a) 0, (b) 0.5 and (c) 2. ....	39
<b>Figure 14.</b> Temperature profile of the top fiber for various top fiber thermal conductivity ( $\kappa_t$ ) for a top fiber length ( $L_t$ ) of (a) 25 mm and (b) 100 mm. (c) Power density as a function of $\kappa_t$ for various of $L_t$ and $x$ . ....	41
<b>Figure 15.</b> Overall area ( $A_{overall}$ ) needed as a function of target output power ( $P_a$ ) for various heat sink ratio ( $x$ ) and top fiber thermal conductivity ( $\kappa_t$ ). ....	44
<b>Figure 16.</b> The Nobel Prize in Chemistry 2000 <sup>88</sup> .....	48
<b>Figure 17.</b> Chemical structure of three conductive polymer: polyacetylene, P3HT and PEDOT .....	49
<b>Figure 18</b> Slot-die coating of the silver back electrode onto PEN. The wet print that has an opaque green color is seen behind the slot-die coating head (top right). The dried and highly reflective silver back electrode is shown on the rewinding side (top right). The menisci during coating of the eight stripe module is also shown <sup>100</sup> .....	50

**Figure 20** (a) Optical images of a large-scale aligned array of wavy, single-crystal Si ribbons (widths = 20  $\mu\text{m}$ , spacings = 20  $\mu\text{m}$ , thicknesses = 100 nm) on PDMS. (b) Angled-view scanning electron micrograph of four wavy Si ribbons from the array shown in (a)<sup>104</sup>...52

**Figure 21.** Tensile modulus vs. hole mobility for polythiophenes. (a) The tensile modulus and hole mobility of P3HT are lower than that of PBTTT. Both the stiffness and hole mobility increase when as cast PBTTT (PBTTT-AC) is annealed at 180°C (PBTTT-AN). The increase in tensile modulus and mobility of PBTTT compared with P3HT is attributed to improved order in PBTTT. Further ordering occurs in PBTTT when it is annealed, also leading to improved mobility and increased stiffness. (b) The tensile modulus and hole mobility of P3HT simultaneously increase with increasing regioregularity of the side-chains. The increase in both properties is likely due to the increased ability of regioregular P3HT to form ordered aggregates, which have improved charge transport properties, but is also stiff<sup>108,109</sup>.....53

**Figure 22.** (a) A 3D schematic of the desired morphology composed of embedded nanoscale networks of DPP-TT polymer semiconductor to achieve high stretchability, which can be used to construct a highly stretchable and wearable TFT. (b) A 3D illustration of vertical segregation of blend film. (c) AFM phase images of the top and bottom interfaces of the blend film with 70 wt% SEBS.<sup>112</sup>.....54

**Figure 23.** (a) Schematic of the segregation character of the 1:1 and 1:4 blend films. (b and c) TOF-SIMS results for vertical segregation of the (b) 1:1 and (c) 1:4 blend films on a Si substrate with its native oxide layer. The CN<sup>-</sup> ion is unique to the PCDTPT polymer<sup>117</sup>.....55

**Figure 24** (a) Sheet resistance as a function of both DMSO and Zonyl concentration in the ink. b) Plot of normalized resistance ( $R/R_0$ ) vs strain for PEDOT:PSS films spun from 0.1% and 10% Zonyl (with constant 5% DMSO) transferred onto PDMS substrates. Shaded areas represent the crack-onset strains (CoS) of the respective films. The widths of the shaded areas are two times the standard deviations for the measurements of crack-onset strain. The different marker symbols (squares, triangles, etc.) refer to different films coated from the same solution<sup>118</sup>.....57

**Figure 25** (a) DSC thermogram of the studied polymers at heating/cooling rate of 10 °C min<sup>-1</sup>, (b) DMA curves of samples at frequency of 1 Hz and heating rate of 10 °C min<sup>-1</sup>. The structures of studied polymers are shown on the right. ....58

**Figure 26.** Absorbance of the PCDTPT:P3HT blend film at 75% strain and film strained to 75% and then lowered to 10% under polarized light parallel (//) and perpendicular (⊥) to the strain direction. ....60

**Figure 27.** UV-vis setup in O'Connor research laboratory, NC State University .....61

**Figure 28.** Schematic of how an AFM works<sup>129</sup>. ....62

**Figure 29.** MFP-3D model AFM from Asylum Research. ....62

**Figure 30** Schematic representations of field-effect transistor architectures, (a) top-gate bottom-contact, (b) top-gate top-contact, (c) bottom-gate bottom-contact, and (d) bottom-gate top-contact. The arrow shows the charge conduction interface<sup>130</sup>. ....64

**Figure 31.** Microscope image of source and drain electrodes made of 40 nm gold/5 nm titanium for one transistor testbed. ....64

**Figure 33.** (a) Photos of an unstrained film, 75% strained film and strain-released film at 10% strain while on PDMS. (b) Illustration of the change in film morphology during the cyclic strain process from a top view and side view. At large tensile strain, the illustration includes alignment of both polymers and partial tearing features. When the strain is reduced the polymer alignment reduces and tearing features narrow. The side view includes an illustration of the vertical segregation of the polymers found in the blend film. (c) An illustration of transfer printing the polymer semiconductor film from the elastomer stamp to an OTFT test bed. ....71

**Figure 34.** (a) Absorbance of the PCDTPT:P3HT blend film at 75% strain and film strained to 75% and then lowered to 10% under polarized light parallel (||) and perpendicular (⊥) to the strain direction. (b) The normalized absorbance of the blend film at 75% strain and at 10% strain, comparing the first strain cycle (1x) to 100 cycles (100x). The measured absorbance at a specific strain state and polarized light orientation are normalized and offset for clarity. The absorbance at a specified strain state and light polarization during the first strain cycle and after 100 cycles are plotted together to

compare absorbance features. (c) The dichroic ratio of the blend film under tensile strain (+) and reduction of the applied strain (-) during the first strain cycle. The dichroic ratio is taken at 550 nm and at 900 nm to capture the P3HT and PCDTPT, respectively. (d) The dichroic ratio of the blend film at 75% strain and 10% strain with increasing number of strain cycles. ....75

**Figure 35.** Two-dimensional grazing incidence X-ray diffraction images of (a) an unstrained film, and strained films during the (b-e) first strain cycle and after (f-i) 100 strain cycles held at 75% strain and 10% strain as specified. The X-ray beam is incident parallel ( $\parallel$ ) or perpendicular ( $\perp$ ) to the strain direction as labeled. ....76

**Figure 36.** Two-dimensional grazing incidence X-ray diffraction images of films strained to 75% and 10% after 10 and 50 strain cycles. The X-ray beam is incident parallel (para) or perpendicular (perp) to the strain direction as labeled. ....76

**Figure 37.** In-plane line scans of the 2D GIXD images with X-ray parallel to the strain direction, taken for films at the (a) 75% strain limit and (b) 10% strain limit. The reported data is for the films in its 1<sup>st</sup> strain cycle (1x) and 100<sup>th</sup> strain cycle (100x). ....77

**Figure 38.** AFM height images of films strain by 75% and then lowered to 10% strain after (a,b) 1, (c,d) 10, (e,f) 50 and (g,h) 100 strain cycles. (i) An AFM image of an unstrained film. The area of all images are  $5\ \mu\text{m} \times 5\ \mu\text{m}$ . The black arrow shown below the AFM images provides the direction the film was strained. Line scans for films at (j) 75% strain and (k) 10% strain after 100 strain cycles. The line scan for the 75% strained film is given at the edge of the film to show that the roughness is not through the film thickness. ....81

**Figure 39.** Optical microscope image of (a) a PCDTPT:P3HT blend film at 10% strain after 50 strain cycles, and (b) a P3HT film at 10% strain after 10 strain cycles between 75% strain and 10% strain. Arrows in figure indicate the applied strain direction. Both images are taken while on the PDMS substrate. Clear differences in delamination (dark lines) are observed between films. ....82

**Figure 40.** SEM images of the (a) PCDTPT:P3HT blend and (b) neat P3HT film after cyclically strained between 75% strain and 10% 10 times and held at the lower strain

limit. To image the films the PDMS was adhered to a glass substrate. During this process there was additional strain release and the strain state is closer to approximately 6% strain. The images are taken with the films at a 45-degree tilt. ....82

**Figure 41.** (a) Saturated field effect mobility with channel length for an unstrained as cast film, and for charge transport parallel to the strain direction for 75% strained films without thermal annealing (AC) and for a film that is thermally annealed after spin casting at 180C for 10 minutes and then straining the film by 75% and printing onto the rigid testbed. (b) Characteristic transfer curves for 5  $\mu\text{m}$  channel length devices for each of these films. ....84

**Figure 42.** Saturated field effect mobility with strain, parallel (para) and perpendicular (perp) to the strain direction for a single tensile strain, for 5  $\mu\text{m}$  channel length devices .....85

**Figure 43.** Saturated field effect mobility for (a) charge transport parallel to the strain direction, and (b) charge transport perpendicular to the strain direction for films at 75% strain and films released to 10% strain for a specified number of strain cycles. Charge mobility is also reported for an unstrained film. The channel length for the transistors is 5  $\mu\text{m}$ . ....85

**Figure 44.** Subthreshold swing (a,b), on-off ratio (c,d), and threshold voltage ( $V_{\text{TH}}$ ) of the transistor transfer characteristics with number of strain cycles. This includes charge transport parallel to the strain direction (a,c,d) and perpendicular to the strain direction (b,d,f). Values are reported for films held at the 75% strain and 10% strain limits. ....86

**Figure 45.** Transfer curve for unstrained film and film strain by 75% after 1 and 100 strain cycles for charge transport parallel to the strain direction (without any thermal annealing step). ....86

**Figure 46.** Saturated field effect mobility for (a) charge transport parallel to the strain direction, and (b) charge transport perpendicular to the strain direction for films at 75% strain and films released to 10% strain for a specified number of strain cycles. Charge mobility is also reported for an unstrained film. The channel length for the transistors is 100  $\mu\text{m}$ . ....87

**Figure 47.** Illustration of the change in the films surface morphology when on the (a) normal PDMS substrate and (b) UV/ozone treated PDMS substrate during the cyclic strain process from the side view. (c) UV/Ozone treatment effect on PDMS. ....**96**

**Figure 48.** Contact angle and adhesion energy for PDMS under different UV/ozone treatment time. ....**100**

**Figure 49.** AFM surface morphology of a buckled PDMS at rest obtained with 15% pre-strain and UV/ozone treatment for 20 min. ....**100**

**Figure 50.** Characterization of UV/Ozone treated PDMS surface layer thickness using ellipsometry. (a) Psi and Delta fitting of measured data with existing model. (b) Uniqueness analysis of Mean Squared Error (MSE). ....**101**

**Figure 51.** AFM scanned surface morphology for 30 nm and 150 nm DPP-4T film before and after reaching the YOE and YOW. ....**106**

**Figure 52.** Yield point on elastomer (YOE) and yield point on water (YOW) for films onto PDMS with different UV/ozone treatment time. ....**106**

**Figure 53.** RMS roughness of films (a) being strained and (b) strain released during the cyclic strain process. AFM images films being strain released for two different strain ranges for 1 and 100 cycles onto PDMS with different treatment conditions are shown here. For strain range from 20% to 60%, AFM images are presented for films with (c) 1 cycle and (d) 100 cycles with normal PDMS, (e) 1 cycle and (f) 100 cycles with UV/ozone for 10 min, and (g) 1 cycle and (h) 100 cycles with UV/ozone for 20 min. For strain range from 5% to 45%, AFM images are presented for films with (i) 1 cycle and (j) 100 cycles with normal PDMS, (k) 1 cycle and (l) 100 cycles with UV/ozone for 10 min, and (m) 1 cycle and (n) 100 cycles with UV/ozone for 20 min. ....**112**

**Figure 54.** AFM images for films being strained and strain released for different cycles and different strain ranges onto PDMS with different UV/ozone treatment conditions. ....**113**

**Figure 55.** (a) Absorbance of DPP-4T film onto 20 min UV/ozone PDMS at 60% strain and film strained to 60% and then lowered to 20% under polarized light parallel ( $\parallel$ ) and perpendicular ( $\perp$ ) to the strain direction. (b) The normalized absorbance of the film onto 20 min UV/ozone PDMS substrate at 60% strain and at 20% strain for strain range of

20% - 60%, and of film at 45% strain and at 5% strain for strain range of 5% - 45%, comparing the first strain cycle (1x) to 100 cycles (100x). The measured absorbance at a specific strain state and polarized light orientation are normalized and offset for clarity. The absorbance at a specified strain state and light polarization during the first strain cycle and after 100 cycles are plotted together to compare absorbance features. (c) The dichroic ratio of the film onto 20 min UV/ozone PDMS substrate under tensile strain (+) and reduction of the applied strain (-) during the first strain cycle for strain range of 20% to 60% and 5% to 45%. The dichroic ratio is taken at 783 nm. (d) The dichroic ratio of the film onto 20 min UV/ozone PDMS substrate at 60% strain and 20% strain for 20% - 60% strain range and 45% strain and 5% strain for 5% - 45% strain range with increasing number of strain cycles. ....114

**Figure 56.** Normalized absorbance and dichroic ratio for films being strained and strain released for different cycles and different strain ranges onto PDMS with different UV/ozone treatment conditions. ....115

**Figure 57.** Schematic illustration of lamination method used to evaluate semiconducting polymers for stretchable electronics<sup>158</sup>. ....119

## NOMENCLATURE

### *Symbols*

$A_{con}$	contact area between fiber and skin
$A_{ex}$	surface area of the added heat sink sheet
$A_m$	project area of the thermoelectric module
$A_{overall}$	overall area needed for power wearable electronics
$A_p$	projected area of the woven TEG
$A_s$	summed cross section area of polyimide substrate
$A_{TE}$	summed cross section area of the thermoelectric elements and substrate
$C$	packing density
$C_{ox}$	capacitance of the dielectric layer per unit area
$d$	width of tape
$d_1$	top fiber diameter
$d_2$	bottom fiber diameter
$D_{wa}$	length of one unit TEG in the wasp direction
$D_{we}$	length of one unit TEG in the weft direction
$E_u$	elastic modulus of thin film
$E_s$	elastic modulus of PDMS substrate
$F$	average peeling force
$G$	overall thermal conductance of the thermoelectric elements and substrate
$h$	heat transfer coefficient
$h'$	modified heat transfer coefficient
$h_c$	heat convection coefficient
$h_{con}$	contact thermal coefficient
$I$	electric current
$J$	adhesion energy
$k$	cantilever stiffness
$L$	leg length
$L_c$	channel length
$L_{TE}$	TE element leg length
$N$	interactive force
$n$	number of the TE couples
$P$	total output power
$p$	power density
$p_{max}$	maximum power density
$P_{max}$	maximum total output power
$R_{con}$	contact thermal resistance
$R_i$	thermoelectric internal electrical resistance
$R_o$	load electrical resistance
$R_{spr}$	heat spreading thermal resistance
$S$	Seebeck coefficient
$S_{TE}$	Seebeck coefficient of one TE couple
$T$	absolute temperature
$T_g$	glass transition temperature

$t_s$	thickness of the TE fiber
$t_{TE}$	thickness of the TE elements
$V_g$	gate voltage
$V_{th}$	threshold voltage
$W$	channel width
$w_{TE}$	width of TE elements
$x$	ratio of area of added heat sink sheet to the projection area of TEG
$ZT$	thermoelectric figure of merit
$z$	deflection of cantilever tip

### ***Greek symbols***

$\alpha$	stacking angle
$\Delta$	change in a property
$\theta$	TE fiber angle
$\kappa$	thermal conductivity
$\lambda$	buckling wavelength
$\mu$	charge carrier mobility
$\nu$	Poisson ratio
$\rho$	electrical resistivity
$\sigma$	electrical conductivity

### ***Subscripts***

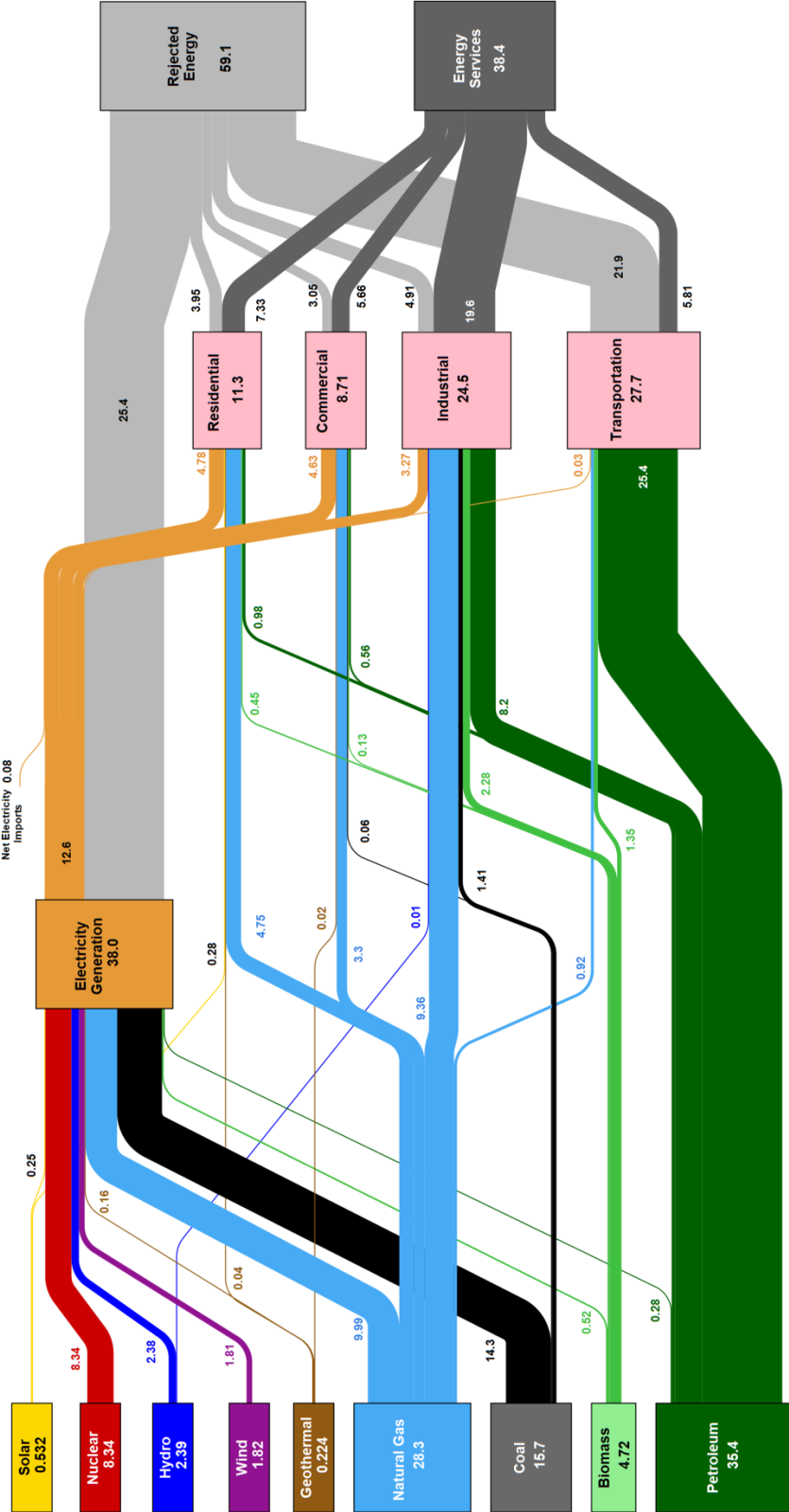
$a$	ambient property
$b$	bottom fiber property
$C$	cold side
$f$	supporting fiber property
$g$	gate
$H$	hot side
$max$	maximum
$opt$	optimal
$s$	TE fiber
$skin$	skin property
$TE$	thermoelectric element
$t$	top fiber property
$th$	threshold
$u$	thin film

# 1 Unconventional thermoelectric generators (TEGs)

## 1.1 Introduction

The global energy demand to support modern society has been increasing rapidly along with the economic development. Since 1990, the world energy consumption increased from less than 400 quadrillion BTU to 600 quadrillion BTU, and will continue to increase to 800 quadrillion BTU in 2040 <sup>1</sup>. In order to meet this high demand on energy and perform sustainable development, on one hand, new types of renewable (solar, wind, biomass, et al) energy are exploited to replace the finite resources like fuel and coal. On the other hand, increasing the energy usage efficiency to reduce the amount of useless waste heat generated, or reusing this waste heat is a promising approach to solve the global resources scarcity problem. In fact, almost 60% of primary energy sources is converted to waste heat when being used (**Figure 1** <sup>2</sup>) in U.S in 2015. Most of this waste heat comes from the incomplete combustion and inefficient heat transfer <sup>3</sup>. The utilization of this low-grade waste heat commonly includes district building heating, chemical synthesis processes and water heating<sup>3,4</sup>. Thermoelectric generators (TEGs) provide the opportunity to convert this waste thermal energy directly to electrical power, and fit the need for thermal energy harnessing over a broad temperature range. It is also in a small size without moving part. However, to date, there has been only limited commercial adoption due to the high costs and relative low efficiency compared to other technologies. Therefore, in order to make TEG competitive, more research efforts and further improvement in this area are required.

# Estimated U.S. Energy Consumption in 2015: 97.5 Quads



Sources: LBNL March 2016. Data is based on DOE/EIA NEMS (2015). If this information is used, credit must be given to the Lawrence Livermore National Laboratory and the Department of Energy under whose auspices the work was performed. Distributed electricity represents only retail electricity sales and does not include self-generation. EIA reports consumption of renewable resources (i.e., hydro, wind, geothermal and solar) for electricity in BTU-equivalent values by assuming a typical fossil fuel plant heat rate. The efficiency of electricity production is calculated as the total retail electricity delivered divided by the primary energy input into electricity generation. End use efficiency is estimated as 65% for the residential sector, 65% for the commercial sector, 80% for the industrial sector, and 21% for the transportation sector. Totals may not equal sum of components due to independent rounding. LBNL-ML-410527

Figure 1 Estimated U.S. Energy Consumption in 2015<sup>2</sup>

### 1.1.1 Thermoelectric technology and device performance

The thermoelectric effect describes the direct conversion of thermal energy to electrical power. It mainly involves three separately identified effects: the Seebeck effect, Peltier effect and Thomson effect. The Seebeck effect is the electrical potential that develops in the presence of a temperature gradient. It described a phenomenon that if a connection between two different metal wires was heated, a voltage difference would be generated between the other ends of these two metal wires due to the diffusion of charge carrier from hot side to the cool side driven by the temperature gradient <sup>5</sup>. The Peltier effect, conversely, is the conversion from electricity to temperature difference. When an electric current pass through a junction of two different metal wires, it the Peltier effect results in heating or cooling at the wire junction. This effect is a result of electron energy states changing when current is passed the junction. The Thomson effect described the reversible heating or cooling in a junction where both temperature difference and electric current exist, and involves both Seebeck effect and Peltier effect.

**Figure 2** describes the concepts of Seebeck effect and Peltier effect and how they are applied in a TE device. The traditional TE devices include thermoelectric generators (TEGs) and thermoelectric coolers (TECs), and both have the similar configuration. They are usually made of p-type and n-type rigid, bulk TE materials, which are electrically connected in series by metal interconnection, and this is the common design for commercial products.

The performance of a TE device is usually indicated by the maximum efficiency ( $\eta_{max}$ ), which is given as <sup>5</sup>:

$$\eta_{max} = \frac{T_H - T_C}{T_H} \frac{\sqrt{1 + ZT} - 1}{\sqrt{1 + ZT} + \frac{T_C}{T_H}} \quad (1)$$

in which  $T_H$  is the temperature at the hot side of TE couple,  $T_C$  is the temperature at the cool side of TE couple, and  $ZT$  is TE element's dimensionless figure of merit. The  $ZT$  value is determined by TE material property and decides how efficiently a TE material can produce thermoelectric power at a certain environment temperature, which is shown as <sup>5</sup>

$$ZT = S^2\sigma T/\kappa \quad (2)$$

in which  $S$  is Seebeck coefficient,  $\sigma$  is electrical conductivity,  $\kappa$  is thermal conductivity,  $T$  is absolute temperature.

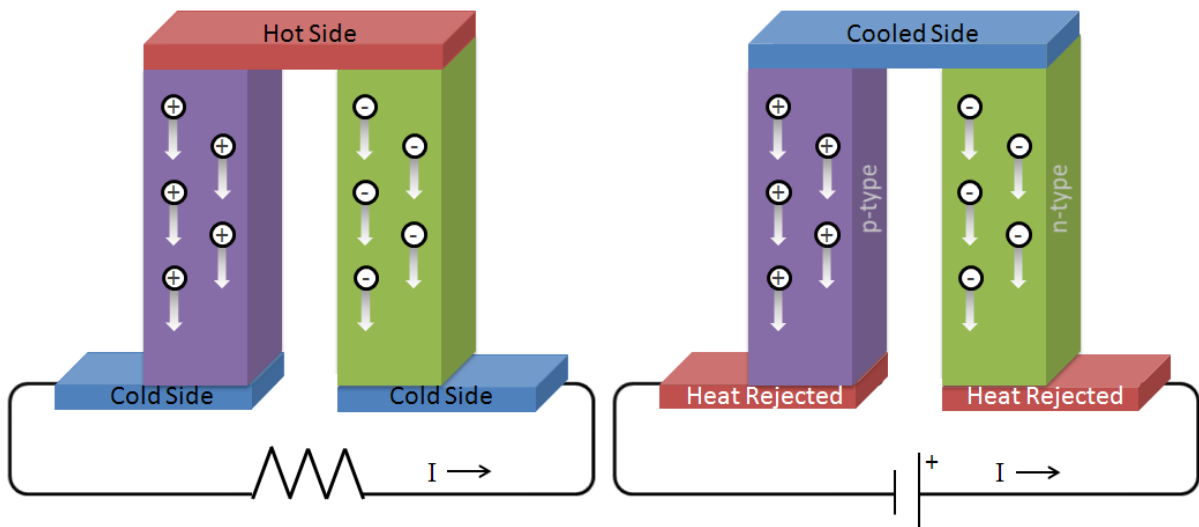


**Figure 2** Schematic of Seebeck effect and Peltier effect<sup>6</sup>

There was little improvement in TE material until the end of twentieth century (**Figure 3(a)**<sup>7</sup>). However, significant efforts have focused on improving the  $ZT$  value recently and the maximum value has been improved above 2 for both n-type and p-type TE material (**Figure 3(b)** (c)<sup>8</sup>) due to the employment of new chemical systems such as skutterudites, pentatellurides, ternary chalcogenides and clathrates<sup>9</sup>.

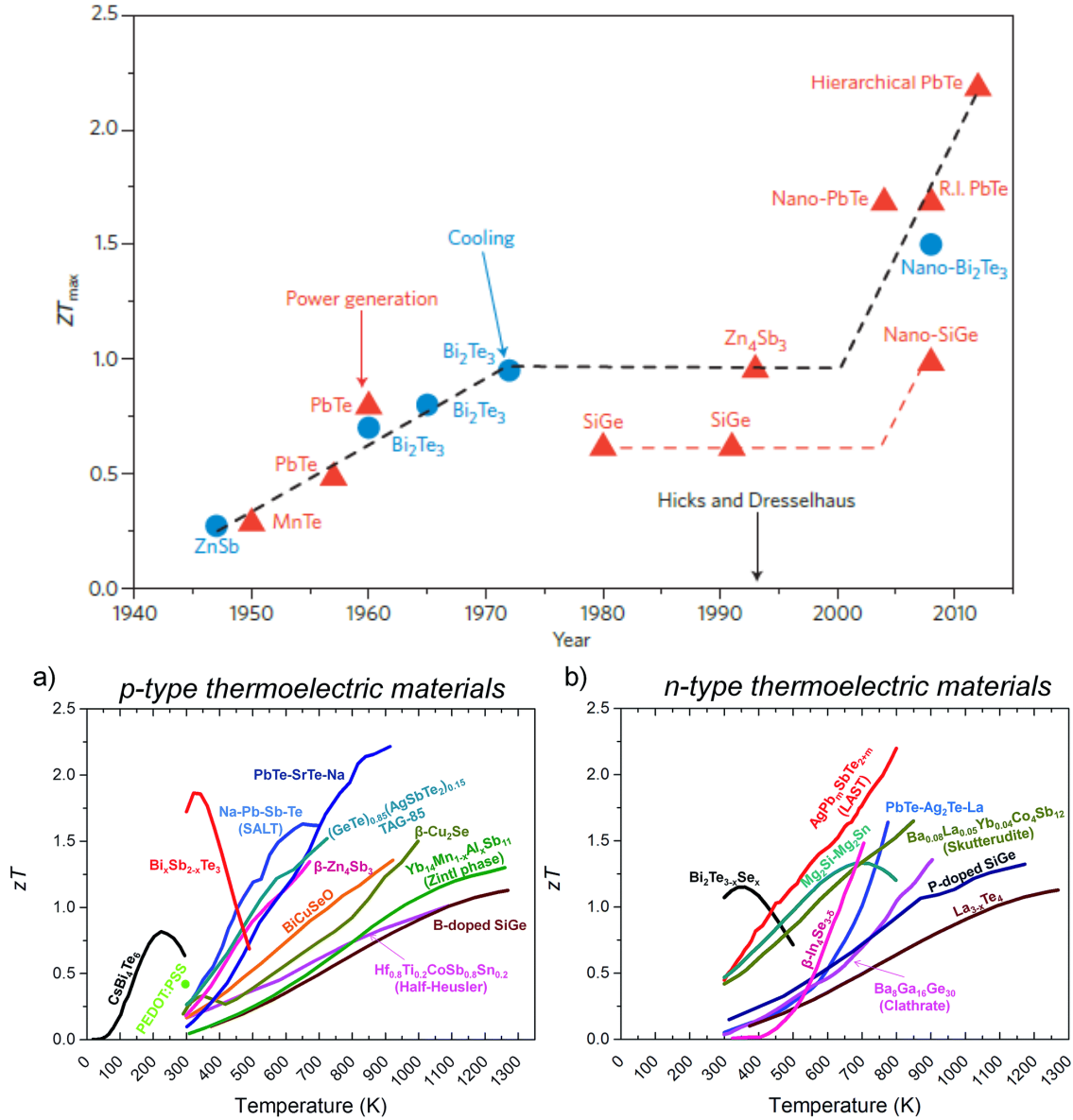


**Figure 3** (a) Evolution of the maximum  $ZT$  over time <sup>7</sup>. Summary of some of best  $ZT$  for (b) p-type and (c) n-type bulk thermoelectric materials as a function of temperature <sup>8</sup>

### 1.1.2 Novel thermoelectric device design

Despite the traditional design of bulk TE devices, novel TE device designs have come up in order to improve the performance, reduce the fabrication cost, or apply for special applications like flexibility. In addition to improving the TE material  $ZT$  value, a good TE device structure design can also lead to significant improvement of the device performance.

One important principle is to let the TE materials function within their optimum temperature range. From **Figure 3** (a) and (b), for most of p-type and n-type TE materials, the ZT values reach a maximum point at a certain temperature range. For example, B<sub>i</sub> group material functions best around room temperature, while P<sub>b</sub> group more intends to work at a higher temperature around 900 K. When being operated at a wide range of temperature difference, it's more ideal to stack multiple TE material in series, or called segmented TE device <sup>10-12</sup>, ensuring they all functions near their own optimum temperature range to boost the overall device efficiency. By using this method, a high conversion efficiency of 20% has been accomplished <sup>12</sup>.

While improving efficiency is critical for competitiveness, a low-cost fabrication process is also important for commercialization. Huang et al. came up with a planar design of micro-TEC using bridge geometry, which is believed to be compatible with integrated circuit (IC) batch processes and will eventually reduce the fabrication cost <sup>13</sup>. Another useful method to reduce cost would be employing thin film TE materials and roll-to-roll fabrication process <sup>14-16</sup>. The thin film TE materials usually possess a lower thermal conductivity than the bulk ones due to the increasing phonon scattering near the surface and thus increase the device performance <sup>17</sup>. The thin film TE devices are also compatible with organic TE material. Compared with inorganic material, organic TE material possess the advantages of easy fabrication, low cost, light weight and flexibility yet suffer from low efficiency. The best ZT value of OTE material so far is 0.42 reported by Kim et al. <sup>18</sup>

## 1.2 Heat shrink formation of a corrugated thin film thermoelectric generator

### 1.2.1 Introduction and motivation

(From T. Sun, J. L. Peavey, M. D. Shelby, S. Ferguson, and B. T. O'Connor, "Heat shrink formation of a corrugated thin film thermoelectric generator", *Energy Conversion and Management*, 103, 2015.)

The direct conversion of thermal energy to electrical power without moving parts makes thermoelectric generators (TEG) a highly attractive energy conversion technology. These devices also have the advantage of having a small volume, and the ability to convert energy over a broad temperature range. However, to date there has been limited commercial adoption of TEGs due to high module costs and relative poor efficiency compared to other technologies. Recently, significant efforts have focused on developing thermoelectric (TE) materials with increased efficiency through improving the TE element's dimensionless figure of merit,  $ZT = S^2\sigma T\kappa^{-1}$ , where  $S$ ,  $\sigma$ ,  $T$  and  $\kappa$  are the Seebeck coefficient, electrical conductivity, absolute temperature, and thermal conductivity, respectively<sup>19</sup>. The  $ZT$  value provides an upper limit on TE power conversion efficiency and is thus a key optimization parameter<sup>20</sup>. Currently, there have been numerous demonstrations of thermoelectric materials with  $ZT$  values greater than 2<sup>16,21</sup>. However, TEGs based on these materials will struggle to become cost effective<sup>22</sup>. Alternatively, low-cost thermoelectric materials based on organic and organic–inorganic hybrid systems are being developed that have recently shown promising cost-performance metrics<sup>22,23</sup>. Conjugated polymers have been developed with  $ZT$  as high as 0.4<sup>18</sup>, and hybrid solution processed materials have been shown to have  $ZT$  values as high as 0.1<sup>24</sup>.

While improving  $ZT$  is critical for cost competitiveness, other aspects of TEG design must also be considered to ensure low cost and high performance systems<sup>25,26</sup>. In particular, it is highly advantageous to develop TEG modules that are compatible with low-cost processing methods and to develop modules that do not have elaborate heat sink demands<sup>27</sup>. Low-cost TE processing has focused on thin-film materials that are compatible with roll-to-roll processing<sup>28-30</sup>. For these thin-film elements, heat transfer across the plane of the film (cross-plane TEs) is the most common module architecture<sup>31,32</sup>. However, maintaining a large temperature difference across the thin film junctions (and thus increasing power output) becomes a challenge<sup>27</sup>. Thin film TEGs can also be designed such that heat transfer occurs in the plane of the film (in-plane TEs)<sup>33-35</sup>. However, this design is not compatible with large area heat sources, and thus not typically applied for power generation<sup>36</sup>. An alternative thin-film thermoelectric design is to place the thin film thermoelectric elements in a corrugated arrangement between thermal interface planes, as illustrated in **Figure 4** and labeled here as a corrugated TE generator (C-TEG). In this design, heat transfer is in the plane of the thin-film thermoelectric elements, effectively increasing the TE element leg-length and improving the ability to maintain a finite temperature difference across the thermoelectric junctions. While heat transfer is in the plane of the thin film, the module remains a cross-plane TE design making it compatible with large area applications.

There have been several previous demonstrations of similar corrugated-type TEGs<sup>34,37-39</sup>. In these demonstrations, there have been two primary methods of fabrication. In the first approach, the TE elements are deposited onto a flat plastic substrate, the substrate is then adhered to a secondary corrugated surface<sup>37</sup>. The secondary surface holds the thin film in the corrugated shape and acts to separate the cold and hot side junctions. In this approach, the

secondary element is a solid material that will result in a significant reduction in temperature difference across the thermocouples lowering power generation and efficiency. The second approach consists of using a thin film plastic substrate that is held in a sinusoidal mold. The thermoelectric elements are vacuum deposited onto the substrate and then the plastic substrate is removed from the mold and bonded to planar plastic plates to maintain the corrugated module architecture. This is an effective approach to form the corrugated module, however depositing onto a non-planar substrate is a challenge and requires vapor deposition methods that are unable to take advantage of low-cost solution processing methods of organic and hybrid materials<sup>38</sup>.

Here, we further demonstrate a method of fabricating a C-TEG by using an innovative plastic heat shrink approach<sup>40</sup>. This method is compatible with processing thermoelectric elements onto flat surfaces that are then formed into the C-TEG geometry. This approach has the advantage of simple corrugated element formation that results in freestanding thermoelectric legs that will minimize parasitic thermal losses. The experimental performance of a thermally formed C-TEG with metallic thermoelectric elements is characterized in detail and compared to finite element and analytical models. To consider the opportunities of this device architecture, it is investigated theoretically with high performance thermoelectric materials and the architecture is optimized using thermal impedance analysis.

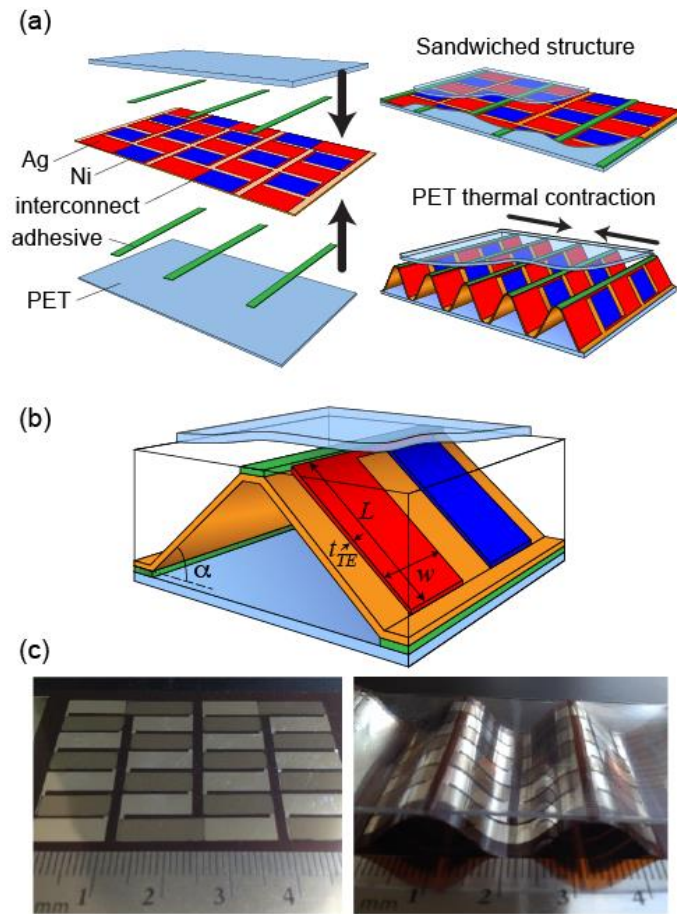


**Figure 4.** (a) Schematic illustration of the fabrication process for the corrugated TEG device, including the stack of heat-shrink PET, the adhesives, and thermoelectric couples on a polyimide substrate. The layers are all combined forming a sandwiched structure that is then thermally formed into the corrugated TEG. (b) Simplified geometric model of corrugated TEG device, with thermoelectric leg dimensions including thermoelectric thickness ( $t_{TE}$ ), length ( $L$ ), width ( $w_{TE}$ ), and stacking angle ( $\alpha$ ). (c) Photos of the corrugated TEG device before and after being thermally formed.

### 1.2.2 Corrugated thermoelectric module fabrication

A schematic of the fabrication process, and final structure is illustrated in **Figure 4(a)**. For proof-of-concept purposes, the thermoelectric elements consisted of Ag and Ni thin films deposited by vacuum thermal evaporation onto a 130- $\mu\text{m}$  thick polyimide substrate, and patterned using a shadow mask. The polyimide film was the core layer of the TEG module and the support for the thin-film thermoelectric legs. The thermoelectric elements were 140-nm thick, 4-mm wide and variable in length. The thermoelectric legs were electrically connected laterally in a row and then between rows at the last TE elements with Ag thin films, as illustrated in **Figure 4(a)** and pictured in **Figure 4(c)**. There was approximately 0.5 mm overlap of the metallic elements to form the electrical junctions. The non-shrink polyimide core was then attached to heat-shrink polyester (PET) films on each side of the polyimide with polymer adhesive placed between the rows of the thermocouples in alternating fashion. The outer layers were uniaxial stretch-oriented having a glass transition temperature ( $T_g$ ) of approximately 345 K. The outer layers were extruded to create the un-oriented base material and then uniaxially stretched at a temperature of approximately 355 K<sup>40</sup>. The three-layer planar composite structure was then placed in a vacuum oven at 383 K causing the PET sheets to shrink and forcing the polyimide interlayer to form and maintain a sinusoidal shape. In this demonstration, 630- $\mu\text{m}$  thick PET films were stretched by 33%, resulting in films with a shrink of approximately 25% after heating. An example of the fabricated hybrid TEG is pictured in **Figure 4(c)** and is composed of three and a half Ag-Ni couples per row with legs that are 12 mm long and 4 mm wide. Note that Ag and Ni were chosen for their good thermoelectric properties among metals. These materials are also

ductile and adhere well to the polyimide allowing for bending during TEG formation without mechanical failure.

### 1.2.3 Results and Discussion

#### *Performance analysis*

The performance of the TE couples was characterized prior to the attachment of the PET outer layers, and then again after the completed corrugated TE fabrication process as described above. The TE couples tested prior to device fabrication were in a planar configuration. The temperature difference was achieved using commercial thermoelectric modules, one on each side of the couples with one heating and the other cooling. The planar TE device was placed across the commercial thermoelectric modules. The temperature at the junctions of the test structure was measured with a surface thermocouple (Model 88014, Omega Engineering) placed in close proximity to the metal junctions. For the C-TEG testing, the commercial thermoelectric modules were placed on each side of the test module. Again, one module was set to cool and the other to heat to generate a temperature difference across the module. In this case a thermocouple (5-SRTC, Omega Engineering) was adhered at the metal junctions using thermal paste. The current–voltage characteristics of the test devices were measured using a semiconductor parameter analyzer (HP 4156b). In **Figure 5(a)** the open circuit voltage is given as a function of temperature difference between the thermocouple junctions ( $\Delta T$ ) for a row of 3 couples and a row of 10 couples with 8-mm long legs. From the slope of the curve the Seebeck coefficient of one couple ( $S_{TE}$ ) is found to be  $19.0 \mu\text{V K}^{-1}$  for the 3 TE couples in the flat sheet configuration, which matches well to previous experimental result of  $19.2 \mu\text{V K}^{-1}$ <sup>41</sup>. However,  $S_{TE}$  drops down to  $14.2 \mu\text{V K}^{-1}$  when formed into the C-TEG design. Similarly, the electrical resistivity was found to be

368 nΩ m while flat and 875 nΩ m when bent. This resistivity is higher than typically observed for these metals in bulk form (20 nΩ m and 190 nΩ m for Ag and Ni, respectively)<sup>42-44</sup>. The large resistivity of the films in the flat configuration is attributed to the vacuum deposition process and thin film nature, which has previously been shown to increase the resistivity of metals compared to their bulk counterpart<sup>45,46</sup>. The change in properties when forming the C-TEG module is likely due to an increase in dislocation density and other defects associated with the bending process. The smallest radius of curvature observed for the thermoelectric couples with leg length of 8 mm was found to be approximately 3.8 mm. Previous research considering the change in conductivity of thin metal films with bending radius showed similar changes in electrical resistivity<sup>47</sup>. Critically, the metallic interconnection of the thermoelectric legs for different rows, pictured in **Figure 4(c)**, will see the smallest radius of curvature and the metal film will be in contact with the polymer adhesive. To determine if this has a large impact on performance, the Seebeck coefficient was measured across 10 thermocouples over multiple rows, which includes the interconnecting Ag film between rows. The average  $S_{TE}$  was found to be 14.0 μV K<sup>-1</sup> per couple, showing negligible performance loss associated with this interconnection.

The output voltage and output power for 3 TE couples in one row of the C-TEG was investigated experimentally and with finite element numerical simulation using ANSYS<sup>48</sup>, for a  $\Delta T$  of 7.0 K. The finite element model consisted of 598,225 nodes and 295,719 elements using an auto-generated mesh. The model assumes planar legs as illustrated in **Figure 4(b)**. The difference in the finite element model output using sinusoidal legs and the straight leg approximation has previously been shown to be negligible<sup>49</sup>. Experimentally, the maximum output power was found to be approximately 0.67 nW at a current of 4.1 μA, as

shown in **Figure 6**. The result from the finite element simulation matches well with the experimental measurement, with a maximum output power of 0.65 nW. Generally, the total output power ( $P$ ) of TEGs can be given by<sup>27</sup>,

$$P = \frac{(nS_{TE}\Delta T)^2 R_o}{(R_i + R_o)^2}, \quad (3)$$

where  $n$  is the number of the TE couples,  $R_i$  is the TEG internal electrical resistance and  $R_o$  is the load electrical resistance. The maximum output power occurs when the load electrical resistance is equal to the internal electrical resistance of TEG resulting in,

$$P_{max} = \frac{(nS_{TE}\Delta T)^2}{4R_i}. \quad (4)$$

The geometry of the TE couples directly impacts the maximum output power due to  $R_i$  given by,

$$R_i = \frac{\rho L}{w_{TE}t_{TE}}, \quad (5)$$

where  $\rho$  is the combined electrical resistivity,  $L$  is the leg length,  $w_{TE}$  is width of TE elements and  $t_{TE}$  is thickness of the elements. The experimental maximum output power with variation in temperature difference for various  $L/t_{TE}$  ratios is given in **Figure 5(b)** and is compared to the predicted power from Eqn. (4). It is found that  $P_{max}$  increases with  $\Delta T$  following a parabolic relationship as expected. It is clear that the thicker film and shorter leg length result in high power output following the relationship that power density is proportional to  $(w_{TE}t_{TE})/L$ , as given by Eqn. (4)<sup>50</sup>.

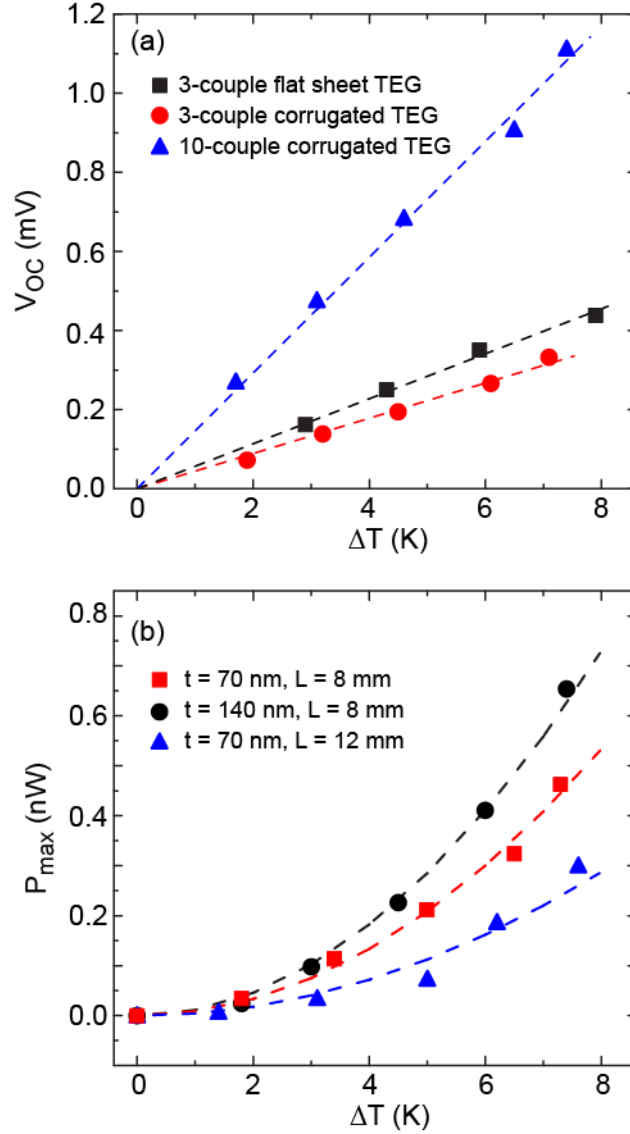


**Figure 5.** (a) Open circuit voltage ( $V_{oc}$ ) as a function of the temperature difference across the couples ( $\Delta T$ ) for various thermocouple configurations, 3 TE couples in a flat sheet, 3 TE couples in the corrugated structure, and 10 TE couples in the corrugated structure. The linear fits to the data are used to determine the average Seebeck coefficient of the thermoelectric couple. (b) The maximum power output for different geometry of the thermoelectric thin film material in the corrugated structure for 3 thermocouples. The line fit to the experimental data is made using equation 2.

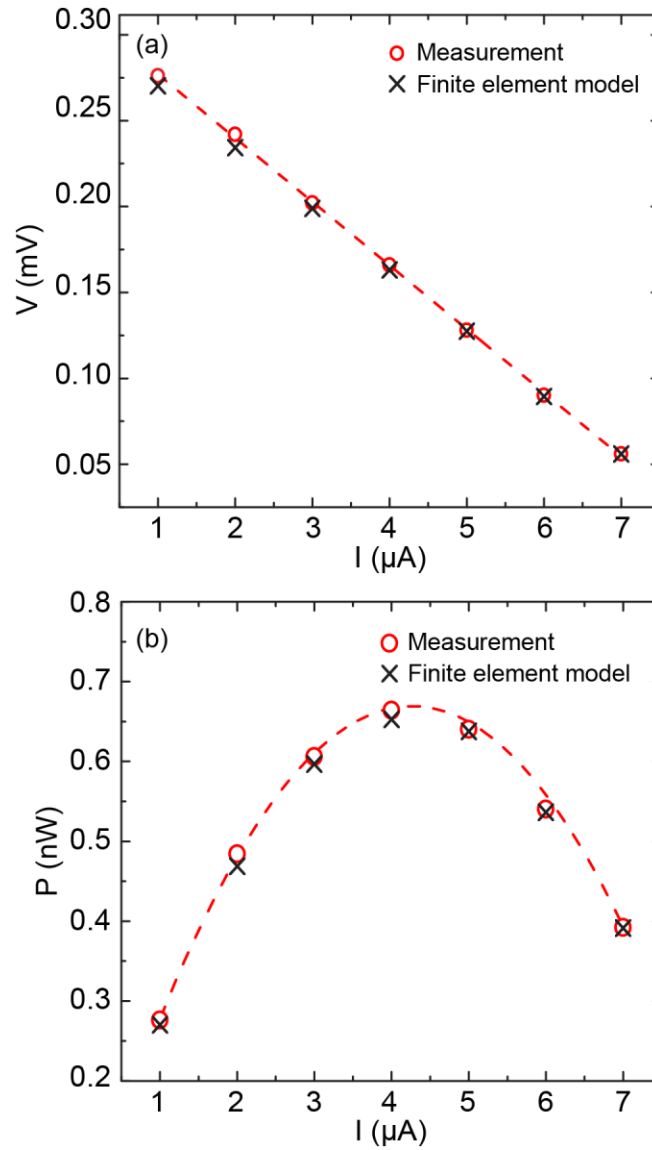


**Figure 6.** (a) Voltage output ( $V$ ) and (b) power output of 3-couples of the C-TEG as function of current ( $I$ ) for a temperature difference across the couple ( $\Delta T$ ) of 7.0 K. The measurement is compared to numerical finite element simulations.

### ***Theoretical Performance Optimization***

The geometry of the experimentally demonstrated modules was selected based on availability of pre-stretched PET, stability of the thermally formed corrugated film, and ability to easily probe the temperature profile across the thermocouples. However, the resulting modules may not be the optimal geometry for power generation. Similarly, high performance materials may be employed as long as bending during fabrication does not significantly impact their properties. With this in mind, a dimensional and material analysis is theoretically conducted on the C-TEG design to consider the performance potential of this architecture. With the goal of minimizing the system cost, it is expected that the module will operate in the heat sink limited regime<sup>25,27</sup>. The TEG is heat sink limited when the output power of the system is limited by the ability to transfer heat to or away from the thermoelectric couples. This would be expected for a TEG system without elaborate heat sink designs. Here, the TEG performance is optimized under the conditions of a constant hot side temperature of the thermoelectric couple ( $T_H$ ), and heat rejection being limited by natural convection<sup>25,27</sup>. Optimal performance of this system is found under thermal impedance matching conditions. Details of this approach have been previously described<sup>25,27</sup>. Here, we provide a brief review of the analysis method. In thermoelectric operation, the convective heat transfer from the cold side of the module is equivalent to the summed conduction through the module, Peltier heat transfer, and joule heating, given by,

$$hA_m(T_C - T_a) = G(T_H - T_C) + S_{TE}T_C I + \frac{1}{2}I^2 R_i, \quad (6)$$

where  $h$  is the heat transfer coefficient,  $A_m$  is the projected area of the TEG module,  $T_C$  is the cold side temperature of the TE couple,  $T_a$  is the environment temperature,  $I$  is electric current, and  $G$  is overall thermal conductance of the TE elements and substrate given by,

$$G = \frac{\kappa_{TE}A_{TE}}{L} + \frac{\kappa_s A_s}{L}, \quad (7)$$

where  $\kappa_{TE}$  is the thermal conductivity of the TE element,  $A_{TE}$  is the summed cross section area of the TE couples,  $\kappa_s$  is the thermal conductivity of the polyimide substrate and  $A_s$  is the summed cross section area of the polyimide substrate. To simplify the calculation, Peltier heat transfer and joule heating, which are relatively small compared with heat conduction are neglected<sup>27</sup> resulting in,

$$hA_m(T_C - T_a) \approx G(T_H - T_C). \quad (8)$$

The design of the C-TEG module will typically result in a low areal packing density of thermoelectric elements as compared to a conventional bulk TEG. This requires that the thermal resistance caused by heat spreading also be included in the optimization. Heat spreading occurs when heat flows through materials that have a change in cross-sectional area<sup>51</sup>, which in our case happens when heat flows between the outer PET films and the thermoelectric legs. The thermal resistance associated with heat spreading can be accounted for by modifying the heat transfer coefficient  $h$  resulting in a modified heat transfer coefficient  $h'$  given by<sup>27,51,52</sup>,

$$h' = \frac{1}{A_m R_{spr} + 1/h}, \quad (9)$$

where  $R_{spr}$  is the heat spreading resistance. One important factor affecting  $R_{spr}$  is thermal conductivity of the outer layer material, which in our case is PET<sup>51</sup>. Applying a high thermal conductivity material will dramatically decrease the heat spreading capacity and thus increase the overall power density. A possible approach is to coat a metal layer on the exterior of the PET layer to minimize heat spreading resistance. Combining Eqn. (4), (8) and (9), the maximum power density ( $p_{max}$ ) is given as,

$$p_{max} = \frac{h'^2 A_m (T_H - T_a)^2 S_{TE}^2 A_{TE}}{4(hA_m + G)^2 L \rho}. \quad (10)$$

In this analysis,  $T_H = 302$  K,  $T_F = 295$  K, and  $h = 5$  W m<sup>-2</sup> K<sup>-1</sup>. The heat transfer coefficient represents natural convection of a vertical plate in air with a modest temperature difference between  $T_C$  and  $T_F$ <sup>53</sup>.

Based on this analysis, we consider  $p_{max}$  with a variation in  $L$  and  $\alpha$  for the Ag–Ni elements with experimentally determined materials properties, with results given in **Figure 7**. It is important to note that conduction through the air cavity within the TE module is considered negligible in this analysis. This is a common assumption that does not typically have a large impact on performance. However, at small values of  $\alpha$ , conduction through the cavity may become a significant factor and caution in the accuracy of this assumption is warranted. Here, we find that for a constant  $L$ ,  $p_{max}$  increases as  $\alpha$  becomes larger as a result of the increase in thermoelectric element packing density (i.e. increased fill factor). If  $\alpha$  is held constant, there exists an optimal leg length ( $L_{opt}$ ) that results in  $p_{max}$ . In the experimental conditions,  $\alpha$  was approximately 41°, which would result in  $L_{opt}$  to be approximately 3 mm. For verification of the model, the experimental results with the same boundary conditions ( $T_H = 302$  K,  $T_F = 295$  K,  $h = 5$  W m<sup>-2</sup> K<sup>-1</sup>) are also plotted in **Figure 7**, and are shown to matched well with the calculated data. Differences between the model and experimental results may be associated with unaccounted for geometric variations, thermal contact resistances, and heat transfer coefficient.

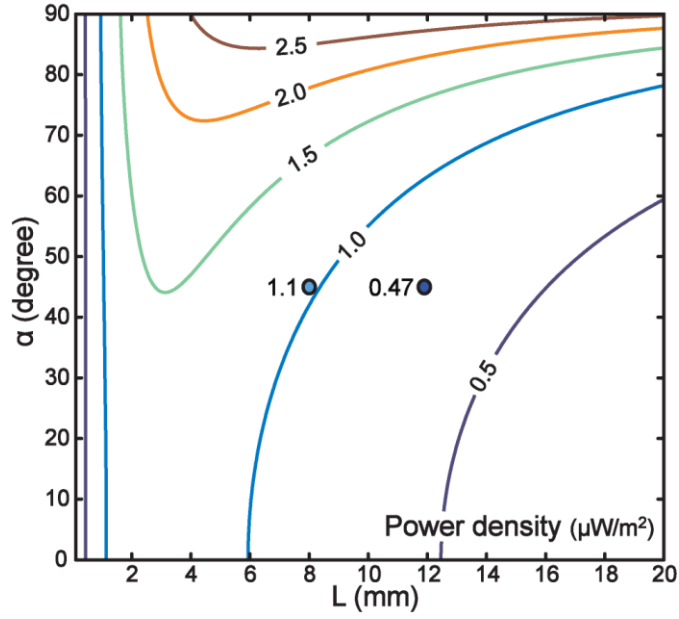


**Figure 7.** The theoretical maximum power density ( $p_{max}$ ) of a C-TEG module as a function of the thermoelectric couple leg length and leg angle ( $\alpha$ ) when employing the Ag-Ni couples under the heat sink limited conditions. Experimental maximum power density under the same boundary conditions for the fabricated devices is also provided (dots).

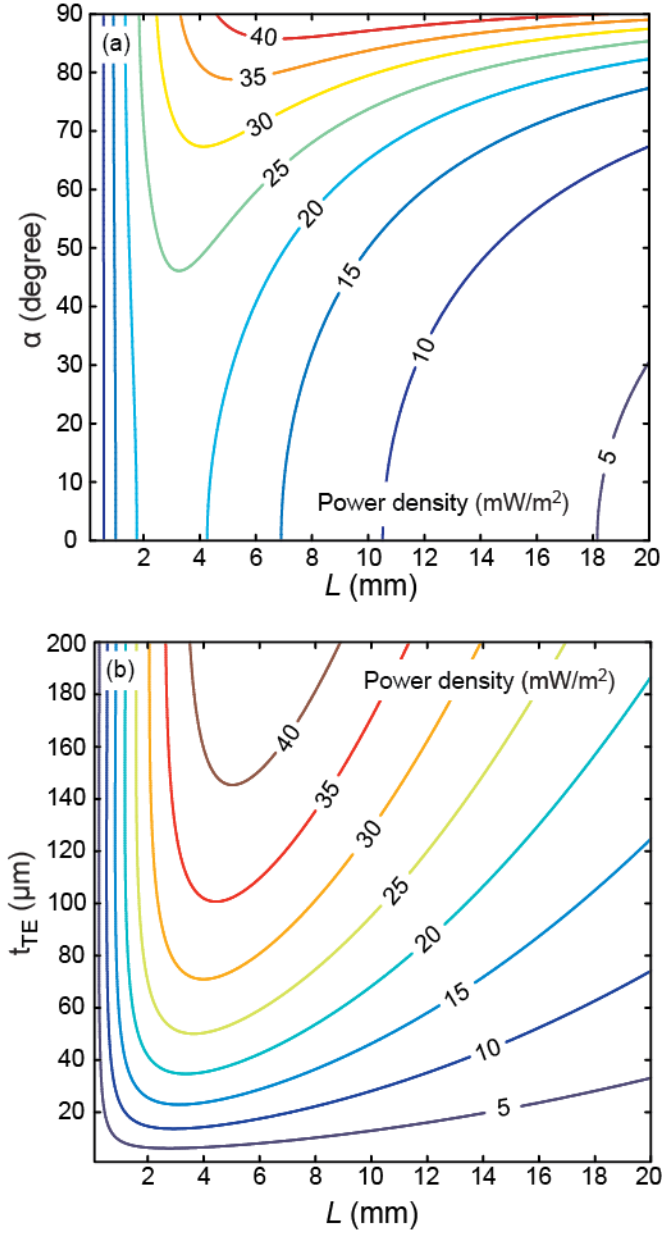


**Figure 8.** Geometric analysis of the maximum power density for a C-TEG based on Bi<sub>2</sub>Te<sub>3</sub> thermoelectric couples. (a) Power density as a function of leg length and leg stacking angle for a constant thermoelectric element thickness ( $t_{TE}$ ) of 75  $\mu\text{m}$ . (b) Power density as a function of leg length and  $t_{TE}$  for a C-TEG with a constant leg stacking angle ( $\alpha$ ) of 68°.

Thermoelectric materials with higher  $ZT$  should significantly improve the power generation of the C-TEG module. To consider the performance opportunity of the C-TEG design with advanced materials, we theoretically consider the performance with high performance  $\text{Bi}_2\text{Te}_3$  based elements. In this case we use  $S_{TE} = 236 \mu\text{V K}^{-1}$ ,  $\rho = 12.3 \mu\Omega \text{ m}$ ,  $\kappa = 0.57 \text{ W m}^{-1} \text{ K}^{-1}$ , resulting in a  $ZT$  value of approximately 2.38 at room temperature, similar to previous demonstrations<sup>16</sup>. While the thin film thermoelectric elements should aid flexibility, the  $\text{Bi}_2\text{Te}_3$  elements may not necessarily have the ability to flex during processing without fracture<sup>54</sup>. Nevertheless, the material is chosen to represent a realistic, high performance system that may be achieved with more compliant materials in the near future<sup>36,55</sup>. The power density of the module is given in **Figure 8(a)** with variation in  $L$  and  $\alpha$ , with  $t_{TE}$  held constant at  $75 \mu\text{m}$ , and in **Figure 8(b)** for a variation in  $t_{TE}$  and  $L$ , with  $\alpha$  held constant at  $68^\circ$  (which represents a shrink ratio of approximately 50%, in-place of the experimentally demonstrated 20%). The larger  $\alpha$  will increase the power density of the module, and the value chosen is based on a realistically achievable shrink ratio for drawn polymer films. A similar trend is found for  $p_{max}$  with variation in  $\alpha$  and  $L$  as observed with the metal TE elements. In **Figure 8(b)**, it is observed that the thickness of the thermoelectric elements increases the power out of the device but  $L_{opt}$  is found to be relatively constant. Due to the heat sink limited regime, at high  $\alpha$ ,  $L_{opt}$  is found to be larger than observed in the analysis of the metal TE couples resulting in greater compatibility with simple scalable processing. According to Mayer and Ram<sup>27</sup>, an excessively high packing density will result in reduced performance due to heat sink limitations. However, performance loss associated with excessive packing density is not observed in **Figure 8**. This is due to the packing limits inherent with the C-TEG design. The thermal conductance of the TE element is very small

due to the small thickness and long leg length, and the fill factor remains low even when  $\alpha$  is equal to  $90^\circ$  due to the spacing associated with the polyimide substrate ( $\sim 0.12$  mm) and adhesive ( $\sim 2$  mm). The substrate thickness will also have an effect on the power density  $p_{max}$  by increasing parasitic heat transfer with increasing thickness. The impact of substrate thickness has previously been investigated for a corrugated TE cooler<sup>49</sup>. It was found that the losses can be relatively low for moderate temperature differences across the module<sup>49</sup>.

Finally, for comparison, a conventional bulk thermoelectric (B-TEG) module with the same areal density of thermoelectric material ( $\text{kg m}^{-2}$ ) as the C-TEG under the same boundary conditions is considered. Here the B-TEG is considered with high thermal conductivity ceramic interface plates ( $\kappa = 150 \text{ W m}^{-1} \text{ K}^{-1}$ ), and TE elements without a substrate support. For a C-TEG with  $t_{TE} = 75 \text{ }\mu\text{m}$  and  $\alpha = 68^\circ$ ,  $L_{opt}$  is found to be 4 mm resulting in  $0.3 \text{ kg m}^{-2}$  of  $\text{Bi}_2\text{Te}_3$  and  $p_{max} = 31 \text{ mW m}^{-2}$ . Using a comparable areal density of TE material, the B-TEG will have a maximum power density of  $83 \text{ mW m}^{-2}$ . The difference mainly comes from the application of the high thermal conductivity interface plates on the B-TEG. Improving the thermal conductivity of the PET layer in the C-TEG with metal coatings or through embedded high conductivity particles will improve module performance and minimize any differences in performance. This suggests that the C-TEG can have performance comparable to B-TEG modules for similar thermoelectric element densities.

#### 1.2.4 Conclusion

In this paper, we experimentally demonstrated an innovative thermally formed thermoelectric device that employs thin film thermoelectric elements supported on a plastic substrate that are oriented in a corrugated fashion to resemble a conventional bulk thermoelectric architecture. The demonstrated Ag-Ni thermoelectric based devices were found to have a maximum output power of approximately 0.22 nW per couple when under a 7.0 K temperature difference. While there is slight performance degradation due to the processing approach, the performance is similar to other demonstrations of Ag-Ni thermocouples<sup>41</sup>. We then theoretically consider the performance of this system under a heat sink limited operating regime, finding that an optimal thermoelectric leg length between 3 and 4 mm occurs over a wide range of leg stacking angles, and an optimal power output of  $1.5 \mu\text{W m}^{-2}$  is found for a stacking angle similar to that experimentally demonstrated ( $\alpha = 40^\circ$ ). The theoretical results are then extrapolated to high performance thermoelectric materials showing that for a realistic shrink ratio of 50%, a power density of  $31 \text{ mW m}^{-2}$  can be achieved. This power output is similar to a bulk thermoelectric module for a comparable areal density of thermoelectric material. Further increases in performance are expected with implementation of thermal interface layers with higher thermal conductivity.

The results suggest that for low power density applications with low-quality waste heat, the heat shrink C-TEG module may provide a cost-performance advantage as compared to conventional TEs. This is due in-part to the simple heat-shrink approach that is compatible with low-cost, scalable fabrication methods. The geometric details of the C-TEG module can also be easily modified by varying the heat shrink ratio of the individual PET layers. This

includes the formation of cylindrical shapes<sup>40</sup>. This allows for application to non-planar geometries with the ability to optimize element packing density for a specific application.

## 1.3 Performance expectations of a woven thermoelectric generator

### 1.3.1 Introduction and motivation

Thermoelectric generators (TEGs) are a highly attractive energy conversion technology to capture waste heat given their thin form factor, and lack of moving parts<sup>16,56,57</sup>. One particularly attractive application of TEGs is in wearable electronics, where the TEG can reduce or completely replace an on-board battery to power the electronic devices.<sup>58–67</sup> Thus, there is a desire to develop thermoelectric (TE) materials and devices that are compatible with wearable technologies. For wearable TEGs it is important that the module can make low thermal resistance contact with the body, and that it is able to change shape in a way that is comfortable to the wearer. A highly attractive approach to achieve this goal is to integrate the thermoelectric elements directly into a woven textile<sup>67–74</sup>.

Thermoelectric elements can be integrated with textiles through connecting traditional and commercially available TEGs to a fabric, through impregnating TE elements into a fabric host<sup>67–69,71–74</sup>, or through processing the TE materials in a fiber form factor that is then woven into a fabric<sup>41,70,75</sup>, as shown in **Figure 9**. In these approaches, only the last approach is able to have fabric-like mechanical properties that will allow for seamless integration into a fabric – maximizing comfort and aesthetics. In the directly woven approach, the TE materials may be embedded into an insulating fiber host, or an insulating fiber can act at the substrate for the TE materials. In the later approach, Yadav et al. demonstrated a fiber TE couple by thermally evaporating silver (Ag) and nickel (Ni) onto one side of a silica fiber<sup>41</sup>. Liang et al. demonstrated a single leg glass fiber based TEG made of PbTe with both high performance as well as flexibility by using a solution-phase deposition method<sup>75</sup>. However, they both stopped at individual fibers without fabricating a textile module. More recently, Lee et al.

demonstrated the example of flexible woven TEG textiles based on electrospun polymer nanofiber coated with  $\text{Bi}_2\text{Te}_3$  and  $\text{Sb}_2\text{Te}_3$ <sup>70</sup>. The textile module was able to output  $0.856 \text{ mW/cm}^2$  with temperature difference of  $200^\circ\text{C}$  applied in the textile thickness direction. These demonstrations are very promising, and highlight the significant progress continuing to be made in this TEG approach. However, the performance expectations of such as design for wearable applications have not been established. In addition, with the goal of seamless integration into a fabric, the ability to efficiently reject the heat becomes a challenge<sup>69</sup>. The low heat rejection ability will cause heat accumulating at the cold side and eventually increase the cold side temperature ( $T_c$ ) and will dramatically damage the device performance. In high performing wearable thermoelectric from commercial elements, a large heat sink was employed. However, this method has the drawback of heavy, uncomfortable and potential bad contact, which makes it not applicable to woven TEG. Alternatively heat spreading to reduce the convective thermal resistance can be employed<sup>76,77</sup>. Heat spreading layer is widely used between large bulk heat sink and electronics component as well as TEG to ensure a good contact for heat dissipation<sup>76-78</sup>. For wearable TEG, it's more feasible to employ planar heat sink that in the same plane as the fabric part. By using high thermal conductivity fiber, the heat transferred from human body can be spread out to planar heat sink and rejected efficiently.

Here we show a fabric TEG design that is able to dissipate the heat efficiently and maintain a finite temperature difference between hot and cold side under heat sink limited conditions. This new design employs a corrugated structure that combines conventional bulk TE design and in-plane thin film TE device, as studied in previous research<sup>38,49,79,80</sup>. Employing this structure allows the heat go through the out of plane direction of the device to

be compatible with large area application, while at the same time go through the in plane direction of TE material so as to maintain a substantial temperature difference<sup>38,49,79,80</sup>. The heat dissipation is realized by transporting heat away from the cold side by highly thermal conductive fiber to a thin planar heat sink sheet. The heat sink sheet is fabricated into the TEG fabric patch to ensure a good integrity. Recently, Bahk et al.<sup>74</sup> and Suarez et al.<sup>69</sup> considered the performance expectations of a wearable thin film thermoelectric module that took a more conventional cross-plane thermoelectric geometry. Here, we would like to focus on a fiber woven structure and the geometric and materials considerations for this type of architecture. Furthermore, we have explored the needs for thermal spreading and rejection through an approach that is compatible with the woven fabric approach. And also, the feasibility analysis was conducted aimed at supplying power for wearable electronics. Unlike traditional electronics, wearable electronics especially self-powered electronics needs to be designed to consume much less power for sustained operation. And this is usually achieved by integrating electronics onto a single system on chip (SoC)<sup>81,82</sup>. By using this technique, the power consumption can be reduced to tens of micro watts and can be easily powered by TEG<sup>81,82</sup>. And differed from other applications, wearable TEG needs to be area-effective due to the limited space in human body, and one needs to consider not only the performance (higher  $T_h$ ) but also the wearer's comfort level. The overall human skin surface area is around 1.9 m<sup>2</sup>, however there are only certain parts that are suitable for TEG. Usually head and trunk have a higher skin temperature than legs, arms and feet, which can produce more power. While arms have an advantage of improving heat rejection by increasing the heat convection coefficient while walking and swinging. The skin area for this suitable area (i.e. trunk and arms) is about 1 m<sup>2</sup> and this will be the limit for effective TEG harvesting.

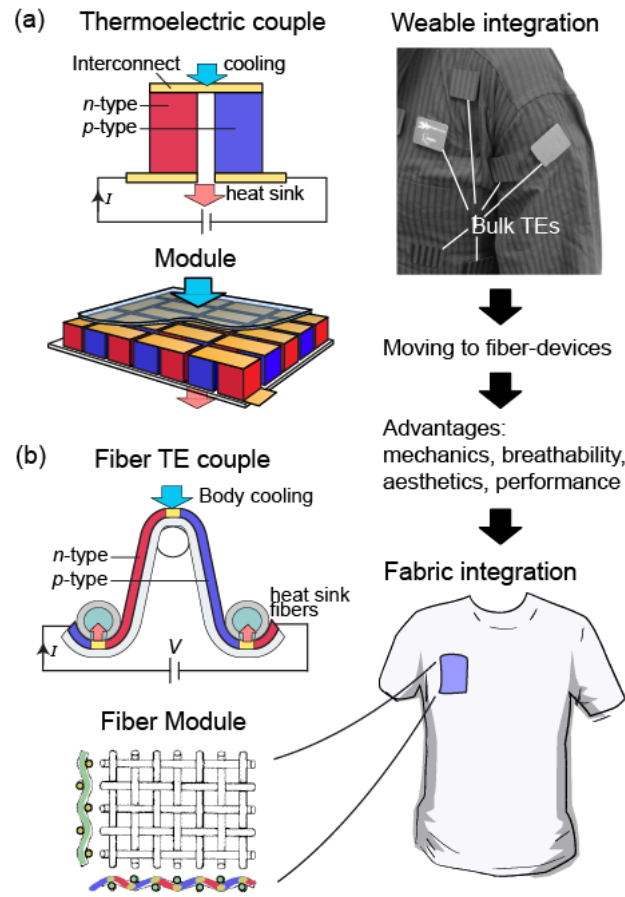


**Figure 9.** Approaches to wearable TEG through (a) integration and (b) woven fabric

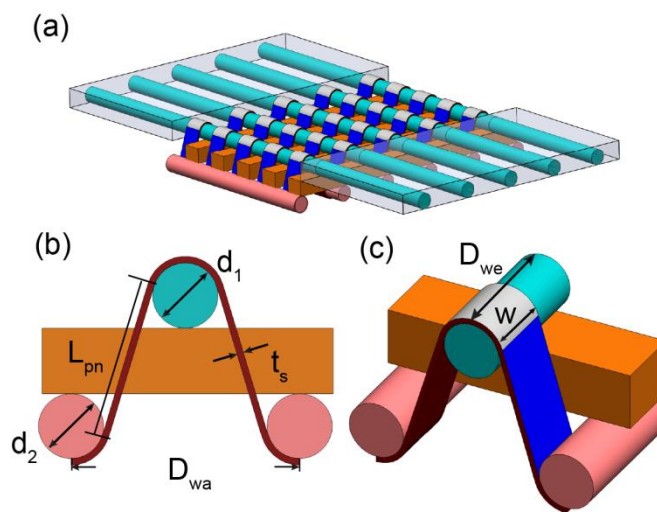


**Figure 10.** Schematic of (a) the textile TEG patch, (b) one unit of woven TEG and (c) side view of one-unit textile TEG

### 1.3.2 Device architecture and material properties

There are many possible weave patterns for a fiber based TEG<sup>70</sup>. Here, we focus on a modified plain wave design illustrated in **Figure 10**. This design captures many of the structural features that will dictate performance in various weave patterns, including spacing of elements, parasitic losses from insulating fibers, and means of heat spreading and rejection. In this architecture, the TE material is deposited onto a thin square fiber substrate (TE fiber) and connected by metal interconnection. The TE fibers are then woven between two round fibers. The direction that TE fibers lie along is called the weft direction and warp direction for the perpendicular one<sup>70</sup>. Supporting square fibers with relatively high stiffness are placed between every two TE fibers in the weft direction and between the two round fibers to sustain the whole structure and to maintain the weave geometry when an external force is applied on the device. They are also served as a spacer/insulator to prevent the potential shorting between TE materials. Finally, the top fibers act as thermal transport materials, to spread the heat laterally for improved heat rejection – by increasing the convective heat transfer surface area. Additional details of the heat sink design considerations are provided below.

To explore the potential opportunity of this new structure, a TE couple with a high ZT value of approximately 1 at room temperature is chosen in this analysis, with Seebeck coefficient ( $S_{TE}$ ) = 100  $\mu$ V/K, electrical resistivity ( $\rho_{TE}$ ) = 10  $\mu\Omega$  m and thermal conductivity ( $\kappa_{TE}$ ) = 0.3 W/mK. The TE fiber, top fiber, bottom fiber and supporting fiber are all considered to be electrical insulators ( $\rho = \infty$ ). For a TEG device design, it's important to force the heat to go through the TE material as much as possible, and at the same time reject the heat away from the cold side efficiently to maximize the temperature difference across the

TE couples. Therefore, a low thermal conductivity value of 0.03 W/mK based on the polyacrylonitrile (PAN)<sup>83</sup> are assigned to the supporting fiber and bottom fiber, and high thermal conductivity of 1000 W/mK is chosen for the top fiber. A more detailed analysis related to the high thermal conductivity fiber will be shown later.

### 1.3.3 Analytical model

The basic model for analyzing conventional bulk TEG performance in the limited heat sink condition has been established in the previous study<sup>27</sup>. In that case, the parasitic heat loss through the air is usually neglected and the thermal resistance network is merely a simple circuit with convection resistance ( $R_c$ ) in series with TE resistance ( $R_{TE}$ ). The temperature difference ( $\Delta T_{TE}$ ) applied on the TE element can be simply obtained by equating the heat leaving the TE leg cold side to the one entering the heat sink<sup>27</sup>. And then the output power or power density can be calculated using the following equation,

$$P = \frac{(nS_{TE}\Delta T_{TE})^2 R_o}{(R_i + R_o)^2}, \quad (11)$$

in which  $n$  is the number of the TE couples,  $S_{TE}$  is the combined Seebeck coefficient of TE couples,  $R_o$  is the load electrical resistance and  $R_i$  is the internal electrical resistance. When the  $R_o$  matches with  $R_i$ , the output power reaches the maximum value, and is given by

$$P_{max} = \frac{(nS_{TE}\Delta T_{TE})^2}{4R_i}, \quad (12)$$

and the maximum power density ( $p_{max}$ ) is given by

$$p_{max} = \frac{(nS_{TE}\Delta T_{TE})^2}{8R_i A}, \quad (13)$$

where  $A$  is the occupied area. Internal electrical resistance is determined by TE dimension and electrical property and is given by

$$R_i = \rho_{TE} \frac{L_{TE}}{w_{TE}t_{TE}}, \quad (14)$$

where  $\rho_{TE}$  is the combined electrical resistivity of TE couple,  $L_{TE}$  is the leg length,  $w_{TE}$  is the TE couple width and  $t_{TE}$  is the TE couple thickness. However, in our woven TEG architecture,  $\Delta T_{TE}$  cannot be obtained by only solving one equation due to the higher complexity of the structure. In this structure, since there is no cover on the top, the air convection not only happens at the cool side of TE leg but also at each surface open to the air, such as the surface of TE element ( $R_{c-TE}$ ), the upper surface of bottom fiber ( $R_{c-bottom}$ ), supporting fiber ( $R_{c-frame}$ ) as well as top fiber ( $R_{c-top}$ ) where is not covered by TE fiber. Besides, the parasitic loss from the bottom fiber ( $R_{bottom}$ ), supporting fiber ( $R_{frame}$ ), air ( $R_{air}$ ) as well as contact resistance ( $R_{con-bottom}$  and  $R_{con-substrate}$ ) are also considered in this model. **Fig. 11(a)** shows the simplified thermal resistance network of this woven TEG structure. The stable temperature as a boundary condition is assumed to be at the inner surface of the skin, and the skin resistance both in the vertical ( $R_{skin-noncon}$  and  $R_{skin-con}$ ) as well as laterally ( $R_{skin-h}$ ) direction are also considered. In this case, to simply the model, all the heat transportation is considered to be one-dimensional. Then this complex circuit is further reduced to one single equivalent resistance and one equivalent voltage in series with TE/substrate resistance using Thevenin theorem. This allows one to isolate the TE element out of the complicated circuits and be able to calculate the temperature difference applied between TE legs and eventually calculate the maximum power density using Eqn. (13).

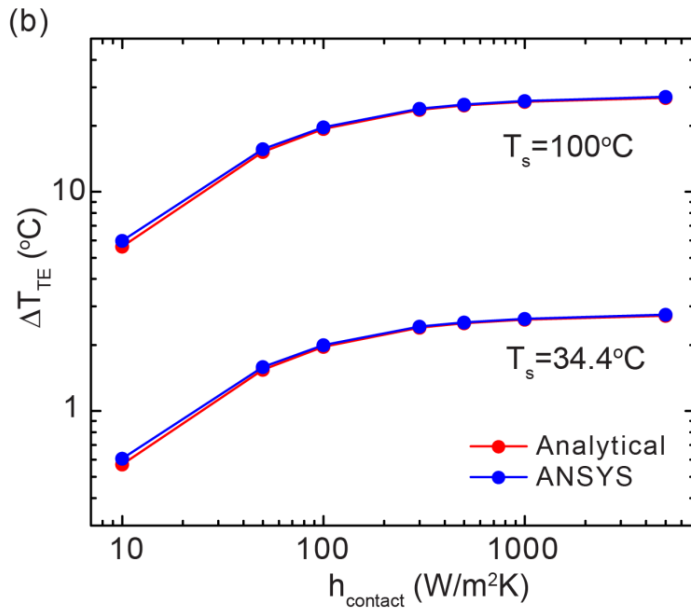
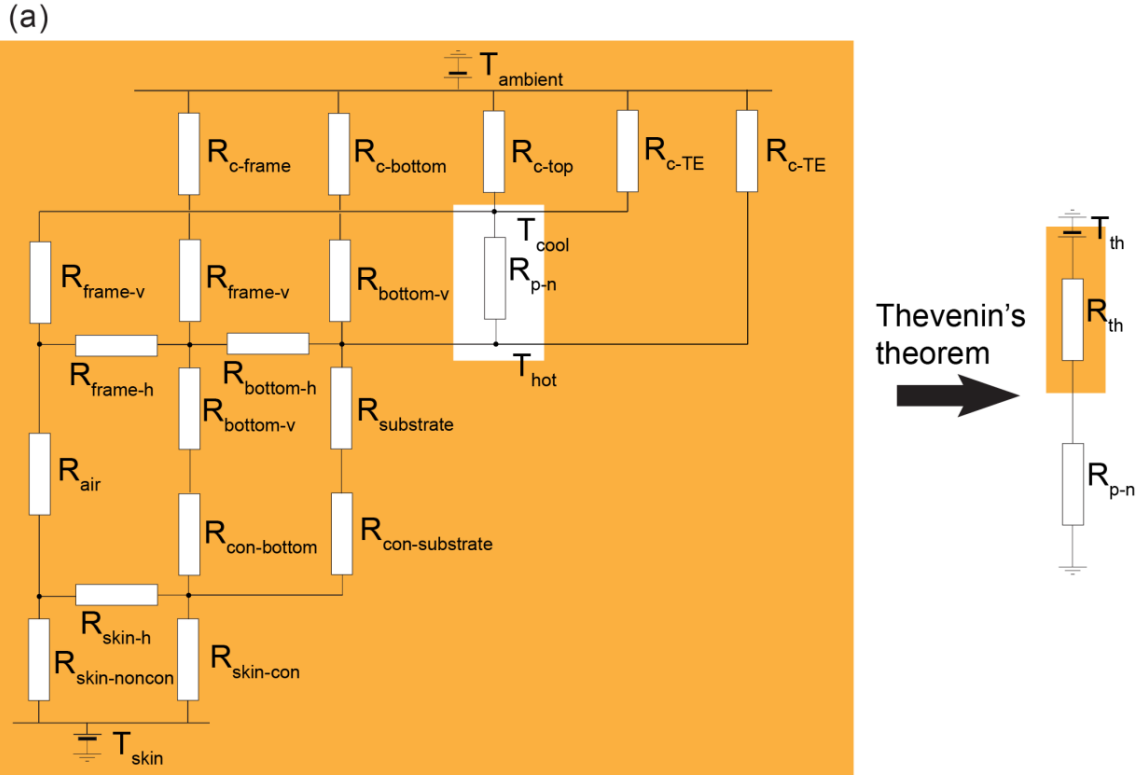


**Figure 11.** (a) Thermal resistance network for analytical model and (b)  $\Delta T_{TE}$  as a function of contact resistance coefficient  $h_{con}$  for both Analytical model and Finite Difference method (ANSYS).

The maximum power density for one single TE couple with different contact resistance ( $R_{con}$ ) was first investigated using both analytical model and finite element numerical simulation (ANSYS). As one major thermal loss for wearable TEG,  $R_{con}$  mainly comes from poor contact between TEG and human skin<sup>84</sup>. The contact resistance can be expressed using heat transfer coefficient  $h_{con}$  in the following equation

$$R_{con} = \frac{1}{h_{con}A_{con}}, \quad (15)$$

where  $A_{con}$  is the contact area. In this analysis, the dimension of TE leg is chosen with TE leg length  $L_{TE} = 2.5$  mm, TE leg width  $w_{TE} = 0.5$  mm, and TE leg thickness  $t_{TE} = 10$   $\mu$ m. The dimension of fabric structure is chosen with top fiber diameter  $d_1 = 0.3$  mm, bottom fiber diameter  $d_2 = 0.3$  mm, TE substrate fiber thickness  $t_s = 0.1$  mm, stacking angle  $\theta = 90^\circ$  and length along wasp direction for one-unit  $D_{wa} = 1$  mm. The heat sink ratio  $x$ , which is defined as

$$x = A_{ex}/A_p, \quad (16)$$

where  $A_{ex}$  is the surface area of the heat sink sheet and  $A_p$  is the projected area of one TE couple, is set to 0 here, which means no heat sink is connected. The other dimensions can then be determined based on above-mentioned dimensions. The dimensions chosen here are optimal geometry that will potentially result in a higher performance based on geometry analysis that will be shown in the later text. The boundary condition is chosen with heat convection coefficient  $h_c = 5$  W/m<sup>2</sup>K and ambient temperature  $T_a = 27$  °C.

Initially, the results from analytical model and simulation method with the same boundary conditions show a small difference, and this variation seems to be a function of angle  $\theta$  and also associated with contact thermal coefficient  $h_{con}$ . In order to reduce the error of analytical model and better match with simulation result, the contact thermal resistance is

multiplied by a coefficient as a function of  $\theta$ , and the results of modified analytical model as well as ANSYS is shown in **Figure 11(b)**. It shows that  $\Delta T_{TE}$  from analytical model increases from about 0.6 °C to 1.2 °C when  $h_{con}$  increase from 10 W/m<sup>2</sup>K to 1000 /m<sup>2</sup>K with the skin temperature ( $T_{skin}$ ) of 34.4 °C and it matches well with result from ANSYS. This result indicates the contact resistance has a significant impact on the temperature difference across TE leg and eventually on TEG performance. To further validate the analytical model, a different boundary condition with temperature of 100 °C instead of 34.4 °C is employed and the results from the two methods are still found to match well. This validated the effectiveness of proposed analytical model and further geometry analysis and feasibility analysis is ready to perform with this model.

### 1.3.4 Results and discussion

#### *Geometry analysis*

For a certain geometric design, it is important to perform geometry analysis to explore the potential variables for obtaining the best performance. For wearable applications, it is necessary that we capture realistic boundary conditions. The temperature difference across the TEG is expected to be relatively small, the purposefully pulling a high thermal flux through the TEG will result in an undesirable cold sensation<sup>74</sup>. The skin temperature also can be different at different locations<sup>85</sup>. Here, we adopt the boundary conditions at human chest, where the skin temperature is set to be 34.4°C at the ambient temperature of 27°C. And the contact thermal coefficient between skin and surface of TEG  $h_{con}$  is set to be 50 W/m<sup>2</sup>K. For wearable application, it is unrealistic and undesirable to apply a forced convection heat sink or other medium like water. Therefore in this study, a natural convection through air is

assumed as the heat sink boundary condition and the heat convection coefficient  $h_c$  is set to be 5 W/m<sup>2</sup>K.

Here we first study the single unit of this TE fiber device's performance based on different TE geometry under limited heat sink condition and the results are shown in **Figure 12(a)** and (b). Here two power density values are calculated based on different occupied area. One is defined as

$$p_{max} = P_{max}/A_p, \quad (17)$$

and the other one is defined as

$$p'_{max} = P_{max}/(A_p + A_{ex}). \quad (18)$$

$p_{max}$  provides the information about the performance of only TE element, while  $p'_{max}$  represent the performance of the whole device. They have a relationship that can be described as

$$p'_{max} = p_{max}/(1+x). \quad (19)$$

This allows one to capture not only the performance of TE element, but also focus on the area consumption of the whole device. The result shows that for each heat sink condition, there exists an optimal leg length that results in the maximum power density. In this case, the combined thermal resistance of TE couple and TE substrate matches with the equivalent resistance  $R_{th}$ , and the temperature drop across the TE leg is almost half of the equivalent voltage  $T_{th}$ , based on the thermal impedance match theory <sup>27</sup>. For  $x = 0$ , the optimal  $L_{TE}$  is found to be around 2.5 mm and  $p_{max}$  (same as  $p'_{max}$  when  $x=0$ ) of 2.16 mW/m<sup>2</sup>. This value is lower than that of TEG made of bulk material mainly due to smaller packing density and smaller temperature difference across TE leg. The packing density of TE material ( $C$ ) is defined as,

$$C = \frac{t_{TE}W_{TE}}{Ap}. \quad (20)$$

For the normal bulk TEG, usually  $C$  is at a value of about 25%, while in our case it varies from 0.05% to 4.7% depending on what TE and fiber dimensions are chosen. Since for a thin film device, which employs the in-plane direction properties of the material and the substrate is always inevitable, finding an efficient approach to improve  $C$  will be necessary to achieve a good  $p_{max}$ . It also found that both  $p_{max}$  and  $p'_{max}$  are almost linear with the TE thickness within the chosen range. This is mainly because the increasing packing density associated with the increment of  $t_{TE}$ .

Unlike the traditional bulk TEG, the geometry of this fabric TEG is more complicated due the evolvement of fabric fibers. To better understand how the fabric part will influence the TEG performance, it's necessary to perform analysis based on both fiber geometry as well as fiber property. The power density as a function of each fiber geometry is shown in **Fig. 12(c)-(f)**. It is found that  $p_{max}$  decreases with increasing  $d_1$ , and  $t_s$ , and decreasing  $\theta$ . This is mainly a result of different packing density, that with the smaller dimension of each fiber, the packing density of the TE element will increase. Besides, it is also found that  $p_{max}$  drops more with increasing  $t_s$  than  $d_1$  due to the deduction of the combined thermal impedance of the TE/TE substrate also associated with the increasing  $t_s$ . On the other hand,  $p_{max}$  reaches the maximum value at the certain optimal  $d_2$ , which is the result of trade-off impact on  $d_2$  by contact resistance and packing density.

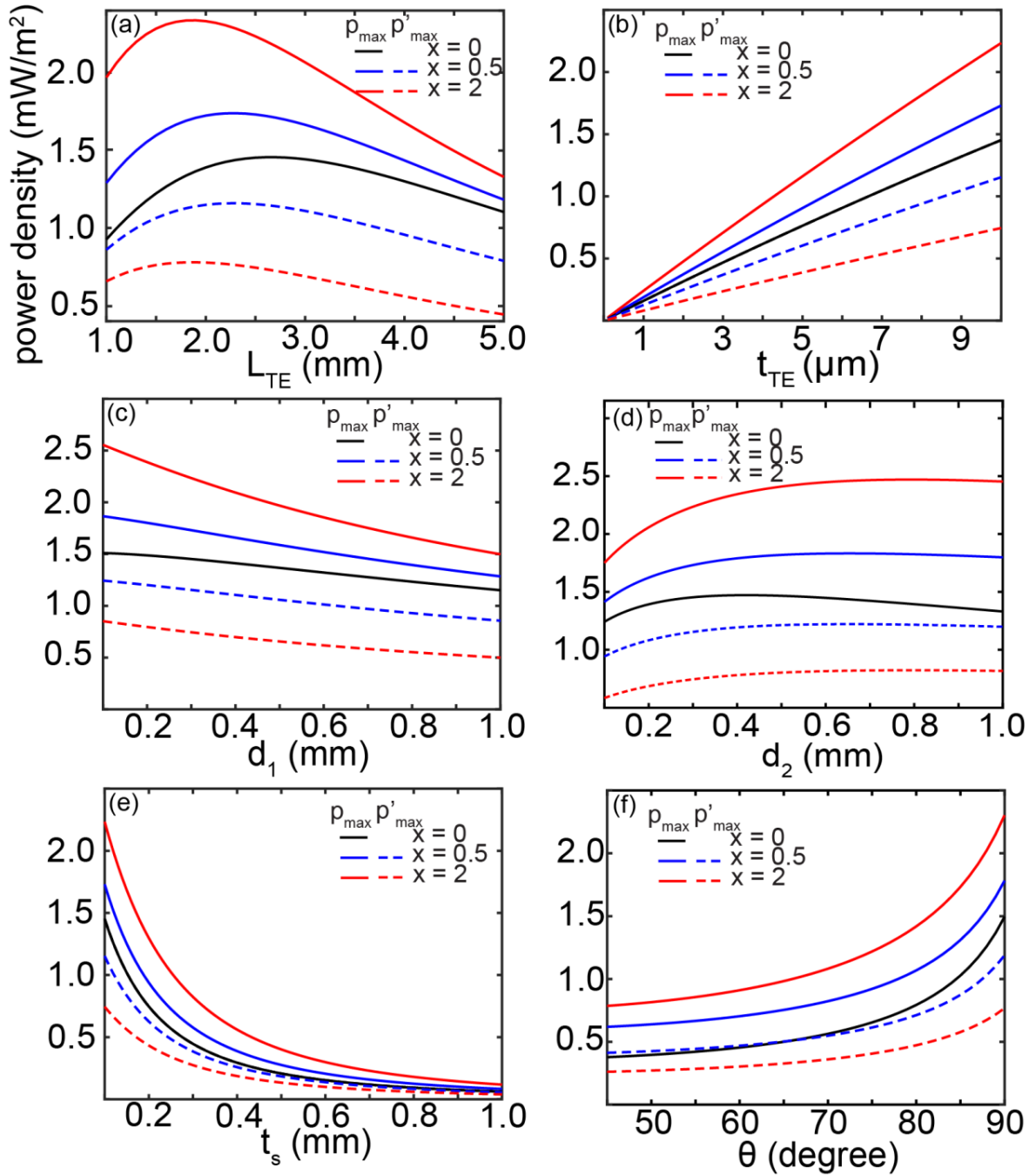


**Figure 12.** Output power density as a function of (a) TE couple leg length, (b) TE couple thickness, (c) top fiber diameter, (d) bottom fiber diameter (e) TE fiber thickness and (d) TE fiber angle with different heat sink area ratio.

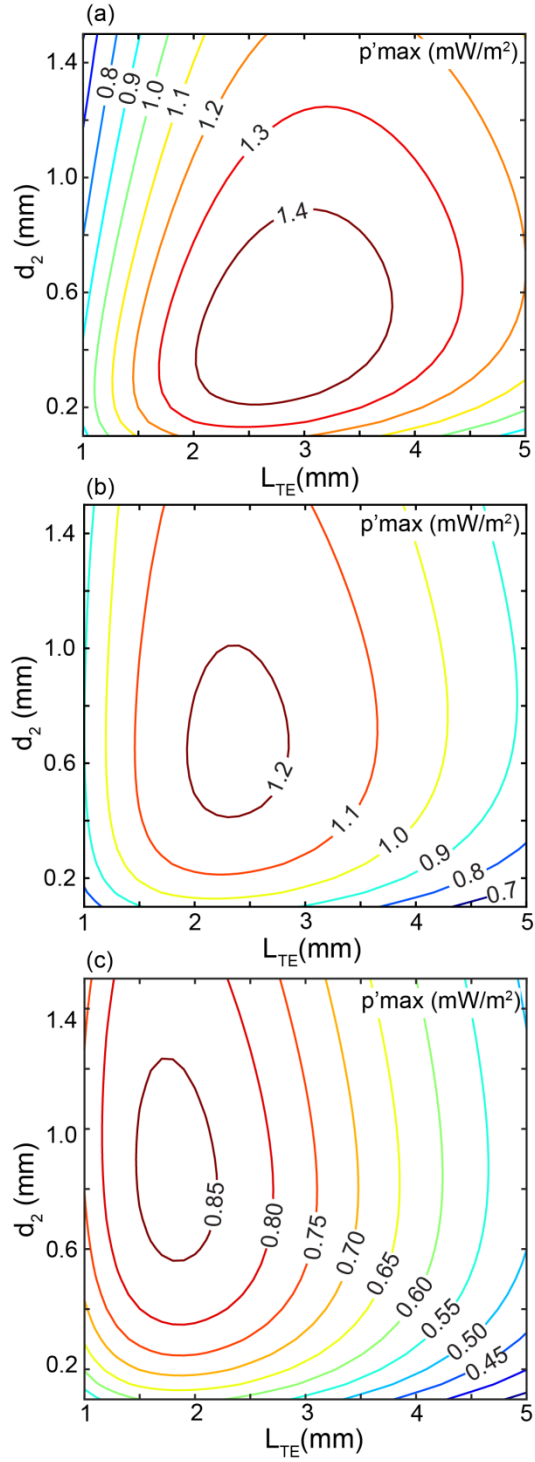


**Figure 13.** Power density as a function of TE leg length and bottom fiber diameter with heat sink ratio of (a) 0, (b) 0.5 and (c) 2.

The above analysis shows that the TEG performance follows a single trend for some parameters ( $d_1$ ,  $\theta$ ,  $t_s$  and  $t_{TE}$ ) while possesses the maximum value with others ( $d_2$  and  $L_{TE}$ ). Here we plotted the power density as a function of both  $L_{TE}$  and  $d_2$  to find the most optimal geometry at a certain boundary condition with  $h_c = 5 \text{ W/m}^2\text{K}$  and different  $x$  and the result is shown in **Fig 13**. The other parameters are chosen with  $d_1 = 0.3 \text{ mm}$ ,  $\theta = 90^\circ$ ,  $t_s = 0.1 \text{ mm}$  and  $t_{TE} = 10 \text{ um}$ . The results show that when  $x = 0$ , the optimal  $p'_{max}$  of  $1.48 \text{ mW/m}^2$  happens when  $L_{TE} = 2.8 \text{ mm}$  and  $d_2 = 0.45 \text{ mm}$ . As  $x$  increases, optimal  $L_{TE}$  is found to decrease while  $d_2$  increase. This phenomenon can still be explained by thermal-impedance match theory, although, instead of equating two terms-thermal resistances of TE leg and heat sink-, three terms which include the contact thermal resistance are believed to match with each other to reach the maximum power density. In this case, for a given heat sink condition ( $h_c$ ), the optimal  $L_{TE}$  and  $d_2$  determine a similar thermal resistance among TE leg, heat sink and skin contact and eventually result in the best performance. This finding is important and helpful to optimize the design when both hot and cool side of TEG is unable to maintain a stable temperature boundary condition.

The fibers also provide a potential path for the heat loss. To determine if this will have a substantial effect on the performance, we conducted the performance analysis with different thermal conductivity of the bottom fiber ( $\kappa_b$ ) and supporting fiber ( $\kappa_f$ ). The result shows that the performance loss is less than 8% even when both the  $\kappa_b$  and  $\kappa_f$  go up to  $5 \text{ W/mK}$ . This value is much higher than the thermal conductivity of common textile material<sup>86</sup>. Therefore, the parasitic loss from the bottom and supporting fiber can be neglected in this fabric TEG.

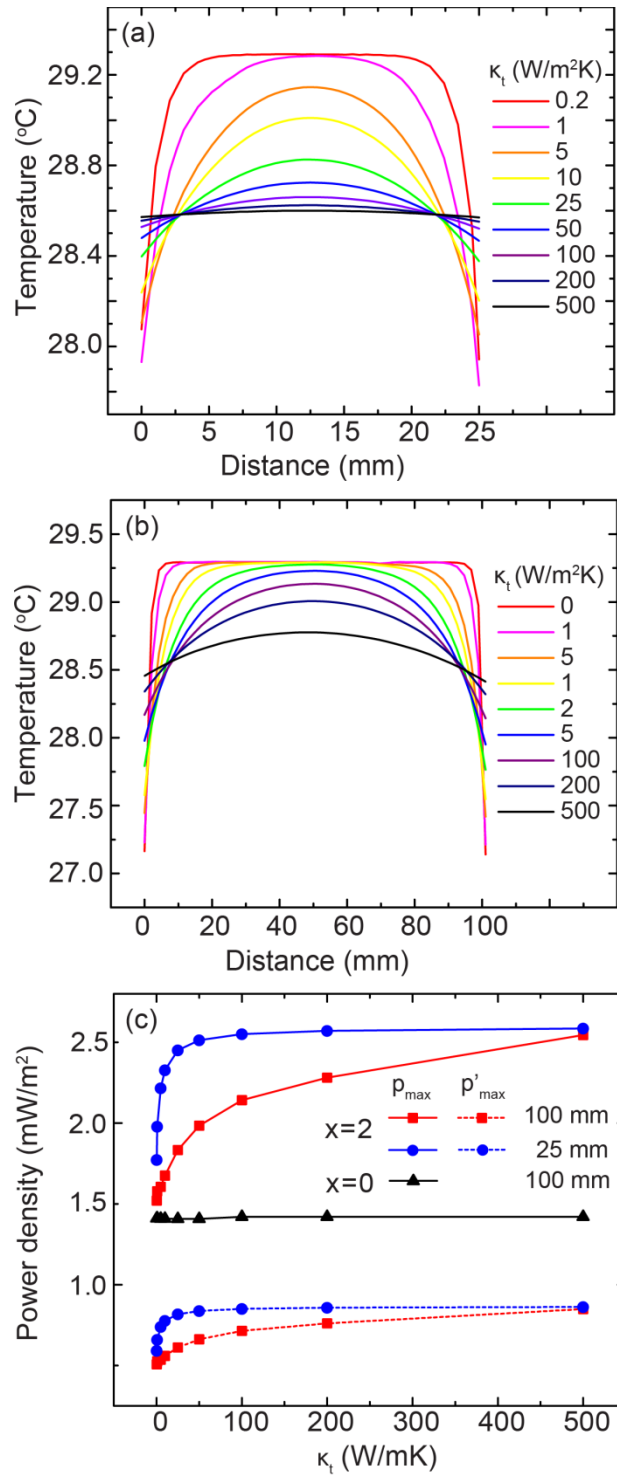


**Figure 14.** Temperature profile of the top fiber for various top fiber thermal conductivity ( $\kappa_t$ ) for a top fiber length ( $L_t$ ) of (a) 25 mm and (b) 100 mm. (c) Power density as a function of  $\kappa_t$  for various of  $L_t$  and  $x$ .

### ***Thermal conductive fiber analysis***

TEG with stronger heat dissipation power would significantly increase the  $\Delta T_{TE}$  and improve the output power density. Unlike other TEGs which are usually parallel connected to the heat sink on the top of the cold side, we employ high thermal conductivity fiber to transport heat to the heat sink which is connected with TEG in a series manner. Therefore, it would be important to explore the top fiber's thermal conductivity's ( $\kappa_t$ ) effect on  $\Delta T_{TE}$  and power density. This analysis is conducted by FEM using ANSYS Workbench. The geometry for FEM is chosen with the  $d_1 = d_2 = 0.3$  mm,  $L_{TE} = 2.5$  mm,  $w_{TE} = 0.5$  mm,  $t_{TE} = 10$   $\mu$ m,  $t_s = 0.1$  mm,  $\theta = 90^\circ$  and  $x = 2$ . The boundary condition assumes that the TEG is placed on the human skin with surface temperature of  $34.4^\circ\text{C}$  and ambient temperature of  $27^\circ\text{C}$ . The heat convection coefficient  $h_c$  is assumed to be  $5$   $\text{W}/\text{m}^2\text{K}$  and contact heat transfer coefficient  $h_{con}$  is  $50$   $\text{W}/\text{m}^2\text{K}$ . The temperature profile for top fiber with different thermal conductivity ( $\kappa_t$ ) is first shown in **Fig. 14**. In **Fig. 14(a)**, it shows at low  $\kappa_t$ , the temperature in the middle of top fiber is about  $29.2$   $^\circ\text{C}$ , while  $27.8$   $^\circ\text{C}$  at the end where near the heat sink sheet. This suggests the heat transferred from the hot side mostly accumulates in the top fiber and is unable to transfer to the heat sinks for an efficient heat rejection. With the  $\kappa_t$  increasing, the middle of temperature curve start to drop down and the temperature at the end of fiber start to increase. This trend of temperature-distributed uniformity indicates more heat is transferred to the heat sinks. When  $\kappa_t$  is above  $100$   $\text{W}/\text{mK}$ , temperature difference along the top fiber becomes very small and goes below  $0.1$   $^\circ\text{C}$ . And we call this  $\kappa_t$  the optimal thermal conductivity ( $\kappa_{t_{opt}}$ ). In this case, the TE couple and heat sink are well thermally connected and  $\Delta T_{TE}$  is mainly limited to the heat sink capability to dissipate heat. It is also found that  $\kappa_{t_{opt}}$  will vary based on the top fiber length ( $L_t$ ). A bigger  $L_t$  between the heat sink sheets usually requires a higher

$\kappa_{fopt}$  and vice versa. For a structure with a  $L_t$  of 100 mm, even with  $\kappa_t$  equal to 500 W/mK, temperature gradient still exists in the top fiber along the length direction as shown in **Fig. 14(b)**, while for the smaller  $L_t$  of 25 mm, a  $\kappa_t$  of 100 W/mK is enough.

The inability to transport heat to the heat sink efficiently due to the low thermal conductivity of top fiber will dramatically reduce the performance of the TEG device by holding back  $\Delta T_{TE}$ . The power density as a function of  $\kappa_t$  is plotted in **Fig. 14(c)**.  $p_{max}$  with  $x = 2$  at low  $\kappa_t$  is almost equal to  $p_{max}$  with  $x = 0$ . When  $\kappa_t$  increases,  $p_{max}$  for  $L_t = 25$  mm reaches the optimal condition at  $\kappa_t$  equal to 100 W/mK, while the one for  $L_t = 100$  mm can only be maximized until  $\kappa_t$  above 500 W/mK. It's also found the  $p_{max}$  for  $x = 0$  is almost independent of  $\kappa_t$ . This is expected because in this case, the heat doesn't need to transfer in top fiber laterally much before it can be rejected from the top fiber surface.

### ***Feasibility analysis***

To gain more insight into the fabric TEG, a feasibility analysis for the TEG to power wearable electronics with different power consumption ( $P_a$ ) is conducted. The dimensions of TE material and fibers are chosen with which the maximum power density can be achieved based on previous analysis. Here, we use overall TEG/heat sink area ( $A_{overall}$ ) needed to power the wearable electronics to characterize the feasibility of this fabric TEG. The overall area needed ( $A_{overall}$ ) for powering the sensor is given by,

$$A_{overall} = \frac{P_a}{p'_{max}}. \quad (21)$$

The results of  $A_{overall}$  as a function of  $x$  are shown in **Figure 15**. It shows that  $A_{overall}$  is minimum at  $x = 0$ , and increase with the increasing of  $x$ . The difference due to the effect of thermal conductivity of top fiber  $\kappa_t$  is also shown in the figure as the colorful band. The

boundary of the band corresponds to the limit  $\kappa_t$  of 1000 W/mK and 0.01 W/mK respectively. It clearly shows that  $A_{overall}$  can vary significantly with different  $\kappa_t$ , indicated by the bandwidth, and a big  $x$  usually results in a big variation.

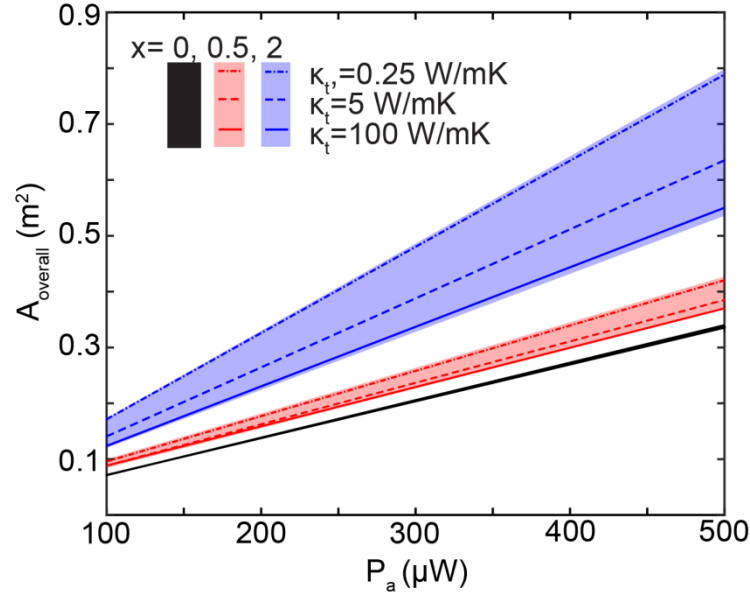


**Figure 15.** Overall area ( $A_{overall}$ ) needed as a function of target output power ( $P_a$ ) for various heat sink ratio ( $x$ ) and top fiber thermal conductivity ( $\kappa_t$ ).

The feasibility analysis above is based on the conservative assumption and it's important to ensure that the hypothetical parameters are realistic to manufacture or achieve. In this case, the minimum  $A_{overall}$  is around 0.1 m<sup>2</sup> for 100 μW device, which is a relatively big area. However it has the potential to be further improved with the development of science and technology, and therefore it's also important to explore such limitation under the most ideal condition. With this purpose in mind, another feasibility analysis is conducted based on the ideal yet maybe unrealistic parameters, with  $ZT = 2$ ,  $L_{TE} = 2.5$  mm,  $d_1 = 0.3$  mm,  $d_2 = 0.5$  mm,  $t_{TE} = 50$  μm,  $t_s = 0$ ,  $\theta = 90^\circ$ ,  $x = 0$ ,  $h_c = 4.8$  W/m<sup>2</sup>K. The result shows the power density can reach 88.6 mW/m<sup>2</sup> and  $A_{overall}$  can be reduced to 56 cm<sup>2</sup> to power a 500 μW wearable electronics. This can be easily applied at most skin region in human body. The result

suggests that this woven TEG design is feasible and can be potentially applied on human body served as power source for wearable electronics.

### 1.3.5 Conclusion

We theoretically investigated a fabric TEG that employs thin film TE material deposited onto a square fiber that woven into a plain weave fashion with two other fibers at top and bottom. We first conducted the performance analysis under limited heat sink condition where heat dissipated by natural convection with air. In this case, the highly thermally conductivity is applied for the top fiber in order to transport heat to heat-sink sheet efficiently. The performance is shown to be sensitive to fabric geometry parameters such as TE couple leg length ( $L_{TE}$ ), TE couple thickness ( $t_{TE}$ ), top fiber diameter ( $d_1$ ), bottom fiber diameter ( $d_2$ ), TE fiber thickness ( $t_s$ ), angle of the TE fiber ( $\theta$ ), and heat sink parameters such as heat convection coefficient ( $h_c$ ) and added heat sink ratio ( $x$ ). For a long top fiber length of 100 mm, the thermal conductivity of top fiber ( $\kappa_t$ ) needs to reach at least 500 W/mK to make sure the heat can be transport to heat sink efficiently to maximize the power density. Reducing the top fiber length to 25 mm can help reduce the requirement of  $\kappa_t$  to below 100 W/mK. Then the feasibility by harvesting human body waste heat energy using this TEG based on conservative and ideal condition is conducted. The results show that with further improvement, this woven TEG has the potential to power a 500  $\mu$ W electronics with only an area of about 56 cm<sup>2</sup>. This suggests this fabric TEG may be advantageous in human being application and served as a reliable approach to power future wearable electronics.

## 1.4 Summary and potential future work

### 1.4.1 Summary of present work

Thermoelectric generator device has been proposed for almost 50 years and is struggling to be widely commercially adopted. While chasing a high-performance material is one way to improve the efficiency TEG, reducing the fabrication cost is the key to broaden its application. And a rational design can contribute to both high performance as well as cost reduction. In this work, we showed an innovative approach to fabricate the thin film TEG with corrugated architecture by using a heat-shrink fabrication process. We then theoretically consider the performance of this device architecture with high performance thermoelectric materials in the heat sink limited regime. The results show that the heat-shrink approach is a simple fabrication method that may be advantageous in large-area, low power density applications. The fabrication method is also compatible with simple geometric modification to achieve various form factors and power densities to customize the TE generator for a range of applications. We then apply the corrugated structure to woven fiber that can be used to power the wearable electronics by reusing the waste heat generated from human body. The performance of this woven TEG is theoretically analyzed under limited heat sink condition, in which the rejected heat is dissipated by thermal convection through the top fiber and connected heat sink sheet. The results show that the max output power density is sensitive to the packing density, heat sink condition and thermal conductivity of the top fiber. The feasibility shows this fabric TEG has the potential to power a 500  $\mu\text{W}$  electronics with an area of about 56  $\text{cm}^2$ . This suggests this fabric TEG may be advantageous in human being application and served as a reliable approach to power future wearable electronics.

#### **1.4.2 Suggestion for future work**

The corrugated TEG is sensitive to the structure geometry. Therefore, further optimization can be made in reducing the substrate thickness, increasing the film thickness and increasing the contraction angle. It also shows a reduction of electrical property at the bending junction, therefore employing a more flexible material such as conductive polymer should provide better mechanical properties.

## 2 Stretchable organic semiconductors

### 2.1 Introduction

#### 2.1.1 Conductive polymer

The first conductive polymer (CP), polyaniline, was described in 1862 by Henry Letheby<sup>87</sup>. After more than 100 years, Alan J. Heeger, Alan MacDiarmid and Hideki Shirakawa reported a high conductivity polymer, polyacetylene doped with iodine, which started the modern study on the conduction mechanism of conductive polymer, and this achievement was awarded the 2000 Nobel Prize in Chemistry for the discovery and development of conductive polymer (**Figure 16**)<sup>88,89</sup>.

### The Nobel Prize in Chemistry 2000



Alan J. Heeger  
Prize share: 1/3



Alan G. MacDiarmid  
Prize share: 1/3



Hideki Shirakawa  
Prize share: 1/3

**Figure 16.** The Nobel Prize in Chemistry 2000<sup>88</sup>.

The conductive polymer is a special group of polymers that possess alternating single and double bonds or aromatic rings in their backbones (**Figure 17**). The conjugated double bonds, (i.e. pi bonds), are the key for a conductive polymer having metallic or semiconductor

properties. The conjugated p orbitals combine with each other to create an electronic band, within which region the electrons become highly mobile.

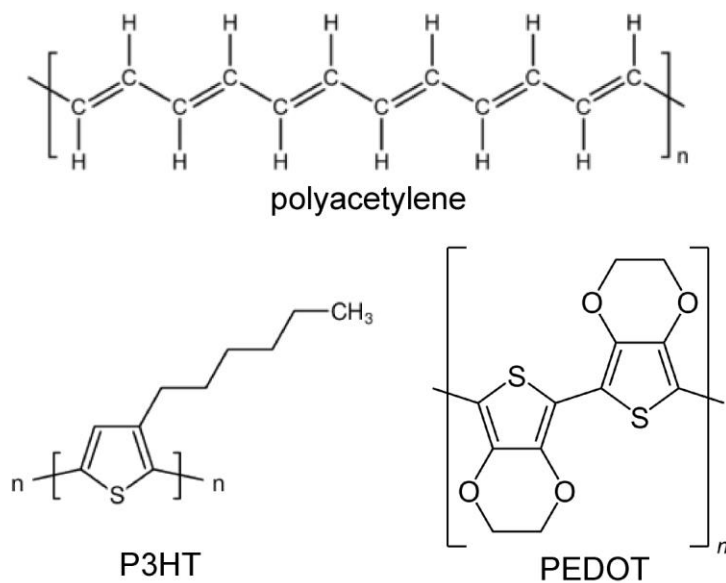


**Figure 17.** Chemical structure of three conductive polymer: polyacetylene, P3HT and PEDOT

Compared with metals and inorganic materials, the charge mobility for CPs is usually low. Therefore, it's difficult and unrealistic for CP to replace the role that traditional inorganic materials are playing, but CP will provide a perfect supplement in applications where inorganic material are not well suited. Conductive polymer possesses some extraordinary properties, such as flexibility, semitransparency, low-weight, small environmental impact, and simple fabrication processability. Today, great interest has grown in CPs and the materials are maturing with a large number of novel electronic devices being demonstrated such as bio-integrated device<sup>90</sup>, actuator<sup>91</sup>, supercapacitors<sup>92</sup>, organic light emitting diode<sup>93</sup>, organic photovoltaic <sup>94-96</sup> and sensors<sup>97-99</sup>. The conductive polymer usually employs thin film structure in devices, and can be easily printed or coated onto diverse types

of substrates, which gives it the possibility to be fabricated using roll-to-roll process to reduce cost (**Figure 18**).



**Figure 18** Slot-die coating of the silver back electrode onto PEN. The wet print that has an opaque green color is seen behind the slot-die coating head (top left). The dried and highly reflective silver back electrode is shown on the rewinding side (top right). The menisci during coating of the eight stripe module is also shown<sup>100</sup>.

### 2.1.2 Stretchable polymer semiconductors

The electronics that are able to survive under large deformation has received a great attention in recently years. The potential application includes bio-integrated device that is expected to replace the part of human being, as well as foldable electronic device in daily life such as smart phone and wearable electronics. The material for traditional electronic is usually based on Si and therefore rigid and brittle. In order to make these devices stretchable, special design to release the energy under deformation is necessary. A popular method is to connect the rigid device island with flexible connection and moves out of plane when under deformation. An example is given here in **Figure 19**, that the complementary metal-oxide-

semiconductor (CMOS) is connected with non-coplanar bridges<sup>101</sup>. Another popular configuration to achieve stretchability is employing out of plane buckling structure<sup>102–104</sup>, as shown in **Figure 20**. To achieve this, a soft elastomer substrate is pre-strained followed by printing a rigid semiconductor film. After the pre-strain is released, the thin film is forced to form the wrinkle or buckling structure. These types of methods are based on the well-developed traditional inorganic fabrication process and therefore are aligned with current manufacturing instrument. However, the cost and the requirement for the out of plane movement limit its application as well as performance. Therefore, it would be idea to develop semiconductor material that is intrinsic stretchable that can avoid the complex structure design.

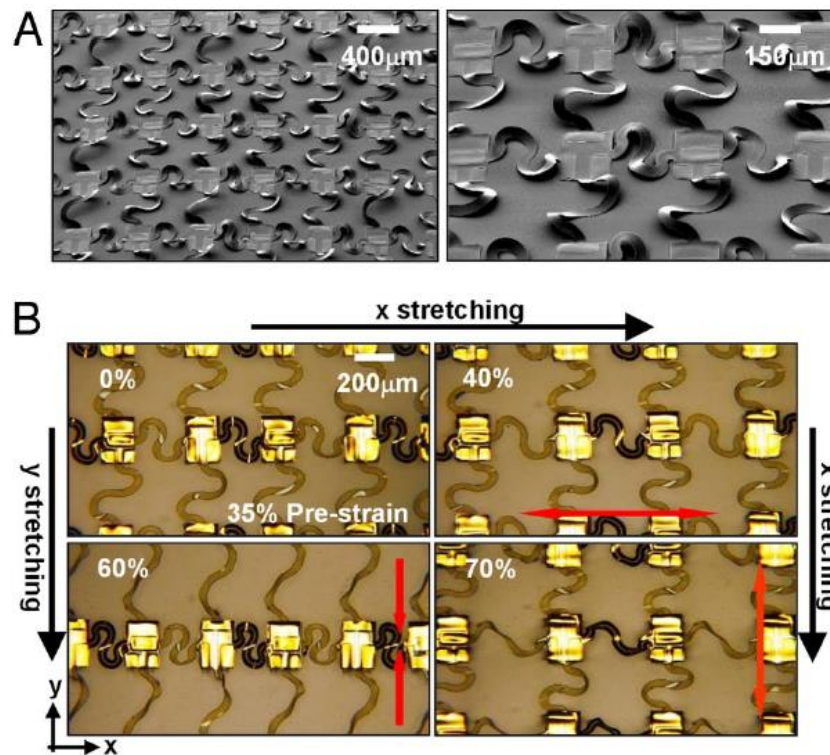


**Figure 19.** (A) SEM image of an array of stretchable CMOS inverters with noncoplanar bridges that have serpentine layouts (*Left*) and magnified view (*Right*). (B) Optical images of stretching tests in the  $x$  and  $y$  directions<sup>101</sup>.

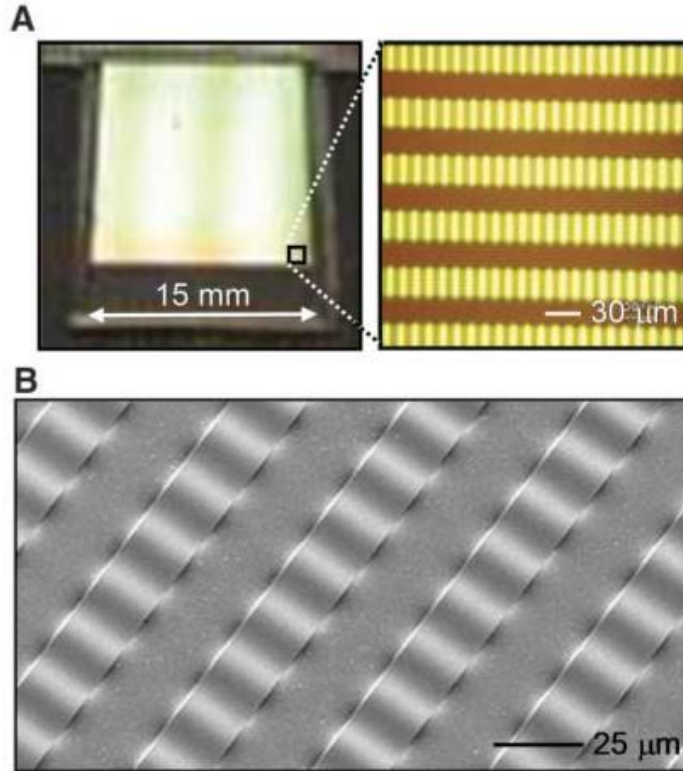


**Figure 20** (a) Optical images of a large-scale aligned array of wavy, single-crystal Si ribbons (widths = 20  $\mu\text{m}$ , spacings = 20  $\mu\text{m}$ , thicknesses = 100 nm) on PDMS. (b) Angled-view scanning electron micrograph of four wavy Si ribbons from the array shown in (a)<sup>104</sup>.

Conductive polymers (CPs) is an attractive material system for the potential intrinsic stretchable semiconductors given the ability to manipulate their plasticity, and the long history in the development of polymers with large reversible elasticity (i.e., elastomers). In addition, solution-processed polymer semiconductor has been reported with hole mobility over  $10 \text{ cm}^2/\text{Vs}^{105}$ . This value exceeds that of hydrogenated amorphous silicon with mobility on the order of  $1 \text{ cm}^2/\text{Vs}^{106}$ . However, a polymer with good stretchability usually possess a low charge carrier mobility, and vice versa. For example, Peng et al create a co-polymer semiconductor that is able to be stretched to 140%, but the field effect mobility was limited to around  $10^{-4} \text{ cm}^2/\text{Vs}^{107}$ . This is mainly because the necessities for high carrier mobility such as high degree of crystallinity and rigid chains are disadvantageous to the deformation of

polymer, **Figure 21**<sup>108,109</sup>. Recently, Son et al suggest in their work that generating localized aggregates instead increasing the crystallinity is an efficient method to improve the charge carrier transport<sup>110</sup>. This might provide another approach to increase the polymer's electrical property while maintaining the advantages in mechanical property.

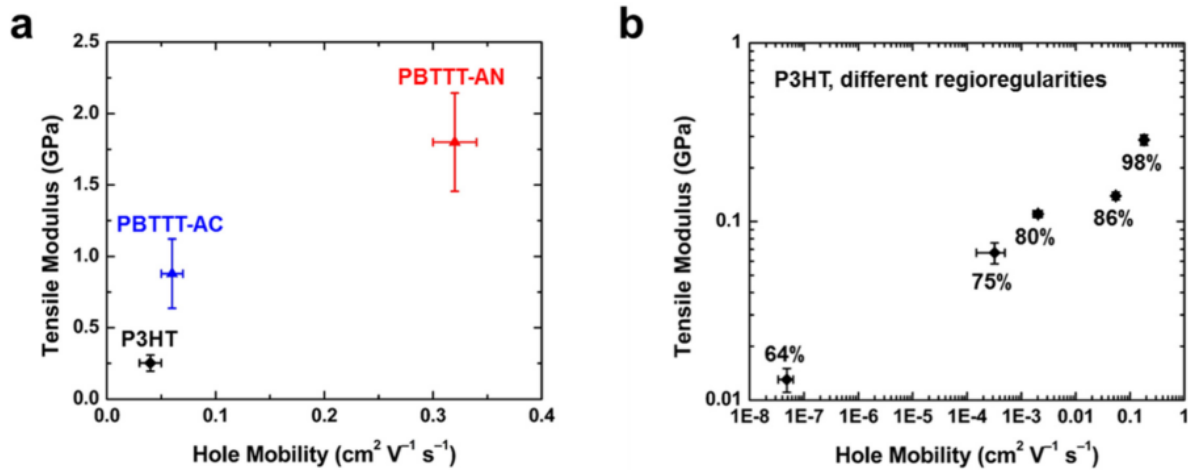


**Figure 21.** Tensile modulus vs. hole mobility for polythiophenes. (a) The tensile modulus and hole mobility of P3HT are lower than that of PBTTT. Both the stiffness and hole mobility increase when as cast PBTTT (PBTTT-AC) is annealed at 180°C (PBTTT-AN). The increase in tensile modulus and mobility of PBTTT compared with P3HT is attributed to improved order in PBTTT. Further ordering occurs in PBTTT when it is annealed, also leading to improved mobility and increased stiffness. (b) The tensile modulus and hole mobility of P3HT simultaneously increase with increasing regioregularity of the side-chains. The increase in both properties is likely due to the increased ability of regioregular P3HT to form ordered aggregates, which have improved charge transport properties, but is also stiff<sup>108,109</sup>.

One of the efficient way to improve the stretchability of the polymer semiconductor is by mixing with another elastomer component that possess better mechanical properties<sup>107,111–116</sup>, as shown in **Figure 22**<sup>112</sup>. The common elastomers are polydimethylsiloxane (PDMS)<sup>113</sup> and polystyrene-block-poly(ethylene-co-butylene)-block-polystyrene (SEBS)<sup>112,115</sup> due to being elastomers with good mechanical compliance and easy fabrication process. In this case, in order to maintain the electrical property of the blend film at the presence of the insulator

elastomer, a phase separation is necessary for the charge carrier mainly transporting through the functional semiconductor polymer. For devices like a transistor that the charge only transport within several nanometers in the semiconductor surface, a vertical segregation between two components is required, as shown in **Figure 22(b)**<sup>112</sup> and **Figure 23**<sup>117</sup>.

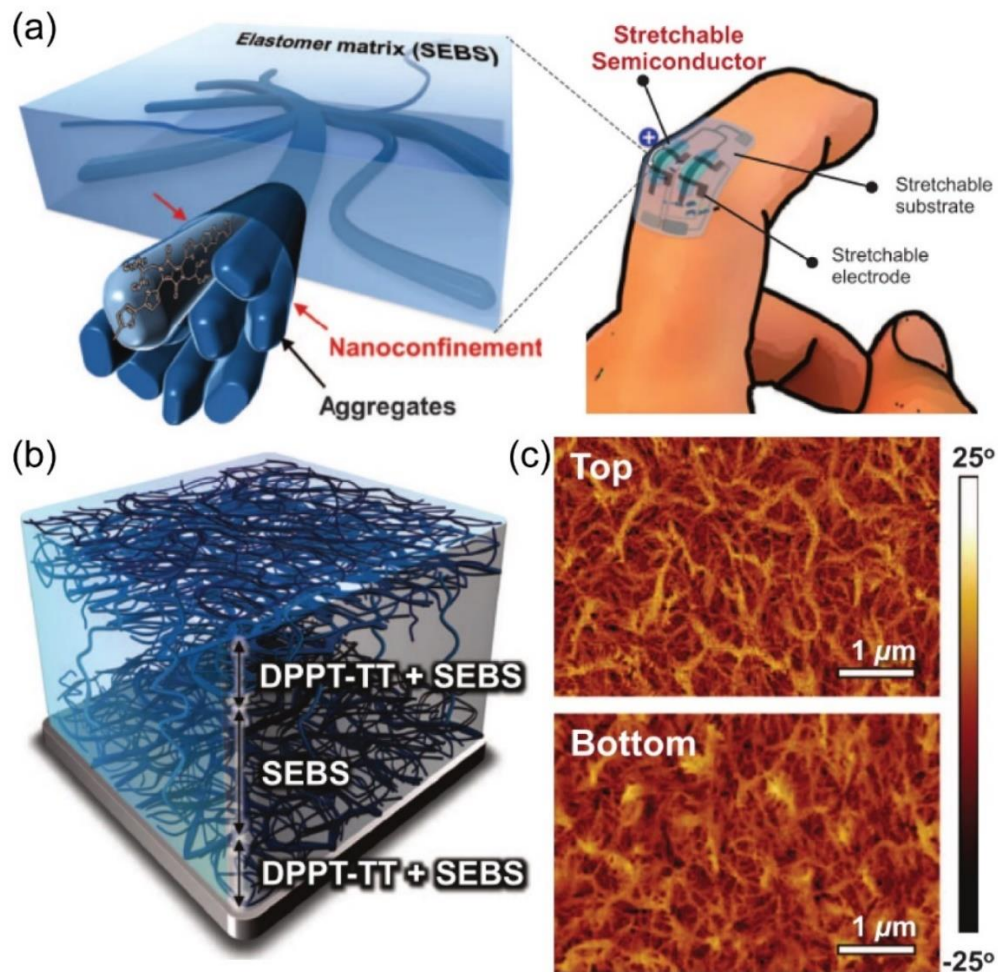


**Figure 22.** (a) A 3D schematic of the desired morphology composed of embedded nanoscale networks of DPP-TT polymer semiconductor to achieve high stretchability, which can be used to construct a highly stretchable and wearable TFT. (b) A 3D illustration of vertical segregation of blend film. (c) AFM phase images of the top and bottom interfaces of the blend film with 70 wt% SEBS.<sup>112</sup>

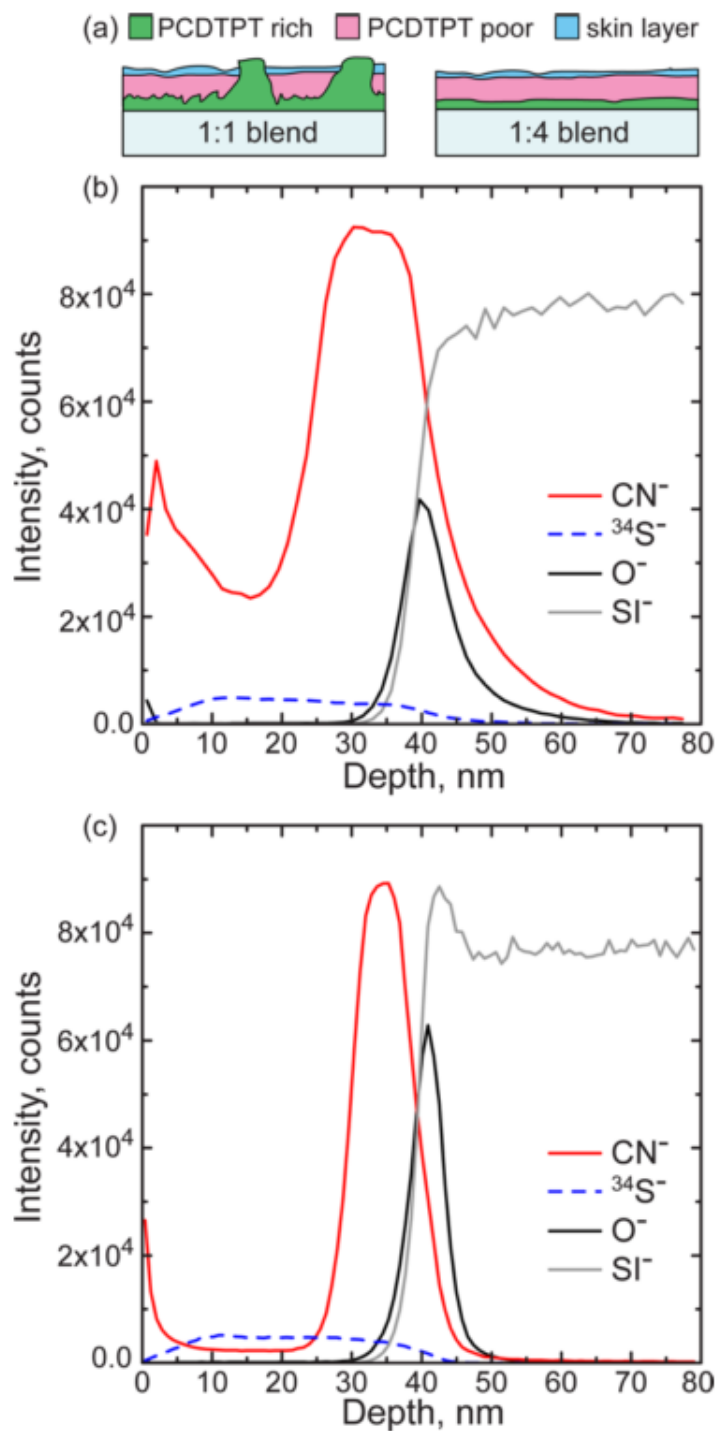


**Figure 23.** (a) Schematic of the segregation character of the 1:1 and 1:4 blend films. (b and c) TOF-SIMS results for vertical segregation of the (b) 1:1 and (c) 1:4 blend films on a Si substrate with its native oxide layer. The CN<sup>-</sup> ion is unique to the PCDTPT polymer<sup>117</sup>.

Adding plasticizer would be another way to improve the stretchability of CPs<sup>118–121</sup>. The plasticizer increases the free volume and therefore reduce the glass transition temperature ( $T_g$ ) of the polymer. For now, this method is mainly applied on the highly conductive polymer poly(3,4- ethylenedioxythiophene):polystyrene sulfonate (PEDOT:PSS). In fact, the plasticization of PEDOT:PSS shows improvement on not only the mechanical compliance under deformation, but also on the electrical conductivity, as shown in **Figure 24**. The increased electrical property is likely due to the improved crystallinity of PEDOT and the ordering of the PEDOT nanocrystals in the solid films<sup>122</sup>.

The stretchability of polymer is also shown to be related to their micro structure such as molecular weight, side chain structure, packing order, and so on<sup>123–126</sup>. Recently, Lu et al. showed that branched side chain and edge-on backbone contribute to better mechanical compliance as well as electrical performance under strain and obtained charge carrier mobility of 0.1 cm<sup>2</sup>/Vs under 100% strain<sup>125</sup>. The enhanced ductility mainly comes from the reduced order of alkyl chain packing order in the crystalline domain as well as the amorphous region with branched side chains compared with linear side chains. These molecular features results in a “softer” thin film with lower  $T_g$ <sup>127</sup>, **Figure 25**.

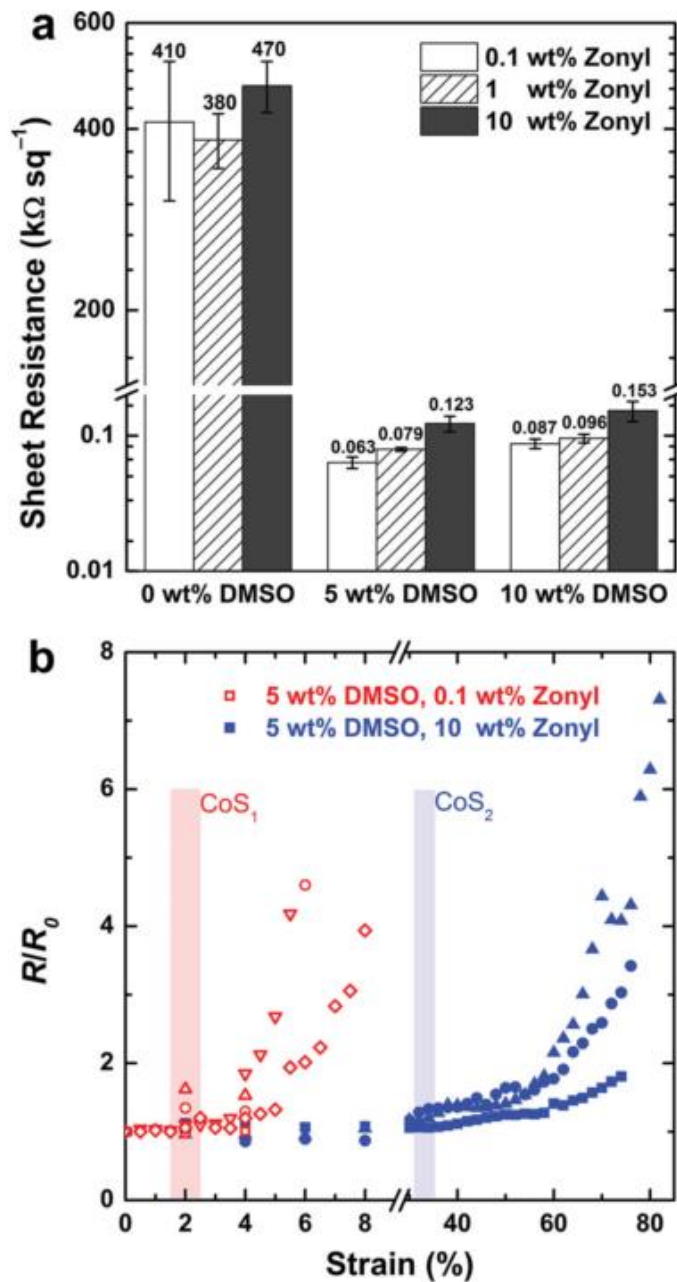


**Figure 24** (a) Sheet resistance as a function of both DMSO and Zonyl concentration in the ink. b) Plot of normalized resistance ( $R/R_0$ ) vs strain for PEDOT:PSS films spun from 0.1% and 10% Zonyl (with constant 5% DMSO) transferred onto PDMS substrates. Shaded areas represent the crack-onset strains (CoS) of the respective films. The widths of the shaded areas are two times the standard deviations for the measurements of crack-onset strain. The different marker symbols (squares, triangles, etc.) refer to different films coated from the same solution<sup>118</sup>.

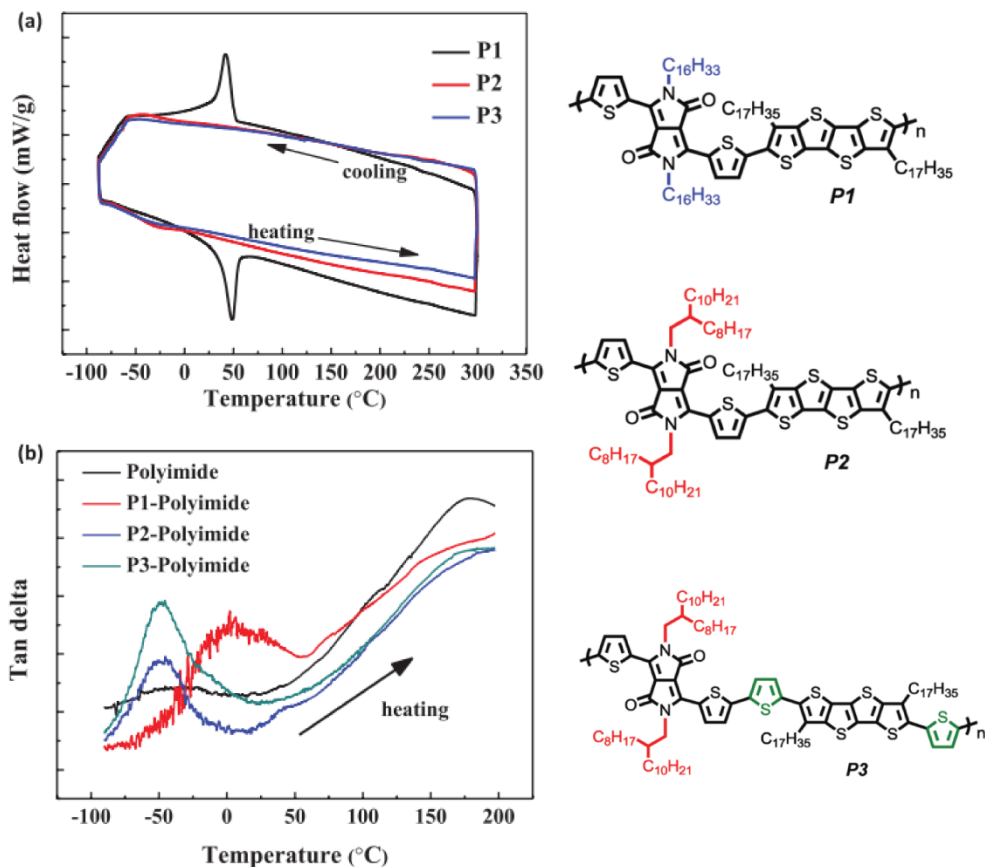


**Figure 25** (a) DSC thermogram of the studied polymers at heating/cooling rate of  $10\text{ }^{\circ}\text{C min}^{-1}$ , (b) DMA curves of samples at frequency of 1 Hz and heating rate of  $10\text{ }^{\circ}\text{C min}^{-1}$ . The structures of studied polymers are shown on the right.

### 2.1.3 Characterization methods

A variety of characterization methods have been developed to better understand conductive polymer of material properties including mechanical properties, electrical properties, optical properties, morphology, etc. Here, we introduce some common characterization methods used to analyze the polymer thin films.

#### *Ultraviolet visible spectroscopy*

Ultraviolet visible spectroscopy is a measurement of attenuation of a beam of light after passing through a sample or reflected from the surface of a sample. The sample can be either

solid or solution. Due to different number and arrangement of sigma, pi bonding and nonbonding electrons within the conductive polymer resulting in different electron transition energy in the molecule, the conductive polymer sample absorbs light with different wavelength and shows varied absorption spectrum. **Figure 26** shows absorption spectrum for two different polymers P3HT and PCDTPT. From the figure we can see that P3HT mainly absorbs light within the wavelength range between 400 nm and 650 nm and the absorption reach the maximum at 550 nm, while PCDTPT has a different absorption range between 700 nm and 950 nm with the maximum absorption wavelength around 900 nm. Therefore, the UV-vis technology allows us to identify different types of CPs by comparing measured absorption spectra. Besides, for some conductive polymers, one can even tell the relative crystallinity level of a solid sample through some feature in the absorption spectrum graph. For example, for P3HT film, we notice there exist a small shoulder at the right of the maximum peak. And in a normalized absorption spectrum, a higher shoulder usually indicates a higher crystallinity level of the sample<sup>128</sup>.

**Figure 27** shows the UV-vis setup in our lab. We use a commercial power source to generate light and Ocean Optics Jazz spectrometer as a receiver to analyze the absorption or transmission of the sample. Between the light source and receiver, there exists 4 other parts: light filter, polarizer, sample holder and reference holder. The light filter is used to optimize the light quality as well as reduce the light power to a safe range for the receiver. The polarizer can generate a beam of polarized light, which is used to study the polymer chain orientation of anisotropic polymer films. This is done by measuring the absorption anisotropy of the film under linear polarized light with varied orientations. The sample holder holds the polymer sample together with substrate and reference holder holds the substrate only.

Usually the absorption measurement is done with the polymer film on a transparent glass substrate. Although transparent, the glass does absorb a small amount of light that may interfere the absorption result and it's important to deduct this part of light absorption during the measurement. To achieve this, a substrate with the same processing (i.e. cleaning process, surface treatment) as polymer substrate is held using reference holder. Every time before the measurement, take the reference from the clean substrate to eliminate the effect of substrate.

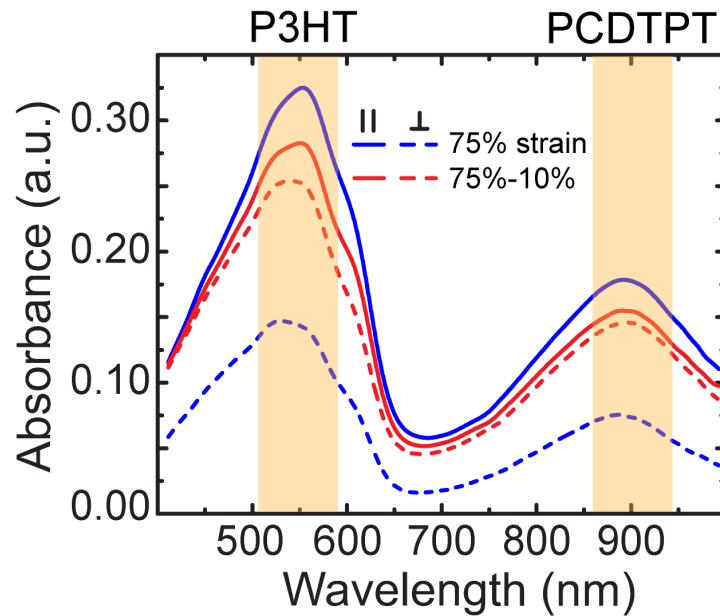


**Figure 26.** Absorbance of the PCDTPT:P3HT blend film at 75% strain and film strained to 75% and then lowered to 10% under polarized light parallel (//) and perpendicular ( $\perp$ ) to the strain direction.

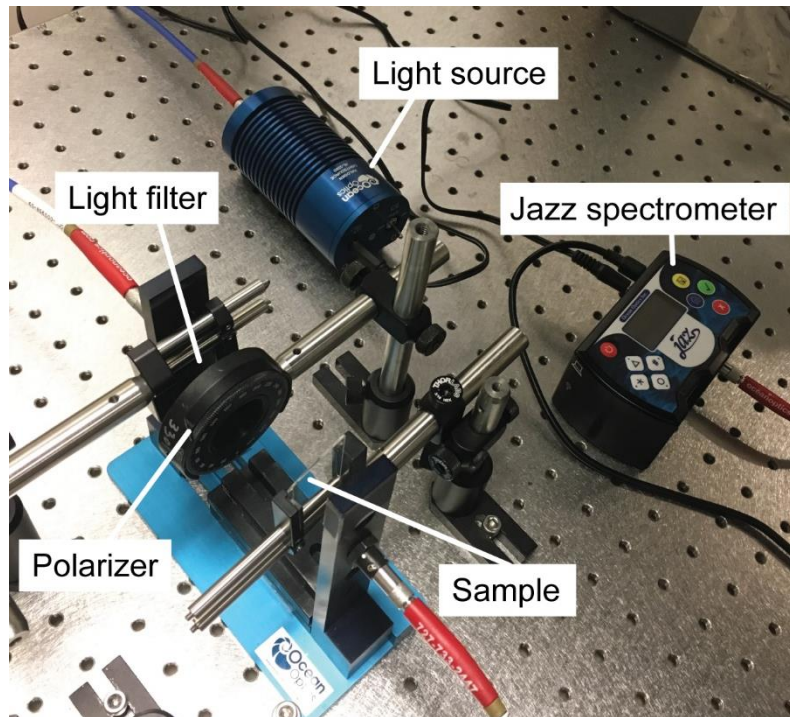


**Figure 27.** UV-vis setup in O'Connor research laboratory, NC State University

### *Atomic Force Microscope*

Atomic Force Microscope (AFM) is one type of Scanning Probe Microscope (SPM), which is designed for characterization the sample's surface morphology and structure by physically scanning over the specimen with a probe. Different than other SPM techniques, AFM works by monitoring and regulating the atomic reaction between sample and probe tip. **Figure 28**<sup>129</sup> describes how AFM works briefly. When tip approaches the sample, the cantilever is deflected by the interactive force from sample surface. This cantilever deflection is monitored by a laser beam deflection system, in which a beam of laser is shot onto the back of cantilever and reflected to a position sensitive detector. The interactive force can be calculated from the Hooke's law,

$$N = -kz \tag{22}$$

in which  $N$  is the interactive force,  $k$  is the cantilever stiffness and  $z$  is the deflection of cantilever tip. By maintaining a stable interactive force (by controlling setpoint value), the probe will move up and down while scanning over the sample surface and the image of sample surface can be tracked by laser position feedback loop. In our case, we use MFP-3D model AFM from Asylum Research, **Figure 29**.

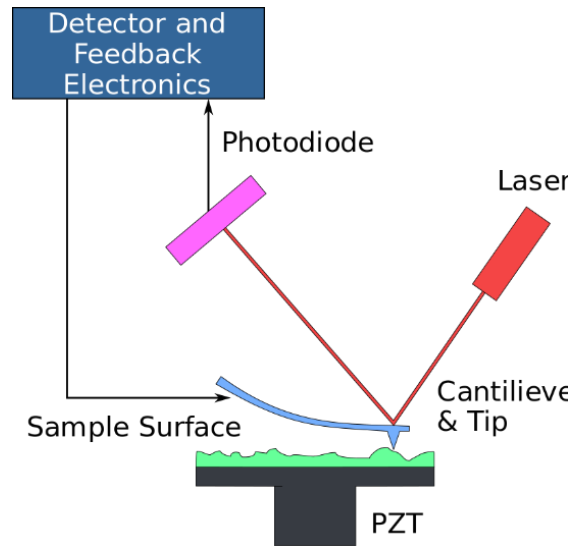


**Figure 28.** Schematic of how an AFM works<sup>129</sup>.



**Figure 29.** MFP-3D model AFM from Asylum Research.

### *Electrical properties*

Charge carrier mobility ( $\mu$ ) is usually a primary figure of merit used to describe the electrical behavior of organic semiconductors since it characterizes how fast the charge carriers, holes or electrons, move through the material. It determines the limiting device operation speed performance and therefore is an important parameter for characterization.

Charge carrier mobility for the organic semiconductor material can be extracted from thin film transistor (TFT) characteristic. A schematic for TFT device structure is shown in **Figure 30**<sup>130</sup>. It is usually composed of five components: substrate, gate electrode, dielectric layer, active layer, source and drain electrode. And depending on the electrode position, there are bottom gate-bottom contact, top gate-bottom contact, bottom gate-top contact and top gate-top contact configurations. In this thesis, the transistors are fabricated into bottom gate-bottom contact configuration unless otherwise mentioned due to the easy fabrication processing and good quality. **Figure 31** shows the source and drain electrode made of 40 nm gold/5 nm titanium for one transistor testbed. It's patterned through standard photolithography process and fabricated by thermal evaporation. The organic semiconductor, which serves as active layer in the channel between source and drain electrodes, is deposited or transferred onto the testbed surface for electrical characterization.

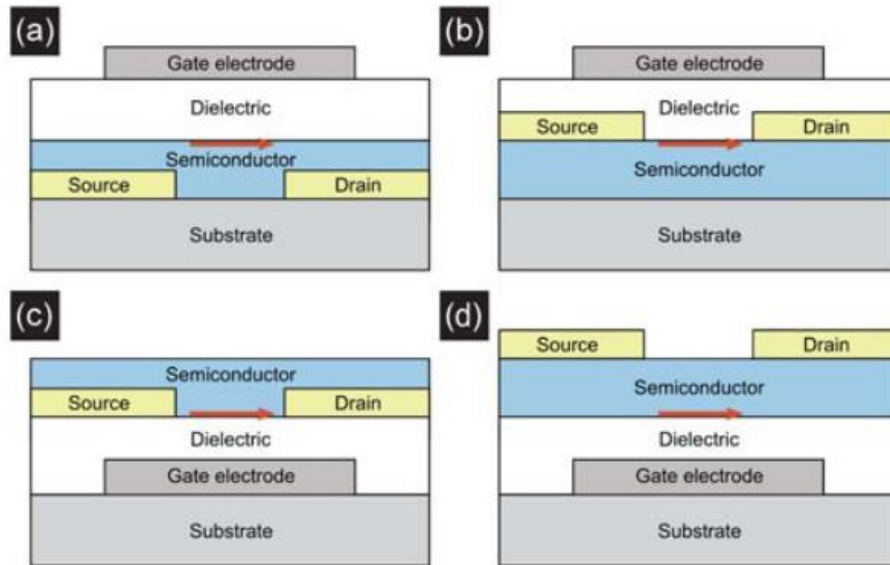


**Figure 30** Schematic representations of field-effect transistor architectures, (a) top-gate bottom-contact, (b) top-gate top-contact, (c) bottom-gate bottom-contact, and (d) bottom-gate top-contact. The arrow shows the charge conduction interface<sup>130</sup>.

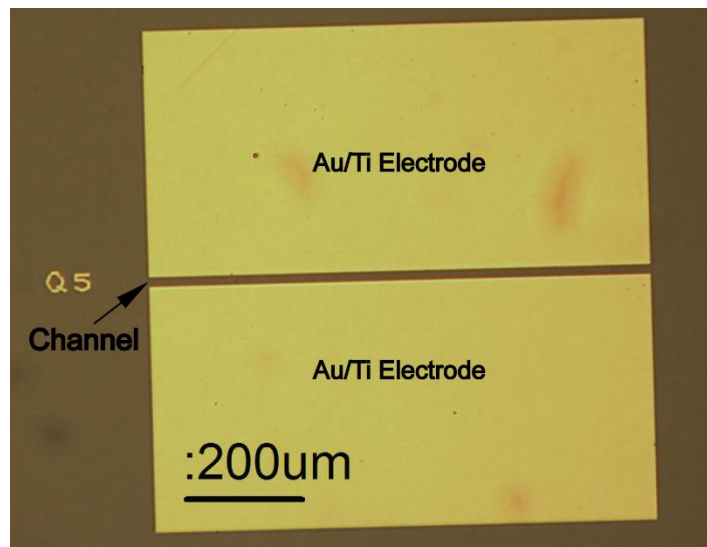


**Figure 31.** Microscope image of source and drain electrodes made of 40 nm gold/5 nm titanium for one transistor testbed.

There are two voltages applied for an effective transistor device - gate voltage ( $V_G$ ), voltage applied on the gate electrode and source-drain voltage ( $V_{DS}$ ), voltage applied between source and drain electrodes. Our focus is on p-type transistors. When  $V_G = 0$  V

(ideally, but positive  $V_G$  is needed in some cases), the conductance of the channel is very low due to the very small amount of charge carrier in the material and the device is “off”. While when  $V_G < 0$  V for a p-type or  $V_G < 0$  V for n-type organic semiconductor, charge carrier starts to accumulate at the semiconductor/dielectric interface and moves in the presence of electric field induced by  $V_{DS}$ . And at this point, the device is “on” and there is significant current,  $I_{ds}$ , between source and drain electrodes. However, sometimes the point where gate voltage first introduces in mobile charge carrier doesn’t always correspond to  $V_G = 0$  due to doping, energy level mismatch, traps, etc. So, for convenience, threshold voltage ( $V_{th}$ ) is created to define the point the transistor has significant charge accumulation. **Figure 32a** describes a common  $I_{DS}$ - $V_{DS}$  curve at different  $V_G$ . When  $V_G > V_{th}$  and  $V_G$  is held stable,  $I_{DS}$  initially goes up linearly with  $V_{DS}$ , and this region is called “linear regime”. This regime continues to exist until  $V_{DS}$  reaches  $V_G - V_{th}$ , i.e.  $V_{DS} = V_G - V_{th}$ , where “saturation regime” start to dominate. At this point, the conduction band is “pinched off” and further increase  $V_{DS}$  will not increase  $I_{DS}$ . Another way for TFT characterization is to hold  $V_{DS}$  stable, and sweep  $V_G$ , as shown in **Figure 32b**. In this case, after the device is switched on (passing subthreshold region), the device is operated under saturation regime first, and then gradually transferred to linear regime. The saturated mobility  $\mu_{sat}$  can then be extracted from the slope of  $I_{DS}^{1/2}$  vs  $V_G$  curve in the saturation regime using the following equation,

$$\mu = \frac{2L_c}{WC_{ox}} \frac{I}{(V_G - V_{th})^2}, \quad (23)$$

where  $L_c$  is the channel length,  $W$  is the channel width,  $C_{ox}$  is the capacitance of the dielectric layer per unit area. All the mobility values in the following text would have been calculated using the same Eqn. 23.

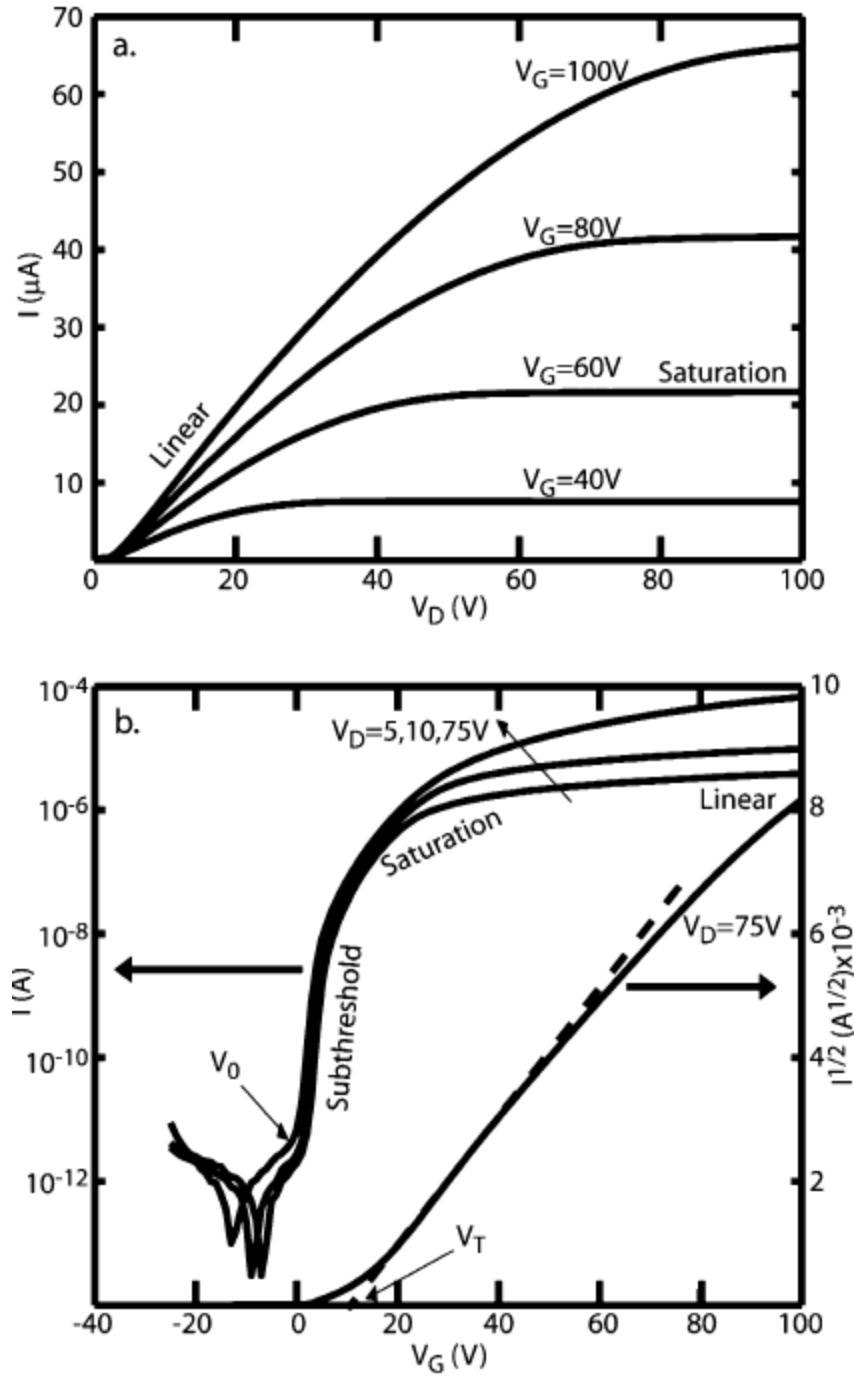


**Figure 32.** (a) Example  $I_D$ - $V_D$  curves for a PTCDI-C8 TFT for various values of  $V_G$ . (b) Example  $I_D$ - $V_G$  curves plotted on semi logarithmic axes for the same device for various values of  $V_D$ . The  $I^{1/2}$  vs  $V_G$  curve for  $V_D = 75\text{V}$  is shown on the righthand axis<sup>131</sup>.

## 2.2 Stretchable Film Approach

Blending technique has been proven an efficient method to improve polymers' mechanical properties such as ductility, strength and fracture toughness. In the field of polymer semiconductor, blending a functional polymer semiconductor with another elastomer also shows advantages for improving ductility<sup>115,116,132</sup>. However, although the electrical performance after blending with elastomer can be maintained by phase separation, it still shows deduction after the blend film is being strained because of the formation of cracks<sup>115,132</sup>. In fact, the natural property of polymer semiconductors to plastically deform under strain is not overwhelmed by adding elastomer and the blend film still undergoes plastic deformation instead of elastic deformation under large strain. Although it is tempting to have a polymer that can be both elastically deformed and possessing good electrical property, the elastomer's natural behavior of low crystallinity doesn't cooperate well with the necessities for high electrical property. In comparison, it's easier and more realistic to achieve stretchability through plasticity, or plastic deformation. Therefore, instead of blending with an elastomer to improve the stretchability, adding a ductile polymer semiconductor might be more advantageous in terms of higher electrical performance.

## 2.3 Plastic Deformation of Polymer Blends as a Means to Achieve Stretchable Organic Transistors

### 2.3.1 Introduction and motivation

(From T. Sun, J. I. Scott, M. Wang, R. J. Kline, G. C. Bazan, B. T. O'Connor, "Plastic Deformation of Polymer Blends as a Means to Achieve Stretchable Organic Transistors", *Adv. Electron. Mater.* 3, 2017)

Electronics that are able to maintain their function during large deformation provide opportunities for integration into a range of transformative technologies, from soft-robotics to bio-integrated devices<sup>90,133</sup>. This vision has resulted in a growing number of demonstrations of stretchable electronic devices including photovoltaics<sup>96,134</sup>, light-emitting devices<sup>135,136</sup>, sensors<sup>133,137</sup>, and transistors<sup>116,138,139</sup>. To impart the ability for devices to reversibly stretch, approaches include the use of geometric structures that minimize strain on the active components<sup>90,96,140</sup> and employing intrinsically stretchable materials<sup>107,138,141</sup>. The development of intrinsically stretchable devices is particularly attractive due the ability to achieve larger device densities, greater strain limits, and seamless integration into stretchable applications. In order to achieve an intrinsically stretchable device, all the layers composing the device need to be stretchable<sup>138,139</sup>. A particular challenge in realizing these devices is the development of intrinsically stretchable semiconductor layers<sup>138</sup>. In the search of stretchable semiconductors, polymers are an attractive material system to explore given the ability to manipulate their plasticity, and the long history in the development of polymers with large reversible elasticity (i.e., elastomers)<sup>142</sup>. Examples of intrinsically stretchable polymer semiconductors include the demonstration of a tri-block co-polymer based on poly(3-hexylthiophene) (P3HT) and poly(methyl methacrylate) to form a thermoplastic elastomer that was able to stretch by 140%<sup>107</sup>. However, the field effect mobility was limited to  $\approx 10^{-4}$

$\text{cm}^{-2} \text{V}^{-1} \text{s}^{-1}$ . More recently, a cross-linked diketopyrrolopyrrole (DPP) polymer was synthesized with a consistent field effect mobility above  $0.4 \text{ cm}^2 \text{V}^{-1} \text{s}^{-1}$  over a strain range of 20%<sup>143</sup>. Another approach has been to form a fibril network of polymer semiconductor material embedded into an elastomer host<sup>113,115,132</sup>. However, this approach consists of a sparse network of semiconductor material that may limit performance, and can still result in fibril fracture at large strain. An alternative approach is to modify the plasticity of the polymer of interest. There have been a number of reports on changing the plasticity of electrically conducting polymer films through modification of the molecular structure<sup>144,145</sup>, morphology<sup>145,146</sup>, and through the use of additives<sup>117–119,147,148</sup>. While these approaches have shown a change in plasticity, there have been limited reports on repeated stretchability of the films. Recently, the conductive polymer poly(3,4-ethylenedioxythiophene):polystyrene sulfonate (PEDOT:PSS) was shown to be highly deformable when incorporating the plasticizer Triton X-100<sup>119</sup>, which was attributed to lowering the glass transition temperature ( $T_g$ ) of the film. However, we are unaware of demonstrations of plasticizers used in polymer semiconductors to achieve stretchable films<sup>138</sup>. Here, we introduce a novel approach to achieve intrinsically stretchable polymer semiconductors. We employ a polymer semiconductor blend film that is shown to plastically deform in tension and compression when on an elastomer substrate allowing for a highly deformable organic semiconductor with high charge mobility when applied in an organic thin film transistor (OTFT). Previously, blending polymer semiconductors has been shown to modify the mechanical response of the film while maintaining charge transport behavior<sup>117,149</sup>. While the ductility of films was shown to increase, the ability to cyclically stretch while maintaining electrical properties has not been shown. For a semiconductor that will be used in stretchable devices, not only is it

important to be able to survive large tensile strain, but also to function after the reduction of the applied strain. Here, we achieve this cyclic strain capability by blending a high-performance polymer poly[4-(4,4-dihexadecyl-4H-cyclopenta[1,2-b:5,4-b,]dithiophen-2-yl)-alt-[1,2,5]thiadiazolo[3,4-c]pyridine] (PCDTPT)<sup>150</sup> with a highly ductile polymer P3HT. PCDTPT has been shown to be a high-performance polymer semiconductor when applied in an OTFT, but is relatively brittle and cracks at a few percent strain<sup>117</sup>. Blending P3HT with PCDTPT significantly increases the ductility of the film over neat PCDTPT, while also maintaining the charge mobility associated with the higher performing PCDTPT when applied in an OTFT. This behavior was attributed to vertical segregation of the PCDTPT toward the gate dielectric interface, while also having significant intermixing of both polymers throughout the films thickness, as illustrated in **Figure 33**<sup>117</sup>. In this work, we explore the ability of P3HT:PCDTPT blend films to function well under large cyclic strain. The morphology and charge transport is characterized for the film strained by 75% and released back to 10% strain, relative to its original length under a specified number of cycles. We show that the films can be cyclically strained up to 100 times while showing stable charge transport behavior owing primarily to the reversible plastic deformation behavior of the blend film with highly stable local polymer order. This represents a novel approach to achieve intrinsically stretchable semiconductor consisting solely of semiconductor materials. Below we first discuss the morphology of the blend film under cyclic strain followed by charge transport characterization.

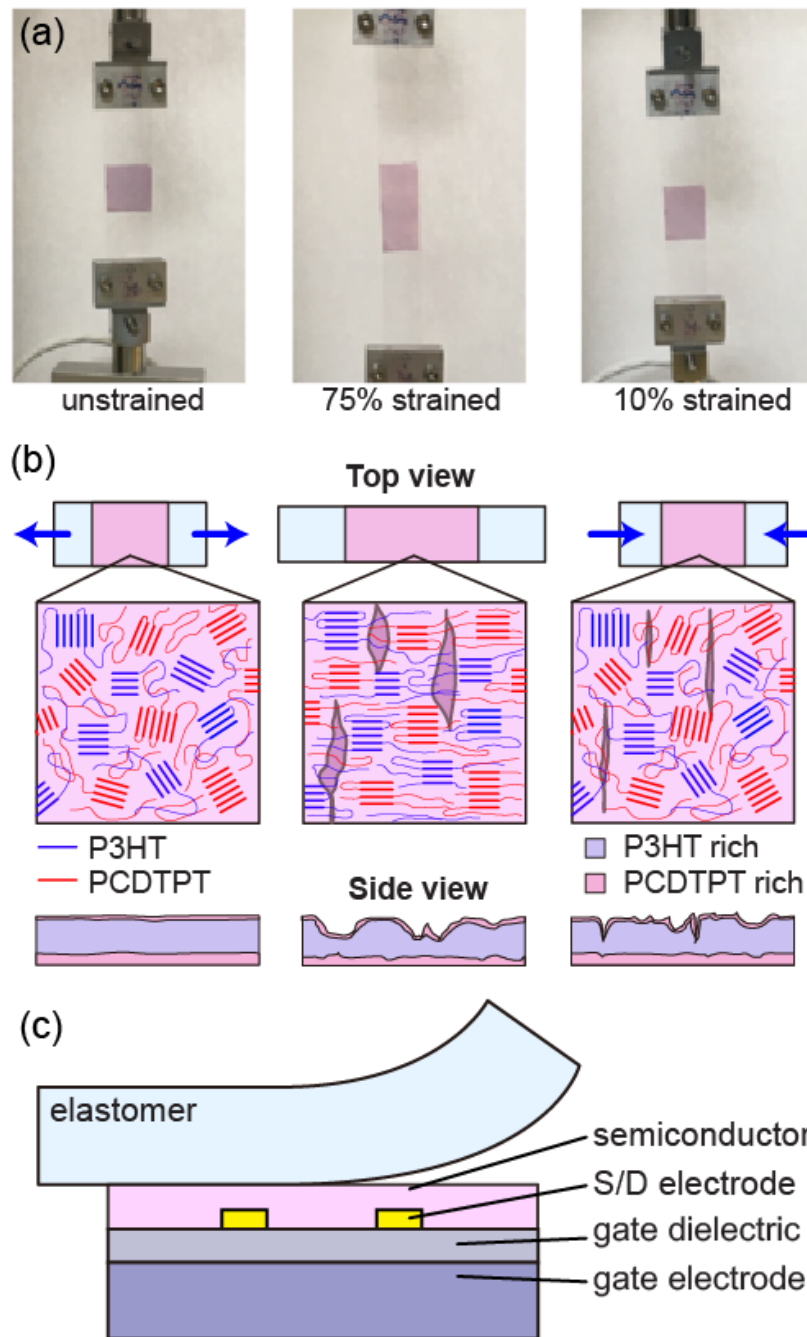


**Figure 33.** (a) Photos of an unstrained film, 75% strained film and strain-released film at 10% strain while on PDMS. (b) Illustration of the change in film morphology during the cyclic strain process from a top view and side view. At large tensile strain, the illustration includes alignment of both polymers and partial tearing features. When the strain is reduced the polymer alignment reduces and tearing features narrow. The side view includes an illustration of the vertical segregation of the polymers found in the blend film. (c) An illustration of transfer printing the polymer semiconductor film from the elastomer stamp to an OTFT test bed.

### 2.3.2 Results and discussion

Films were first spun cast onto octyltrichlorosilane (OTS) treated silicon and then transfer printed to a polydimethylsiloxane (PDMS) elastomer substrate. The film-PDMS stack was then elongated in tension to a specified strain. For cyclic strain, the film-PDMS stack was strained to 75% and then strain was released back to 10% relative to its unstrained state, and repeated for a specified number of cycles. After the strain process was complete, the films were either characterized while on the PDMS substrate or transfer printed onto a secondary substrate for further characterization. Images of a film being strained are shown in **Figure 33** along with a schematic of the cyclic strain process, and the lamination onto a transistor test bed for charge transport characterization. Our previous report investigating PCDTPT:P3HT blend films showed that the blend ratio had a significant impact on the segregation characteristics and ductility of the film<sup>117</sup>. A 1:1 PCDTPT:P3HT blend ratio by weight had a charge mobility similar to the neat PCDTPT film, but in addition to vertical segregation, large lateral segregation of the PCDTPT was observed that limited the crack onset strain to under 50%. When reducing the ratio to 1:4 the lateral segregation was suppressed and ductility increased but there was a decrease in charge mobility. Here we focus on a polymer ratio of 4:6 by weight, approaching the 1:1 ratio to maximize charge mobility but without gross lateral segregation of the PCDTPT, resulting in highly ductile films, as we show below. An optimization of the blend film was not performed, and further optimization of the polymer ratio and processing conditions may lead to further performance gains.

#### *Film morphology*

The change in morphology under large cyclic strain is first characterized by measuring the films with UV–visible spectroscopy under linearly polarized light while the film was on a

PDMS substrate. P3HT and PCDTPT absorb light over different spectral ranges of  $\approx 400\text{--}620$  nm for P3HT and  $650\text{--}1100$  nm for PCDTPT, as shown in **Figure 34(a)**. This allows for unique optical characterization of each polymer. When large strains are applied to the films, the absorbance of linear polarized light parallel to the strain direction increases relative to the absorbance of polarized light perpendicular to the strain direction over both the spectral range associated with P3HT and the range associated with PCDTPT. This dichroism is associated with the alignment of the polymer backbones in the direction of strain<sup>151</sup>. To quantify the alignment of the polymer in the strained film, we calculated the dichroic ratio of the blend films at a wavelength of 550 nm to track P3HT, and at 900 nm to track PCDTPT, provided in **Figure 34(c)**. We find that the dichroic ratio increases with applied strain and behaves in a similar manner with strain at both wavelengths. At a strain of 75%, the dichroic ratios of 2.4 and 2.3 were found at 550 and 900 nm, respectively. When the 75% strained film was reduced to lower strains, the dichroic ratio drops following the same trend as found in the tensile strain direction. The film strained by 75% and then reduced to 10% strain has a dichroic ratio of  $\approx 1.1$  at both 550 and 900 nm. To determine if this morphology change is consistent over many strain cycles, the films were repeatedly strained to 75% and then back to 10% for up to 100 cycles with the dichroic ratio measured at these strain limits. As shown in **Figure 34(d)**, the dichroic ratio at 550 and 900 nm consistently repeats during the cyclic strain process. These results suggest that when the large tensile strain applied to the film is released, the polymer in the film plastically deforms back toward an in-plane isotropic distribution. It is important to note that the absorbance measures the average in-plane orientation of the polymers such that an isotropic backbone distribution and a biaxial orientation distribution will both have a dichroic ratio of 1. It has previously been shown that

a P3HT film uniaxially strained in tension by 100% and then strained again in tension in the transverse direction by 100% results in films with a broad crystalline orientation distribution<sup>152</sup>. It is expected that a similar morphological change will occur here and that when the strain is lowered the polymer backbones will go back toward an in-plane isotropic distribution. To verify that the films are plastically deformed, the blend film was strained to 75%, transfer printed to a silicon substrate and then floated off in water. Here, the film is able to retract without constraint providing an indication of elastic recovery. The film strained by 75% and then floated in water was found to contract by approximately 8% which is attributed to elastic strain recovery, demonstrating that the films are plastically deformed.

The absorbance can also provide information on the local order of the polymer in the film<sup>153</sup>. To compare how the absorbance features change over many strain cycles, we plot the normalized absorbance for films strained by 75% the first time and after 100 cycles, and films strain released back to 10% the first time and after 100 cycles in **Figure 34(b)**. We find that the absorbance features are remarkably similar before and after the cyclic strain process. The vibrionic features in the P3HT remain almost identical, indicative of similar aggregate order<sup>153</sup>. This is consistent with previous work on strain oriented neat P3HT films where it has been shown that the P3HT orients in the direction of strain without a significant difference in aggregate percentage or aggregate quality<sup>128</sup>. The PCDTPT absorbance is also very similar after the first strain cycle and 100th cycle indicative of similar PCDTPT aggregate order.

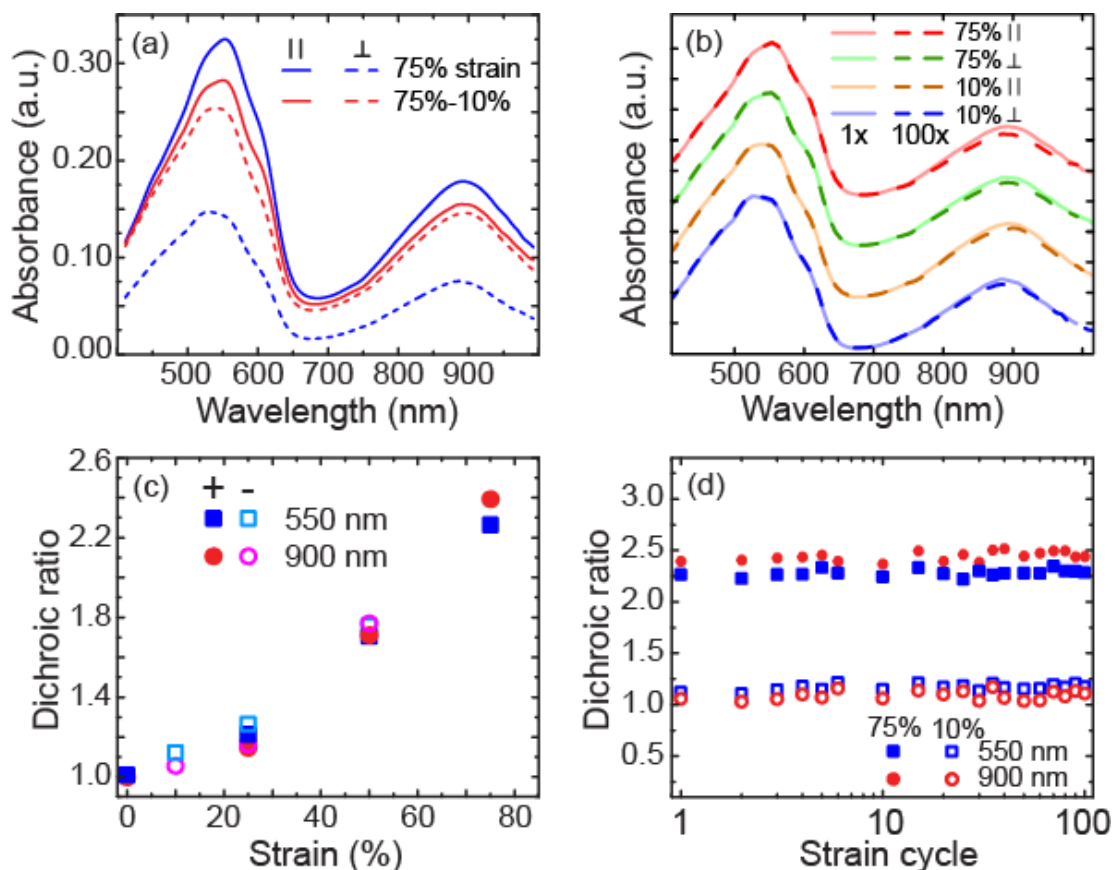


**Figure 34.** (a) Absorbance of the PCDTPT:P3HT blend film at 75% strain and film strained to 75% and then lowered to 10% under polarized light parallel (||) and perpendicular (⊥) to the strain direction. (b) The normalized absorbance of the blend film at 75% strain and at 10% strain, comparing the first strain cycle (1x) to 100 cycles (100x). The measured absorbance at a specific strain state and polarized light orientation are normalized and offset for clarity. The absorbance at a specified strain state and light polarization during the first strain cycle and after 100 cycles are plotted together to compare absorbance features. (c) The dichroic ratio of the blend film under tensile strain (+) and reduction of the applied strain (-) during the first strain cycle. The dichroic ratio is taken at 550 nm and at 900 nm to capture the P3HT and PCDTPT, respectively. (d) The dichroic ratio of the blend film at 75% strain and 10% strain with increasing number of strain cycles.

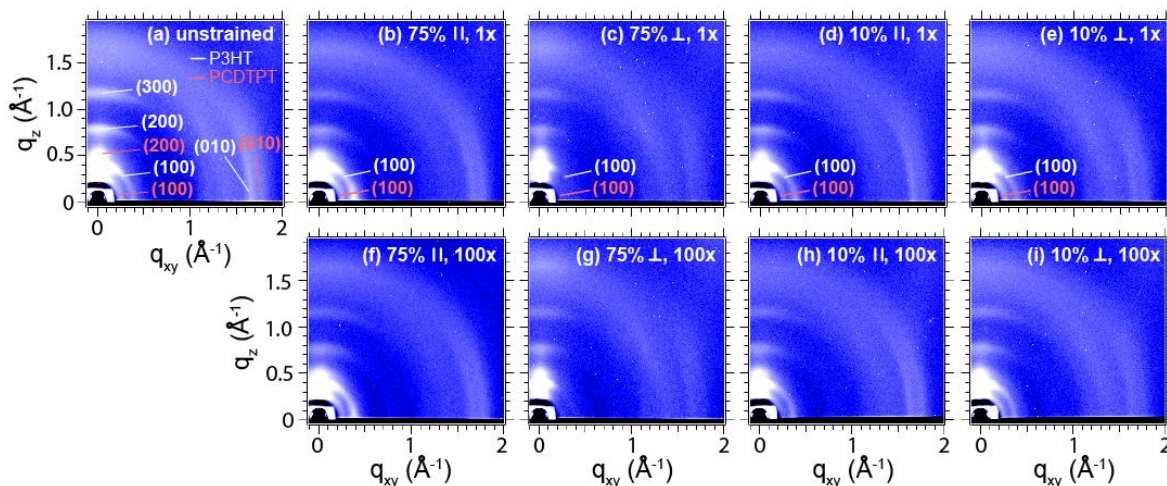


**Figure 35.** Two-dimensional grazing incidence X-ray diffraction images of (a) an unstrained film, and strained films during the (b-e) first strain cycle and after (f-i) 100 strain cycles held at 75% strain and 10% strain as specified. The X-ray beam is incident parallel (II) or perpendicular ( $\perp$ ) to the strain direction as labeled.

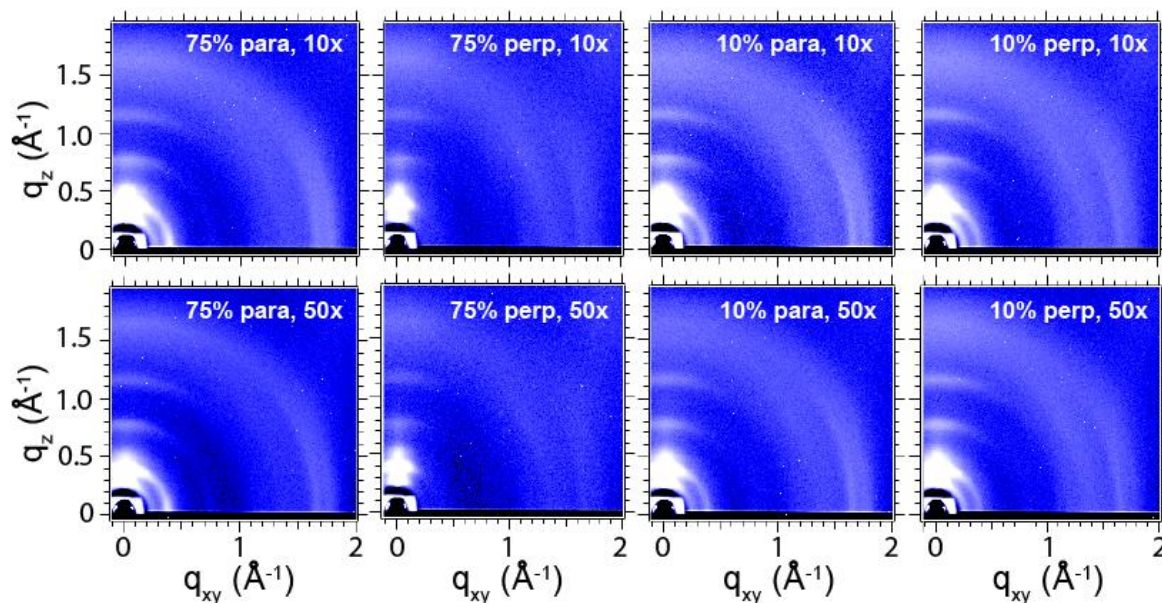


**Figure 36.** Two-dimensional grazing incidence X-ray diffraction images of films strained to 75% and 10% after 10 and 50 strain cycles. The X-ray beam is incident parallel (para) or perpendicular (perp) to the strain direction as labeled.

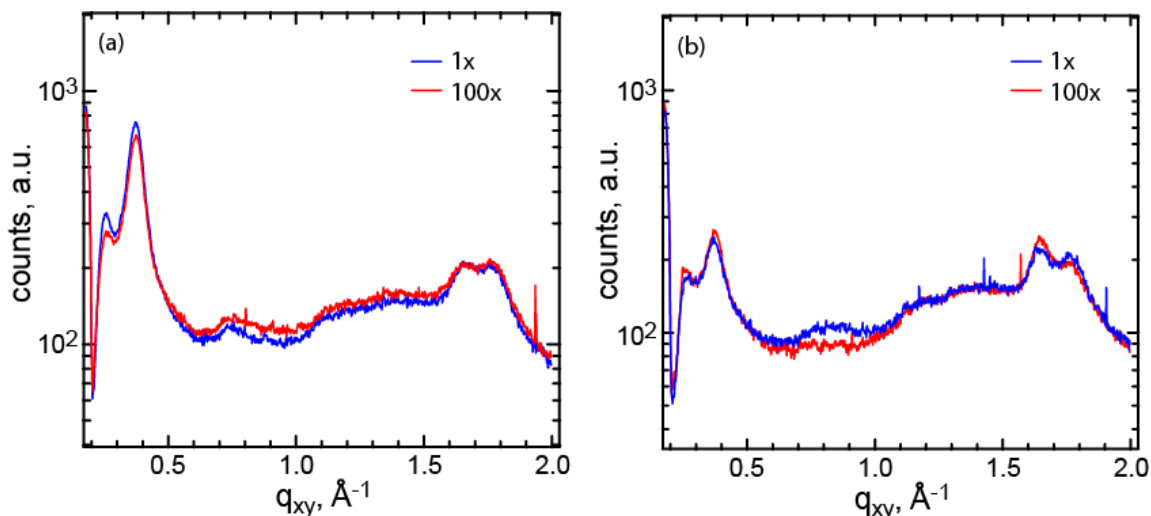


**Figure 37.** In-plane line scans of the 2D GIXD images with X-ray parallel to the strain direction, taken for films at the (a) 75% strain limit and (b) 10% strain limit. The reported data is for the films in its 1<sup>st</sup> strain cycle (1x) and 100<sup>th</sup> strain cycle (100x).

The change in morphology under cyclic strain was also characterized by grazing incidence X-ray diffraction (GIXD). 2D GIXD images were taken on films under various number of strain cycles at both 75% strain and at 10% strain, with images shown in **Figure 35** and **Figure 36**. Previously it has been shown that P3HT and PCDTPT crystallites are present in the blend film and that due to the packing differences of the crystals, their diffraction peaks in the  $\pi$ -stacking and alkyl-stacking directions are separated in reciprocal space<sup>117</sup>. We observe that as the film was strained the diffraction pattern becomes anisotropic with an increase in in-plane diffraction intensity of (100) and (010) peaks when the X-ray beam is parallel to the strain direction (i.e., scattering vector nominally perpendicular to the strain direction). This difference is most clearly observed in the in-plane (100) peaks as indicated in **Figure 35**. This is indicative of alignment of both the P3HT and PCDTPT crystals with the backbone orienting in the direction of strain. When the strain was released, the diffraction anisotropy decreases, with the in-plane (100) diffraction peaks becoming closer in relative intensity, suggesting that the polymer goes back toward an in-plane

isotropic distribution, in agreement with the absorbance anisotropy. Importantly, the diffraction characteristics at a given strain state remain very consistent with increasing strain cycles. In-plane line scans from the 2D images for films in the first strain cycle and after 100 strain cycles are provided in **Figure 37** to highlight the diffraction similarity. These results provide further support that the cyclic deformation process does not significantly change the local order of both polymers in the blend film, including the crystallinity or crystal size.

The morphology of the strained films was further investigated using atomic force microscopy (AFM), optical microscopy, and scanning electron microscopy (SEM) with results given in **Figures 38** and **39** and **Figure 40**. The blend film exhibits some obvious topography changes under large applied strain and strain release. Before being strained, the topography of the film was smooth with an RMS roughness of 1.6 nm. After being strained by 75% there was an increase in roughness resulting in an RMS roughness of 5.1 nm. The increased roughness is attributed to inhomogeneous deformation in the film, resulting in features that appear as partial tears. An AFM line scan that compares the substrate height to the film height, given in **Figure 38j**, shows that these features are not through the film thickness, and the film remains continuous. When the strained film was released to 10% strain relative to its initial length, the partial tearing features appear to close, and the film RMS roughness reduces to 3.9 nm. Under cyclic strain, we find that at a low number of cycles, the topography of the films is repeated at high and low applied strains. As the number of strain cycles increases we begin to observe large protrusions in the AFM images for films at the 10% strain state, which is attributed to localized delamination of the film. Here, the AFM images are for films transfer printed from PDMS to a Si substrate. The delamination of the film is also observed while on PDMS in the optical microscope images (**Figure 39**) and

SEM images (**Figure 40**). Comparing the AFM images to the optical microscope and SEM images shows that the delamination features are similar before and after the transfer-printing step. It is important to note that the chosen strain range represents a limiting case, and increasing the lower strain limit reduces the observed delamination behavior.

As a comparison to the blend films, neat P3HT films were also cyclically strained. Importantly, there are various reports in the literature regarding the crack onset strain of P3HT films, which can vary from 10%<sup>144</sup> to over 150%<sup>151</sup>. The crack onset depends on a number of factors including the molecular weight of the polymer and the source. The neat P3HT used in this study has a crack onset strain of over 150%. Similar to the blend film, the P3HT plastically deforms under strain, and the dichroic ratio increases with applied strain<sup>151</sup>. Unlike the strained blend film, the film roughness remains similar when strained, and no cracks or partial fracture was present<sup>128,151</sup>. Upon strain release from the 75% strain limit, significant delamination of the film occurs. Subsequent strain cycles results in severe delamination, which was observed by optical microscopy in **Figure 39**, and SEM in **Figure 40**. The delamination in the P3HT film is found to be significantly greater than what was found for the blend films and prevented successful transfer printing onto a secondary substrate after the cyclic strain process. The delamination of the P3HT film is consistent with previous work on PEDOT:PSS films where buckling and delamination was observed when large tensile strain applied to ductile films while on an elastomer host was reduced<sup>148</sup>.

During strain reduction, the thin film may buckle out of plane, delaminate, or plastically deform, which depends on the film elasticity, plasticity, and adhesion to the elastomer substrate<sup>154</sup>. The dramatic difference in the cyclic strain character between the blend film and the neat P3HT film is attributed to inhomogeneous elongation that occurs in the film, and a

local change in elasticity. Blending the brittle PCDTPT with P3HT results in a blend film that is nominally not as ductile as the neat P3HT film. This is evidenced by the large increase in film roughness associated with partial tearing observed in the highly strained blend films. Interestingly, the roughness reduces upon strain release suggesting that these localized regions may have a greater plasticity undergoing greater deformation and providing a region of stress relief. The localized thin regions that form during the strain process are not likely to be only one polymer type given that both the PCDTPT and P3HT are shown to orient during the strain process by a similar magnitude. Spin casting a blend consisting of two immiscible polymers has previously been shown to first form a vertical segregation profile followed by a lateral instability and the formation of large lateral segregated domains of the two polymers<sup>155</sup>. The drying kinetics can limit this evolution in the film formation process. Here, we believe that lateral segregation begins to occur in the film; however, solidification arrests the segregation process prior to the formation of pure lateral domains, as previously observed in the 1:1 PCDTPT:P3HT blend films<sup>155</sup>. This lateral segregation of the polymers in the blend then contributes to the lateral thickness variation with large applied strain. Previously we have shown that the elastic modulus of P3HT lowers upon large applied strain<sup>156</sup>. This drop in modulus will reduce the elasticity mismatch between the film and substrate reducing the driving force for film buckling to occur<sup>154</sup>. In addition, as the film is strained, these localized thin regions may have increased compliance and plasticity associated with thin film confinement effects<sup>157</sup>. In contrast, the neat P3HT film does not have a significant change in roughness with tensile strain, such that a localized change in plasticity may not be present. This may contribute to the P3HT film favoring delamination over plastic deformation during strain release. The adhesion of the film to the elastomer substrate may also play a role in the

difference in delamination behavior between the blend film and the neat P3HT film. However, during the transfer printing process, both neat PCDTPT and P3HT films are easily transferred off the PDMS stamp onto a secondary receiving substrate. The secondary receiving substrate includes low surface energy OTS treated silicon, suggesting that both polymers are not strongly adhered to the PDMS. While difference in adhesion between PCDTPT and P3HT may be present, it does not appear to be a primary driving force for the observed delamination behavior.

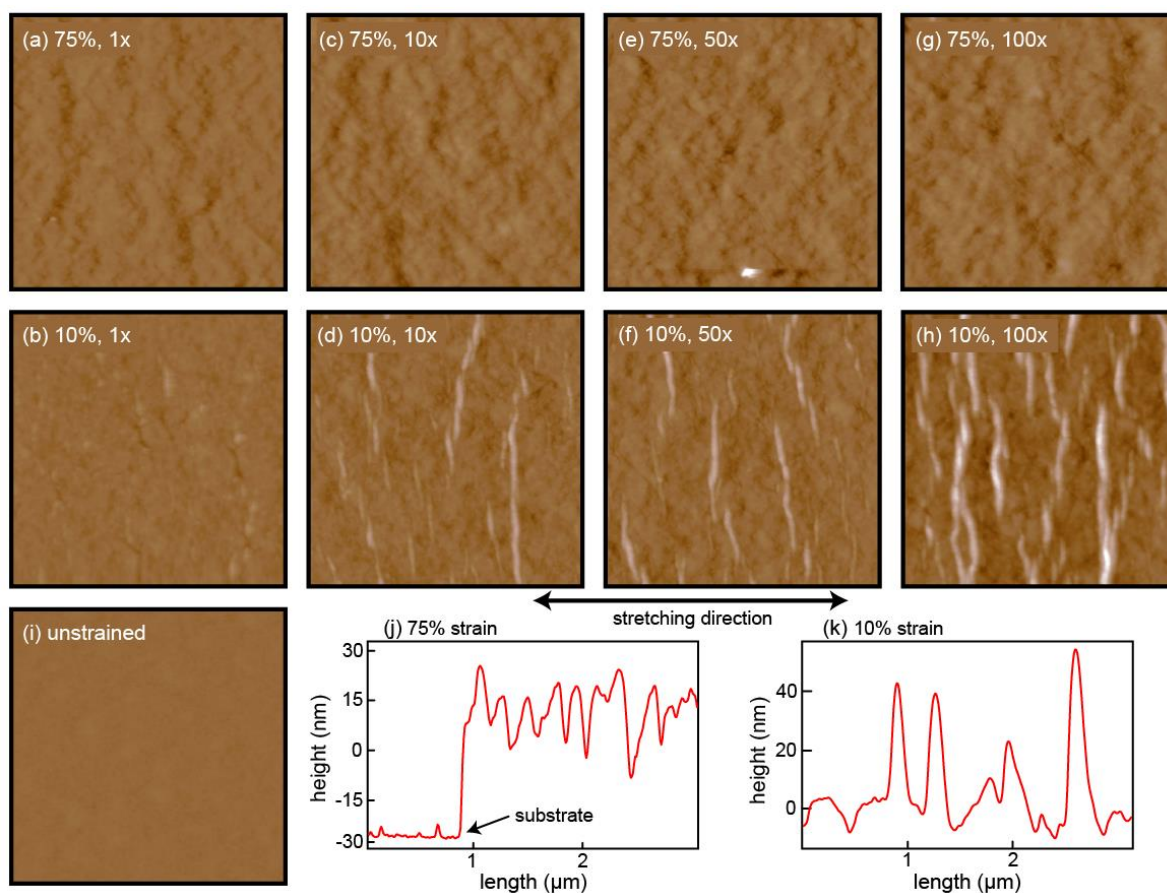


**Figure 38.** AFM height images of films strain by 75% and then lowered to 10% strain after (a,b) 1, (c,d) 10, (e,f) 50 and (g,h) 100 strain cycles. (i) An AFM image of an unstrained film. The area of all images are  $5 \mu\text{m} \times 5 \mu\text{m}$ . The black arrow shown below the AFM images provides the direction the film was strained. Line scans for films at (j) 75% strain and (k) 10% strain after 100 strain cycles. The line scan for the 75% strained film is given at the edge of the film to show that the roughness is not through the film thickness.

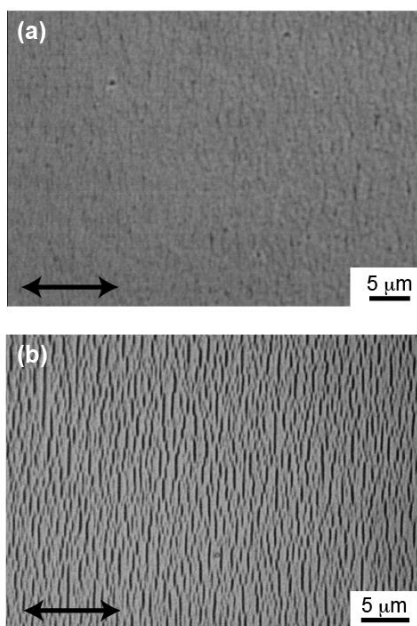


**Figure 39.** Optical microscope image of (a) a PCDTPT:P3HT blend film at 10% strain after 50 strain cycles, and (b) a P3HT film at 10% strain after 10 strain cycles between 75% strain and 10% strain. Arrows in figure indicate the applied strain direction. Both images are taken while on the PDMS substrate. Clear differences in delamination (dark lines) are observed between films.

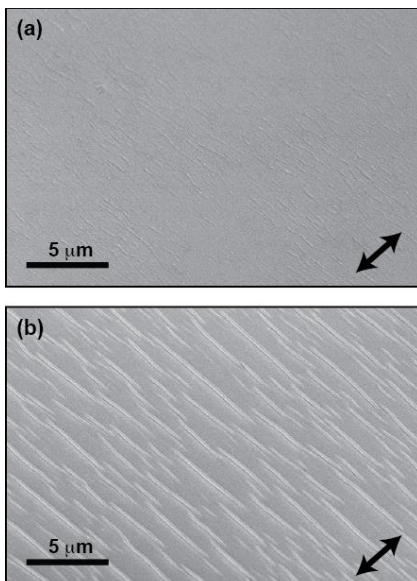


**Figure 40.** SEM images of the (a) PCDTPT:P3HT blend and (b) neat P3HT film after cyclically strained between 75% strain and 10% 10 times and held at the lower strain limit. To image the films the PDMS was adhered to a glass substrate. During this process there was additional strain release and the strain state is closer to approximately 6% strain. The images are taken with the films at a 45-degree tilt.

### ***OTFT Performance***

The ability of the blend film semiconductor to function in a stretchable transistor was tested by cyclically straining the films while on a PDMS host substrate, and then transferring printing the films to a rigid bottom gate bottom contact OTFT test bed for device characterization, as illustrated in **Figure 33(c)**. This approach has been applied in a number of studies of stretchable semiconductors given the simplicity of the approach and ability to focus on the semiconductor layer<sup>115,132,141,151,158</sup>. Once the film was printed, the saturated field effect charge mobility was measured without further processing. The unstrained blend film had a charge mobility of  $0.09 \pm 0.01 \text{ cm}^2 \text{ V}^{-1} \text{ s}^{-1}$  for a  $5 \mu\text{m}$  channel length device. The charge mobility channel length dependence is given in **Figure 41**, showing a drop in mobility with increasing channel length, consistent with low contact resistance behavior<sup>152</sup>. A corresponding neat P3HT film had a charge mobility of  $0.04 \pm 0.01 \text{ cm}^2 \text{ V}^{-1} \text{ s}^{-1}$ , and a neat PCDTPT film had a charge mobility of  $0.10 \pm 0.01 \text{ cm}^2 \text{ V}^{-1} \text{ s}^{-1}$ . The charge mobility of the blend film suggests that charge is primarily transporting through the PCDTPT. It is important to note that PCDTPT and P3HT have a similar highest occupied molecular orbital (HOMO) energy level such that it is possible that charge may transport through both polymers. The measured charge mobility is lower than previously reported for PCDTPT, and PCDTPT:P3HT blend films due to the lack of a thermal annealing step after spin casting the films<sup>119,150</sup>. It was found that when thermally annealing the film immediately after spin casting at the optimized conditions of  $200 \text{ }^\circ\text{C}$  for 10 min, that once the film is strained the charge mobility lowers to a value similar to the film with no thermal annealing, as shown in **Figure 41**. When large tensile strain was applied to the films, the charge mobility increases along the direction of polymer alignment and decreases in the transverse direction, as given

in **Figure 42**<sup>117</sup>. For charge transport in the direction of strain, the charge mobility of the blend film increases to  $0.16 \text{ cm}^2 \text{ V}^{-1} \text{ s}^{-1}$  at 75% strain. Once the strain was released back to 10% strain, the charge mobility decreases and was found to be  $0.08 \text{ cm}^2 \text{ V}^{-1} \text{ s}^{-1}$ . For charge transport perpendicular to the strain direction, the charge mobility decreases to  $0.04 \text{ cm}^2 \text{ V}^{-1} \text{ s}^{-1}$  at 75% strain, and increases back to  $0.1 \text{ cm}^2 \text{ V}^{-1} \text{ s}^{-1}$  upon strain release to 10% strain. The change in charge mobility with strain and strain release is consistent with the changing alignment of the polymer chains in the film<sup>151,159</sup>.

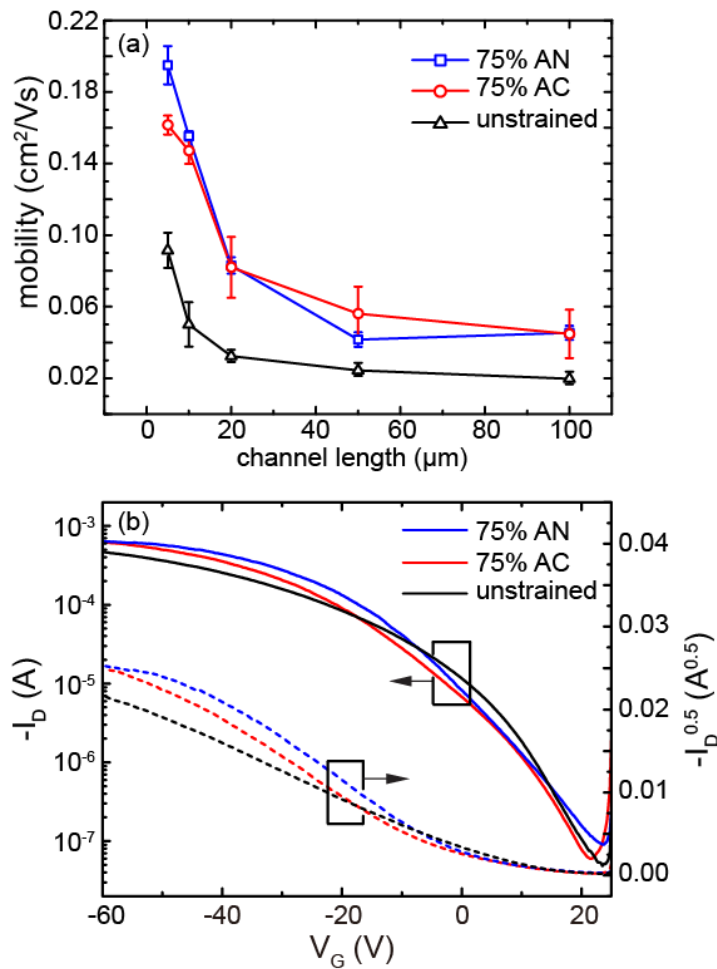


**Figure 41.** (a) Saturated field effect mobility with channel length for an unstrained as cast film, and for charge transport parallel to the strain direction for 75% strained films without thermal annealing (AC) and for a film that is thermally annealed after spin casting at 180C for 10 minutes and then straining the film by 75% and printing onto the rigid testbed. (b) Characteristic transfer curves for 5  $\mu\text{m}$  channel length devices for each of these films.

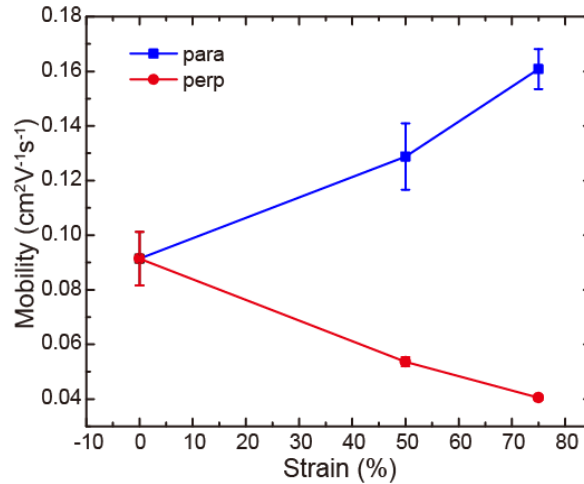


**Figure 42.** Saturated field effect mobility with strain, parallel (para) and perpendicular (perp) to the strain direction for a single tensile strain, for 5  $\mu\text{m}$  channel length devices

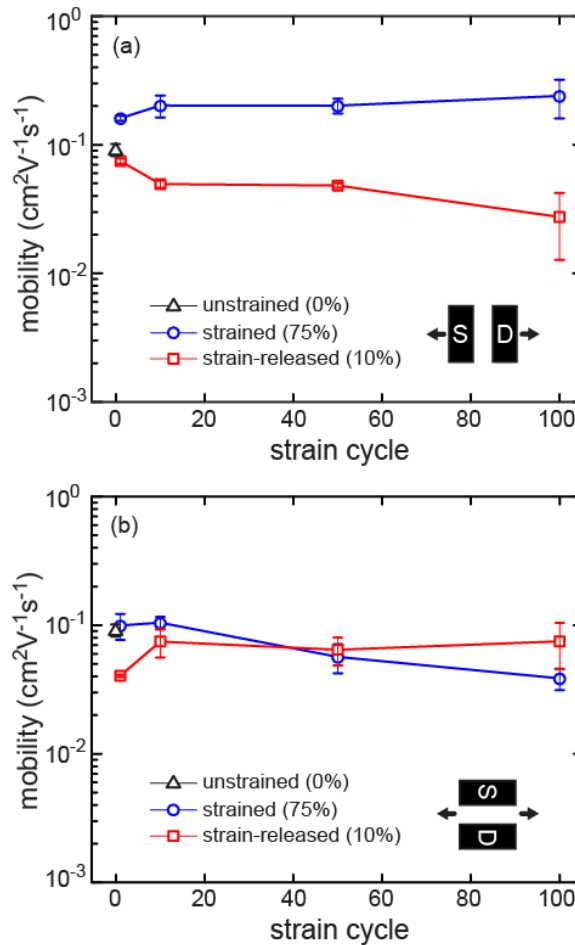


**Figure 43.** Saturated field effect mobility for (a) charge transport parallel to the strain direction, and (b) charge transport perpendicular to the strain direction for films at 75% strain and films released to 10% strain for a specified number of strain cycles. Charge mobility is also reported for an unstrained film. The channel length for the transistors is 5  $\mu\text{m}$ .

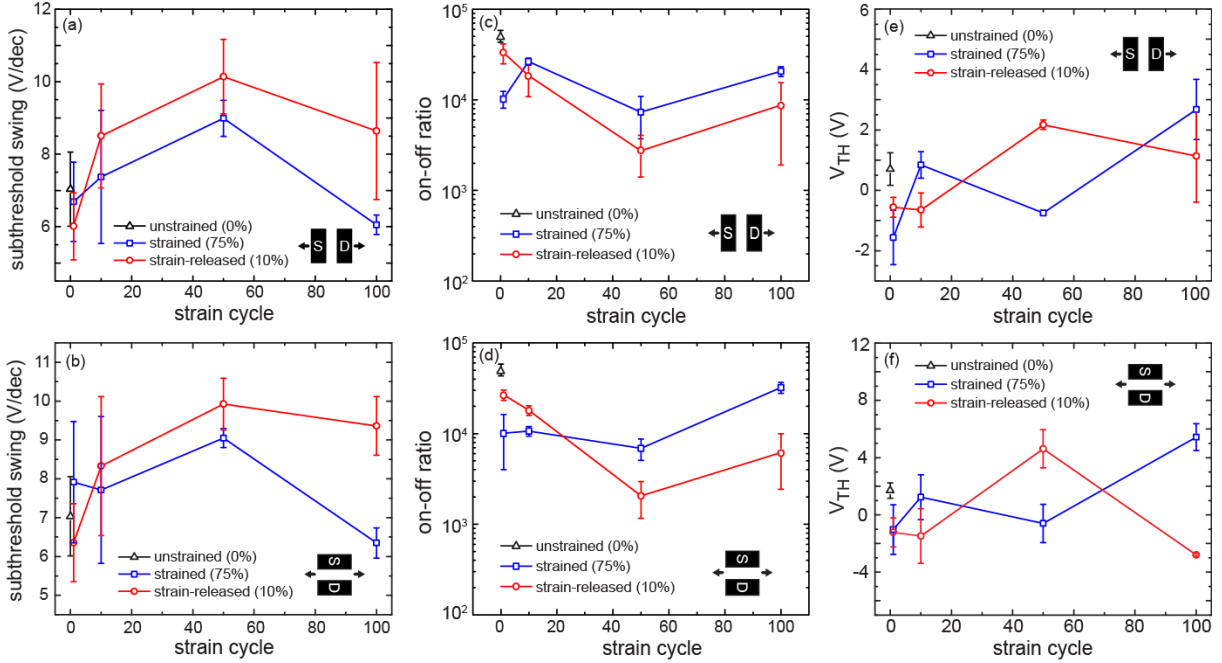


**Figure 44.** Subthreshold swing (a,b), on-off ratio (c,d), and threshold voltage ( $V_{TH}$ ) of the transistor transfer characteristics with number of strain cycles. This includes charge transport parallel to the strain direction (a,c,d) and perpendicular to the strain direction (b,d,f). Values are reported for films held at the 75% strain and 10% strain limits.

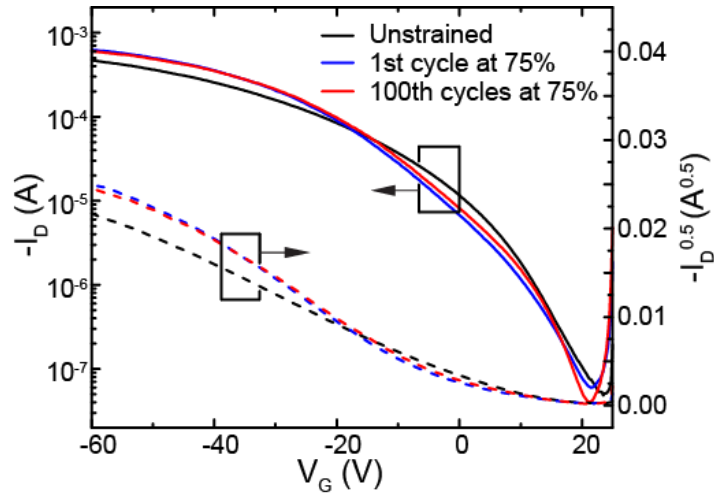


**Figure 45.** Transfer curve for unstrained film and film strain by 75% after 1 and 100 strain cycles for charge transport parallel to the strain direction (without any thermal annealing step).

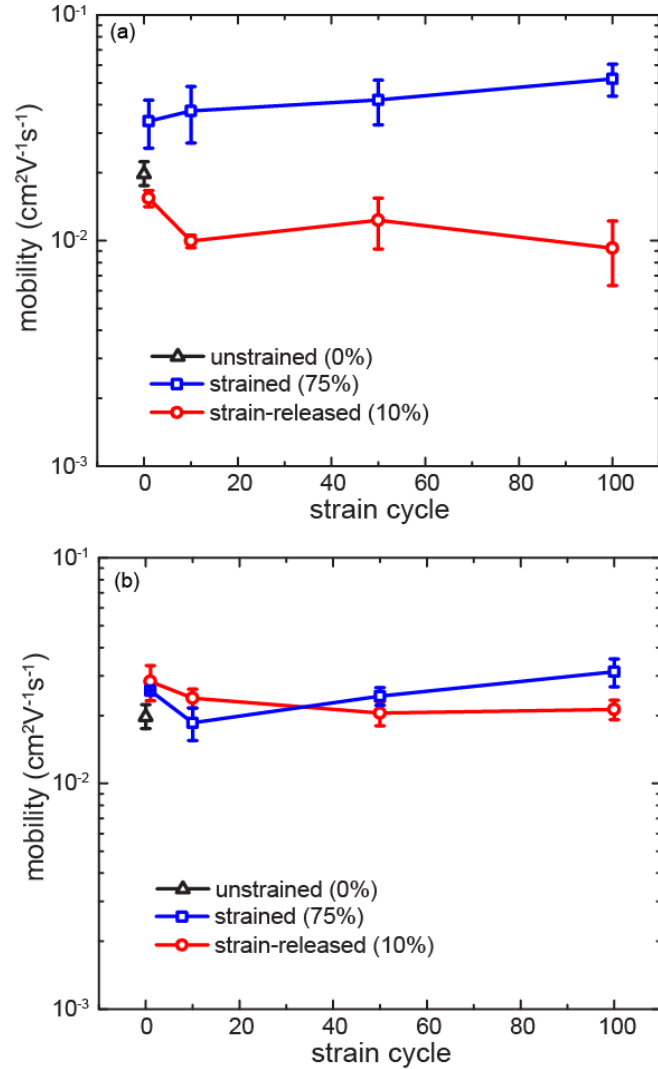


**Figure 46.** Saturated field effect mobility for (a) charge transport parallel to the strain direction, and (b) charge transport perpendicular to the strain direction for films at 75% strain and films released to 10% strain for a specified number of strain cycles. Charge mobility is also reported for an unstrained film. The channel length for the transistors is  $100\ \mu\text{m}$ .

The blend films were further strained between 75% and 10% strain for up to 100 cycles to examine the film's electrical stability, with charge mobility for  $5\ \mu\text{m}$  channel length devices shown in **Figure 43**. The other important transistor characteristics including threshold voltage, subthreshold swing, and on-off ratio are also plotted with strain cycle in **Figure 44** showing relatively stable behavior. The current–voltage curves for a film cyclically strained once and after 100 times are also given in **Figure 45** showing very similar

characteristics. At the 75% strain limit, the charge mobility remains consistent for charge transport parallel and perpendicular to the strain direction. At the 10% strain limit, the charge mobility drops slightly with increasing number of cycles for charge transport both parallel and perpendicular to the strain direction. The drop in mobility is likely associated with the film delamination at this strain state that increases with cyclic strain. The films are being transfer printed by lamination onto the transistor test structure, where any delaminated film may find improved contact on the receiving substrate. Thus, the impact of delamination may not be fully captured with this measurement approach. However, film distortion near the delamination area occurs during the transfer printing process, as observed by AFM, which likely increasing the resistance to charge transport. The charge mobility for long channel lengths (100  $\mu\text{m}$ ) with cyclic strain is given in **Figure 46** showing similar behavior with strain cycle and transport direction. While there was a drop in charge mobility with strain cycle when the film is held at its lower strain limit, the change is relatively small, particularly compared with changes observed in previous approaches such as semiconductor fibril–elastomer composites<sup>113,143</sup>. The OTFT results reported here are compared to recent demonstrations in the literature of stretchable organic semiconductors using a similar testing method in **Table 1**. The comparison includes demonstrations based on block co-polymers<sup>107</sup>, cross-linked polymer semiconductor<sup>143</sup>, crack network films<sup>158</sup>, and fibril–elastomer composite approaches<sup>115,132</sup>. As shown in **Table 1**, the findings reported here are among the highest combination of charge mobility and strain range reported to date.

**Table 1.** A comparison of OTFT characteristics of stretchable organic semiconductors tested on rigid test-beds after cyclic strain. The reported range in charge mobility is for 100 strain cycles, except the block copolymer approach, which is for 1 time tensile strain only.

Approach	Mobility ( $\text{cm}^2\text{V}^{-1}\text{s}^{-1}$ )	On/Off	Strain range (%)	Ref.
Block-copolymer	$<2 \times 10^{-4}$	$10^2$	60	[107]
Semiconductor fibril-elastomer composite	0.006-0.001	$10^5$	50	[113]
Semiconductor fibril-elastomer composite	$<0.001$	$10^3$	100	[143]
Crack network	0.02-0.008	$10^5$	15	[158]
Polymer blend <sup>a)</sup>	0.04-0.02	$10^3$	65	<i>This work</i>
Polymer blend <sup>b)</sup>	0.25-0.16	$10^4$	65	<i>This work</i>

a) Charge transport perpendicular to the strain direction

b) Charge transport parallel to the strain direction at 75% strain

### 2.3.3 Conclusion

Plastic deformation of polymer semiconductor blends has been shown to be a highly effective approach to achieve intrinsically stretchable semiconductors. The PCDTPT:P3HT blend demonstrated here was previously shown to have vertical segregation of PCDTPT toward the interface with the gate dielectric in an OTFT resulting in charge mobility similar to neat PCDTPT films. While charge transport is maintained, the ductile P3HT is mixed throughout the film imparting significant plasticity. Under large tensile strain, both polymers are found to orient in the direction of strain, and upon strain release, the compressive force results in a morphology consistent with polymer chains reorienting back toward an in-plane isotropic distribution. During this process, the local order of the polymer was shown to be remarkably consistent. There does appear to be local material inhomogeneity in the film that results in an increase in film roughness with large applied strain. This turned out to be advantageous, as it provides locations of stress release during the compression of the elongated film back toward its original shape. The film showed no signs of fracture for

strains up to 75% and for 100 strain cycles between 10% and 75% strain. However, as large strain cycles were applied film delamination began to occur at the lower 10% strain limit. When the cyclically strained film was applied in an OTFT, charge mobility was found to track with the polymer alignment. At a given strain state, the charge mobility was found to be consistent up to the 100 applied strain cycles considered in this study; this includes charge mobility consistently above  $0.15 \text{ cm}^2 \text{ V}^{-1} \text{ s}^{-1}$  for charge transport parallel to the strain direction at the 75% strain limit. This approach is the first report to achieve an intrinsically stretchable polymer semiconductor film where the film is comprised solely of semiconductor material. In conclusion, polymer semiconductor blends is a promising and facile method to achieve intrinsically stretchable organic semiconductor films.

### **2.3.4 Experimental section**

#### ***Film Processing***

The blend film was cast from a 4:6 weight ratio of PCDTPT:P3HT dissolved in a 1:1 volume ratio of 1,2-dichlorobenzene:chloroform. The PCDTPT was synthesized following a previously described process<sup>150</sup>, and had a number average molecular weight of  $71 \text{ kg mol}^{-1}$  and a polydispersity of 4.9. The regioregular P3HT was obtained from Sigma-Aldrich, Inc., with a number average molecular weight  $M_n = 54 \text{ kg mol}^{-1}$ , a polydispersity of 2.4<sup>160</sup>. The solution was spun cast onto OTS treated Si substrate at  $1500(2\pi) \text{ rad min}^{-1}$  (1500 rpm) for 30 s at room temperature. The films were then transferred onto a PDMS slab mounted on a custom-made strain stage for subsequent straining and morphological characterization. The strain process was done by hand and the strain rate varied but was at most  $10\% \text{ s}^{-1}$ . The polymer semiconductor films were transferred again to the final receiving substrate for transistor fabrication, X-ray diffraction measurements, and AFM measurements. Cyclic strain

was done in a nitrogen atmosphere and transfer printing was conductive in ambient air. The transfer-printing technique is described in detail in previous work<sup>152</sup>. The PDMS was Sylgard 184 and was prepared at a 10:1 base to cross-linking ratio and cured in a vacuum oven held at  $\approx 85$  kPa at  $60^\circ\text{C}$  over a period of  $\approx 12$  h.

### ***Morphology Characterization***

UV–visible spectroscopy measurements were made using an Ocean Optics Jazz spectrometer. The absorbance of the films was measured while on a PDMS substrate and measured at multiple strain states. The AFM images were measured using an Asylum MFP-3D-BIO in tapping mode. The X-ray diffraction measurements were made at the Stanford Synchrotron Radiation Lightsource (SSRL) on beamline 11–3 with an area detector (Rayonix mar CCD225), an energy of 12.735 keV, and an incidence angle of  $\approx 0.12^\circ$ . The SEM images were measured using FEI Verios 460L field-emission scanning electron microscope. The films were measured while on a PDMS substrate and coated with 10 nm of Au to remove charging effects.

### ***OTFT Characterization***

After straining the film-PDMS stack by a specified amount, the films were transferred printed onto bottom gate, bottom contact OTFT test beds. The source–drain electrodes consisted of a 5 nm Ti wetting layer, followed by 40 nm of Au. The channel length was  $5\ \mu\text{m}$  and the channel width was  $1000\ \mu\text{m}$ . The gate dielectric was an OTS treated  $\text{SiO}_2$  layer that was 300 nm thick. The highly doped Si wafer formed the gate electrode. Charge mobility was measured in the saturation regime with a source–drain voltage of  $-60\ \text{V}$ , and sweeping the gate voltage from  $25\ \text{V}$  to  $-60\ \text{V}$ , with typical results shown in Figure 25. The charge

mobility was determined by taking the slope of the square root of current versus gate voltage over a minimum 5 V range.

## **2.4 The role of elastomer substrate tension, interface stiffness, and adhesion on the behavior of a stretchable polymer semiconductor**

### **2.4.1 Introduction**

Combining stretchability with electronic functionality is poised to advance technologies such as health monitoring and soft robotics as well as open up new technologies previously unachievable due to mechanical limitations of inorganic semiconductors. Intrinsically stretchable polymer semiconductors provide an opportunity to seamlessly integrate devices into stretchable objects. To achieve stretchable polymer semiconductor films, methods have included using a crack network, the use of polymer blends, the development of cross-linked polymer networks, and the use of viscoelastic polymers<sup>111,112,115,116,125,139,143</sup>. The use of viscoelastic polymer semiconductors that can be cyclically strained while maintaining microstructural order and stability provides one promising strategy to achieve intrinsically stretchable devices<sup>111</sup>. Here, the polymer semiconductor deforms in both tensile and compressive strain while maintaining stable electrical characteristics<sup>111</sup>. Typically, the neighboring elastomer provides the driving force for the deformation of the semiconductor<sup>161</sup>. The success of this approach relies on the viscoelastic behavior of the semiconductor film. To manage viscoelasticity, polymer semiconductor backbone, side-chains, molecular weight have all been modified to promote the desired mechanical behavior<sup>117,118,146,148</sup>. Additionally, copolymers and polymer blends have been explored<sup>107,111,114</sup>. In cases of large cyclic strain where the film undergoes plastic deformation, eventual physical failure may occur through film morphological changes, formation of discontinuities in the film, or delamination of the film from the neighboring substrate<sup>111,139,162</sup>.

In this article we consider the characteristics of the neighboring elastomer on the ability to plastically deform the polymer semiconductor film in a repeated manner with minimal morphological impact. We consider the polymer semiconductor poly[2,5-bis(2-octyldodecyl)pyrrolo[3,4-c] pyrrole-1,4(2H,5H)-dione-3,6-diyl)-alt-(2,2';5',2'';5''', 2''''-quaterthiophen-5,5''''-diyl)] (DPP-4T) film on a polydimethylsiloxane (PDMS) elastomer substrate. DPP-4T is chosen as it has been reported to possess a high hole mobility approaching  $1 \text{ cm}^2/\text{Vs}$ <sup>163–165</sup>, and as shown has a glass transition temperature significantly below room temperature. PDMS is chosen as it is a popular silicone elastomer with high extensibility, clarity, high chemical resistance, high thermal stability, and is widely used in stretchable organic electronic demonstrations<sup>96,115,166,167</sup>. PDMS is also widely applied in thin film mechanical characterization<sup>146,154,156,159,167</sup>. While the focus here is on plastic deformation of the active layer, many of the findings are applicable to other stretchable polymer conductor approaches that employ an elastomer substrate.

The focus on the investigation is on the role of adhesion between the elastomer and the polymer semiconductor film, the stiffness of the underlying elastomer, and tension of the elastomer on the deformation behavior of the semiconductor film under cyclic strain. The PDMS surface energy, and near surface stiffness was modulated through UV/ozone treatment. The films are probed in a quasi-in-situ manner by UV-visible spectroscopy and atomic force microscopy using a strain stage that can be integrated with both instruments. We find that the increase in elastic modulus of the near surface PDMS and the increase in adhesion energy between the PDMS and DPP-4T significantly improve the morphological stability of the DPP-4T films. The strain at fracture of the thin film is improved with greater substrate adhesion, similar to other reports<sup>124,166</sup>. The PDMS treatments also results in a

reduction in the both the formation of thin film wrinkles and delamination under cyclic strain of approximately 40%. We show that the film can be cyclic strained up to 100 times while showing stable surface roughness and stable local polymer order. This improvement in physical stability is attributed to the reduced elastic modulus mismatch between the film and substrate, the increased adhesion of the film to the substrate, and maintaining the PDMS substrate in tension throughout the cyclic strain range considered. In this analysis, we also show that the lack of film wrinkling over the strain range considered does not necessarily equate to being within the elastic strain limit as previously reported<sup>166</sup>. Alternatively, we show that the polymer film reaches its yield stress prior to reaching the critical stress required for wrinkling thus eliminating wrinkling under stretching.

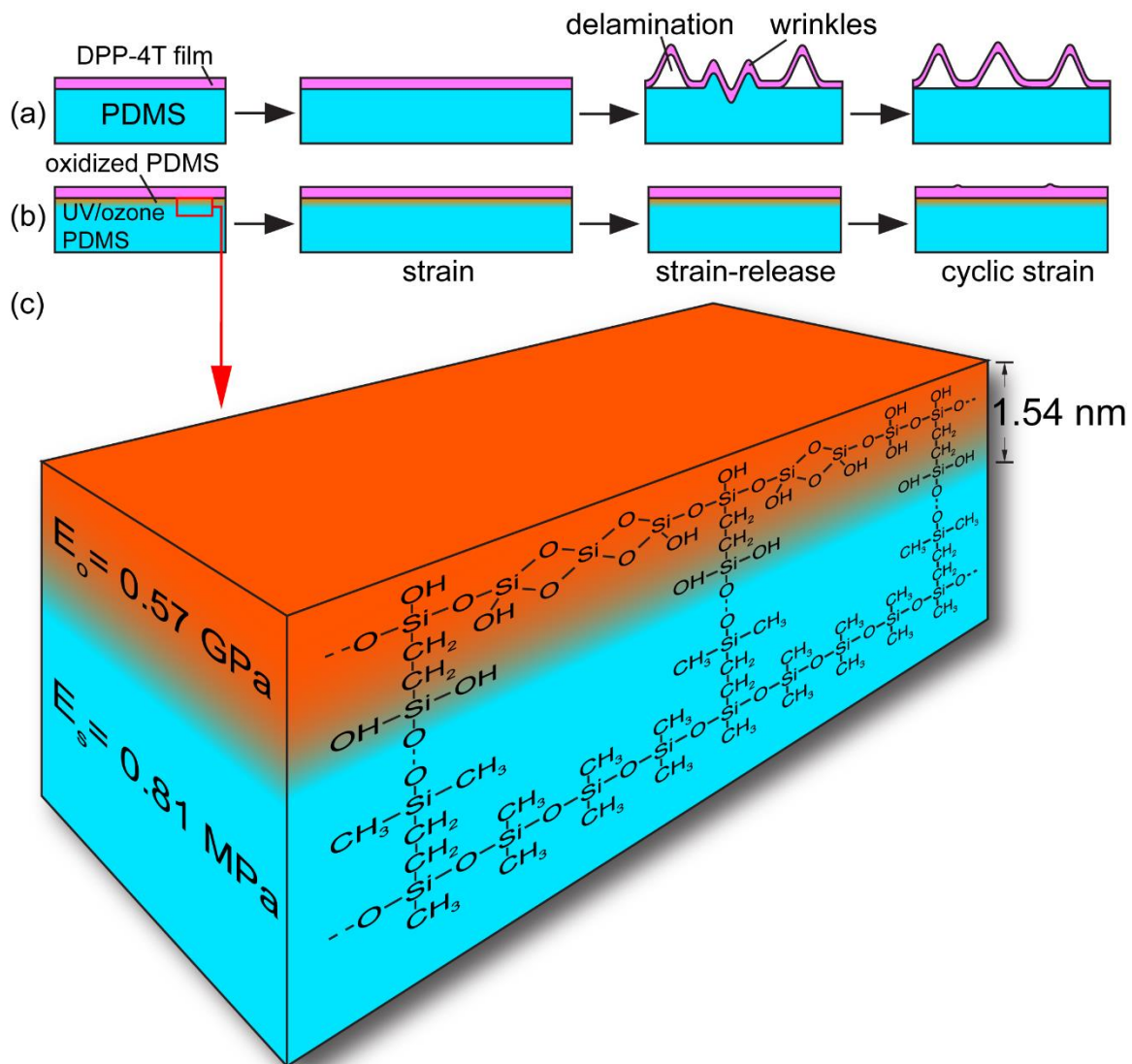


**Figure 47.** Illustration of the change in the films surface morphology when on the (a) normal PDMS substrate and (b) UV/ozone treated PDMS substrate during the cyclic strain process from the side view. (c) UV/Ozone treatment effect on PDMS.

## 2.4.2 Results and Discussion

### *PDMS characterization*

The PDMS substrate surface energy, and near surface stiffness was modulated through UV/ozone treatment. When exposed to plasma or UV-Ozone, the methyl group of PDMS convert into hydrophilic moieties and thus increases the surface energy<sup>168-170</sup>. At the same time, a silica layer begins to form at the surface of the substrate, resulting in an increase in stiffness near the substrate surface<sup>169,171</sup>. The use of UV/ozone treatment has been previously shown to improve adhesion of polymer semiconductor and metal films, improving the strain at fracture<sup>148</sup>. The UV/ozone treatment conditions are constrained for the PDMS due to the embrittlement of the surface by the silica formation. An untreated PDMS substrate can be strained by over 100% prior to rupture. The formation of the silica layer results in surface cracks that form prior to this rupture limit. Nevertheless, under limited UV/ozone treatment, an incomplete layer of silica forms such that the surface retains elastomeric properties and allows for the PDMS to be strained significantly without surface crack formation. When the PDMS is treated with UV/ozone for 20 min, surface cracks will appear under an optical microscope at strains of approximately 65%. At strains less than 65% the film can be cyclically strained without crack formation. Here, we limit our analysis to PDMS with UV/ozone treatment times of 10 and 20 minutes.

The surface energy of PDMS under different UV-Ozone treatment condition is first characterized with water contact angle measurements. The contact angle results are shown in **Figure 48** for untreated PDMS and PDMS under UV-Ozone treatment for 10 min and 20 min. As expected, the contact angle drops with increasing treatment time in a nearly linear manner, indicating the surface energy is increasing. This is a results of methyl (-CH<sub>3</sub>) group

on the PDMS surface being oxidized into hydroxy (-OH) group and eventually converts the CH<sub>3</sub>-Si-O- structure into a hydrophilic ceramic -O-Si-O- network<sup>168</sup>. The contact angle was measured after 5 hours for 20 min UV/Ozone treated PDMS and the value shows negligible variation. The stable contact angle suggests the hydrophobic recovery in the treated PDMS, which is known to occur<sup>172,173</sup>, does not happen with any significance over the first 5 hours after treatment. All subsequent experiments using the treated PDMS occurred within 5 hours allowing the film behavior to be considered without considering the recovery of PDMS surface layer.

The adhesion energy between thin DPP-4T film and PDMS substrate was determined by 90° peeling test, with results shown in **Figure 2**. The DPP-4T film was peeled from the PDMS using Scotch magic tape. The force and displacement were recorded, and the period over which the applied force is stable is used to determine adhesion energy. The adhesion energy ( $\Gamma_c$ ) was calculated by  $\Gamma_c = F/w$ , where  $F$  is average peeling force, and  $w$  is the width of tape<sup>174</sup>. The adhesion energy for DPP-4T thin film onto neat PDMS is found to be 0.048 J/m<sup>2</sup>, which is consistent with previous adhesion result of semiconductor polymer thin film onto PDMS<sup>175</sup>. Then adhesion energy increases to 0.16 J/m<sup>2</sup> and 0.32 J/m<sup>2</sup> with 10 and 20 minutes of UV/ozone treatment, respectively.

The UV-Ozone treatment on PDMS not only changes the surface energy, but also increases the stiffness of the PDMS surface<sup>168-170</sup>. To determine the increase in surface stiffness, we applied a previously described wrinkling method<sup>156,176</sup>. The method is based on the interfacial instability generated from the modulus mismatch between a stiff film on a compliant substrate when under compression, which in this case is silica-like layer and neat

PDMS, respectively. This interfacial instability results in a buckling with a characteristic wavelength ( $\lambda$ ), and the elastic modulus of the thin film can be given by

$$E_u = 3E_s \left( \frac{1 - \nu_u^2}{1 - \nu_s^2} \right) \left( \frac{\lambda}{2\pi h_u} \right)^3, \quad (24)$$

where  $E$  is the elastic modulus,  $\nu$  is the poisson ratio, and  $h$  is the thin film thickness. The subscripts  $u$  and  $s$  are for the film and substrate, respectively. Here, the modified surface of the PDMS is considered the film on the unmodified PDMS substrate. To generate the wrinkles, the PDMS was strained by 15% and then treated with UV-Ozone for 20 minutes. The PDMS was then compressed until surface wrinkles were formed. The wavelength of the wrinkles was measured using Atomic Force Spectroscopy (AFM), with results shown in **Figure 49** and the average wavelength is 58.5 nm. The thickness of the surface layer ( $h$ ) is measured using variable angle spectroscopic ellipsometry (VASE, Woollam M2000). This approach has been previously applied to measure the silica layer thickness in ozone treated PDMS<sup>177</sup>. While, it is expected that there is a gradient in the silica concentration with depth<sup>178</sup>, we apply a simple 2 layer model for the VASE using a Cauchy model for the modified surface layer. Using this approach,  $h$  was determined to be 1.54 nm, with the model fit given in **Figure 50**. The elastic modulus of the PDMS substrate ( $E_s$ ) is determined to be 0.81 MPa by performing a standard tensile test on an untreated PDMS substrate.  $\nu_u$  and  $\nu_s$  are taken as 0.33 and 0.5, respectively<sup>171</sup>. Applying these values to equation (24), the surface modulus for 20-minute UV-Ozone treated PDMS is calculated to be 570 MPa. This should be taken as an approximate value given that a gradient in surface modulus should exist. In addition, previous research has shown a wrinkle wavelength dependence on the PDMS pre-strain<sup>176</sup>. Nevertheless, this increase in the PDMS modulus near the substrate surface reduces the modulus mismatch between DPP-4T film and PDMS substrate and will effect DPP-4T

wrinkling behavior when under strain, discussed further below. The elastic modulus was determined for the DPP-4T films using the same approach and was measured to be 120 MPa.

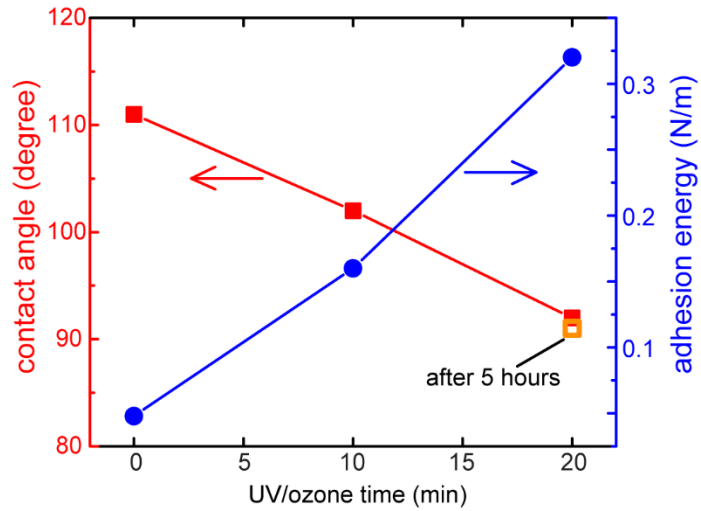


**Figure 48.** Contact angle and adhesion energy for PDMS under different UV/ozone treatment time.

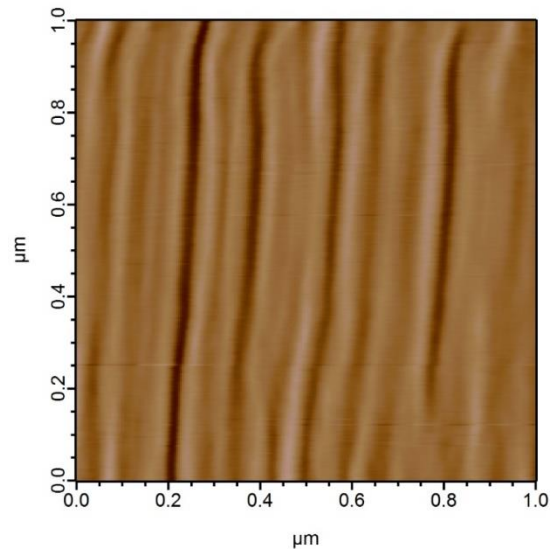


**Figure 49.** AFM surface morphology of a buckled PDMS at rest obtained with 15% pre-strain and UV/ozone treatment for 20 min.

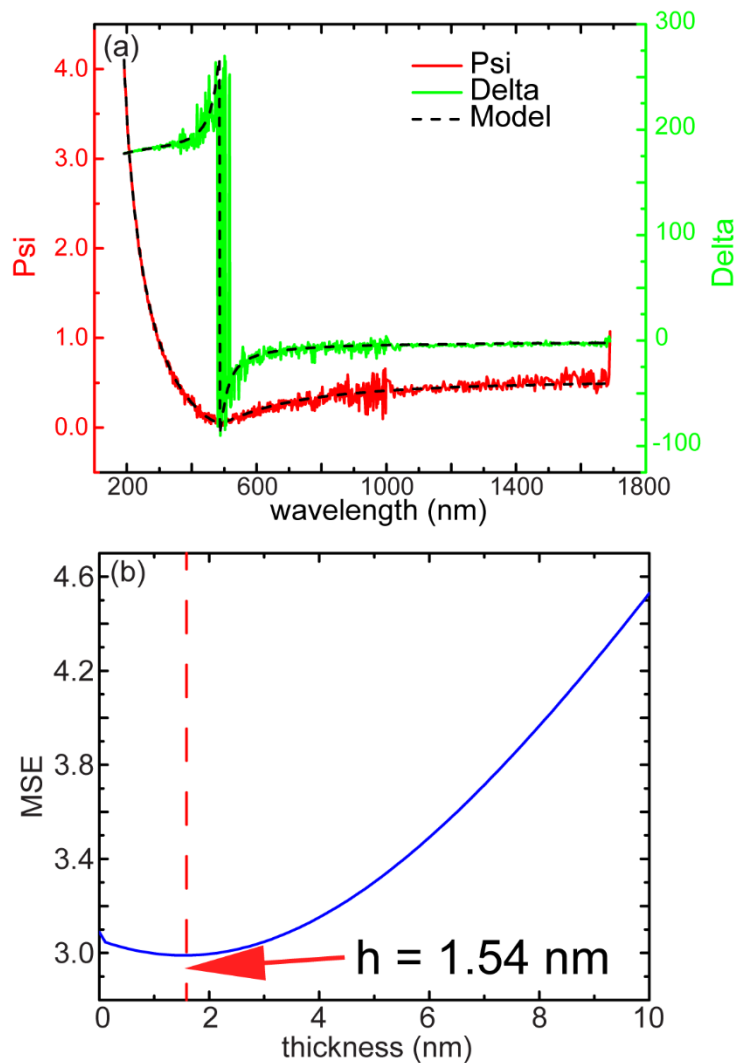


**Figure 50.** Characterization of UV/Ozone treated PDMS surface layer thickness using ellipsometry. (a) Psi and Delta fitting of measured data with existing model. (b) Uniqueness analysis of Mean Squared Error (MSE).

### *Wrinkle onset strain and yield point*

Under large cyclic strain, the viscoelastic film may wrinkle while on the elastomer substrate. In some studies, film wrinkling is exploited as a means to achieve stretchability<sup>104,143</sup>. In these cases, the films are kept within its elastic limit and the strain is limited to a range of stable wrinkle formation. Here, we regard the wrinkling as an undesirable defect. The wrinkling will limit the strain range. In compressive strain, after the

wrinkles have formed, continued compression results in stresses that promote film delamination<sup>179</sup>. In addition, out of plane wrinkling may limit some device designs and applications.

Here, we are interested in determining the role of the substrate on the onset of wrinkling of the polymer film under cyclic strain and its relationship to film yielding. It has been previously been proposed that the yield strain of a polymer thin film can be found by placing the film on an elastomer and cyclically straining the film/elastomer composite over increasing strain ranges until wrinkles are observed when the strain is removed<sup>166</sup>. It was argued that over the elastic regime, the strained film and substrate both return to their original shape without wrinkling. Past the yield point, the film is plastically deformed and when the strain is released from the PDMS substrate, a compressive force will act upon the strained film resulting in film wrinkling. However, there is the competing mechanism of plastic deformation of the film. If the yield stress is met prior to the critical stress for wrinkling, then plastic deformation will occur prior to wrinkling. The stress strain behavior of the film will then dictate when wrinkling will occur.

To consider the onset of wrinkling, the film is laminated onto a PDMS substrate while both being in an unstrained state. The film/PDMS composite are then strained to a specified strain and returned to the unstrained state. This is done in a custom strain stage such that the film topography can be measured by AFM while on the strain stage. At the unstrained state, the surface is measured by AFM to determine the onset of wrinkling. If no wrinkles are found, a large tensile strain is applied to the film, and the measurement is repeated. This approach is similar to others previously described<sup>112,166</sup>. The wrinkle onset strain of the DPP-4T film onto PDMS is characterized for 30 nm and 150 nm thick films, and on PDMS

substrates with different UV/ozone treatment times. The maximum applied strain at which point wrinkles were observed by AFM in the unstrained state is considered the wrinkle onset strain. The wrinkle onset strain for the two film thicknesses considered, and the various UV/ozone treatments is given in **Figure 52**. AFM images of the films just prior to reaching, and just after reaching the wrinkle onset strain are given in **Figure 51**.

For 30 nm thick film, the wrinkle onset strain is around 18% with neat PDMS. Then it increases to 40% for 10 min treated PDMS and further increases to 48% for 20 min treated PDMS. The wrinkle onset strain for 150 nm film follows the same trend but with overall lower values. Although the wrinkle onset strain is a result of the film being plastically deformed, it doesn't capture the onset of plastic deformation, or yield point, and turns out to be highly dependent on the substrate processing.

To illustrate the substrate's effect, we characterized the amount of film retraction of a strained DPP-4T film after removing the film from the PDMS substrate. This was done by straining the film while on PDMS and then floating the film off the substrate onto water. Once removed from the substrate, the thin film will contract based on the elastic strain retained in the strained film. The shrinkage of the film,  $[(\text{final length} - \text{strained film length})/\text{strained film length}]$ , can be roughly considered the elastic strain retained in the film. This should be approximately equal to the yield strain of an unstrained film. We find that for films strained by 45% and floated in water, the shrinkage is roughly 4%, independent of the film thickness and the UV/ozone treatment of the PDMS substrate. This highlights the intrinsic property of the film, rather than the influence of the substrate.

The differences between wrinkling onset strain and yield point results suggest that the substrate has a very strong impact on the thin film deformation mechanism. Since the

polymer semiconductors are usually fabricated into thin film of tens of nanometer, its mechanical characterization is normally done on an elastomer substrate such as PDMS. In this system, the stress that is applied on the substrate will be transferred to the thin film through shear stress at the interface, and eventually force the film to move together with the substrate <sup>161</sup>. The UV/Ozone treatment on PDMS helps improving film's ability to deform without failure from two aspects. First, it increases the adhesion energy between film and substrate. During the strain process, a high adhesion energy is usually believed to increase the crack onset of the thin polymer film due to the uniform strain at each point reducing the localized strain and potential delamination <sup>124</sup>. While during the strain release process, the substrate will force the thin film to compress within the plane until the strain energy release rate exceeds the interfacial toughness in certain regions resulting in localized delamination <sup>180</sup>. A high adhesion energy increases the interfacial toughness between film and substrate and delay the point when film start to delaminate. The strain energy release rate is proportional to the thin film thickness, and therefore the thicker film delaminates earlier than thinner film, as shown in **Figure 52**.

The other advantage of UV/Ozone treatment on PDMS is that it increases the surface modulus of PDMS by forming a silica layer which may eliminate the buckling. The effect of the high modulus silica layer on the buckling phenomenon can be analyzed using the extension of well-established buckling equation. Assume both DPP4T film and silica-like PDMS thin layer buckle when the strain is released. The equation for the bending process is given as

$$(\overline{E}_f I_f + \overline{E}_u I_u) \frac{d^4 z}{dx^4} + (F_f - F_u) \frac{d^2 z}{dx^2} + kz = 0, \quad (25)$$

in which  $\bar{E} = E/(1-\nu^2)$  is the plane-strain modulus,  $E$  is the Young's modulus,  $\nu$  is the Poisson's ratio,  $I = wh^3/12$  is the moment of inertia where  $w$  is the width of the film and  $h$  is its thickness,  $F$  is the uniaxially applied force,  $k = \bar{E}_s w \pi / \lambda$  is the Winkler's modulus of an elastic half-space, and  $z(x) = A \sin(2\pi x / \lambda)$  is the sinusoidal vertical deflection of the film and oxidized PDMS. The subscripts,  $f$ ,  $u$  and  $s$  denote the DPP-4T thin film, oxidized PDMS layer and PDMS substrate, respectively. By rearranging the terms in Eqn. (26) and minimizing the applied force ( $\partial(F_f - F_u) = 0$ ), an optimal wavelength  $\lambda$  is calculated to be

$$\lambda = 2\pi \left( \frac{\bar{E}_f h_f^3 + \bar{E}_u h_u^3}{3\bar{E}_s} \right)^{\frac{1}{3}}. \quad (26)$$

Given the very small thickness of oxidized PDMS layer compared with polymer film, the second term in the numerator can be neglected and treated as zero. This means the thin silica layer has very little effect on the buckling wavelength. With the optimal wavelength, the critical stress can be obtained as

$$\sigma_c \approx \left( \frac{9}{64} \bar{E}_f \bar{E}_s^2 \right)^{\frac{1}{3}} + \frac{F_u}{h_f w} = \left( \frac{9}{64} \bar{E}_f \bar{E}_s^2 \right)^{\frac{1}{3}} + \frac{E_u h_u \times \text{strain}}{h_f}, \quad (27)$$

The first term in Eqn. (28) is the same as critical stress for stiff film onto soft substrate, and the second term comes from the tensile stress in the oxidized PDMS layer. In other word, in order to buckle, the polymer film need to overcome the tensile stress in the oxidized thin PDMS first. Based on the modulus measured in the early text, the first term is about 2.76 MPa, while the second term is about 28.5 MPa multiplied by strain. Therefore, the critical stress for buckling is significantly increased compared with film onto normal PDMS substrate. And this may cause the stress in the film smaller than the critical stress therefore eliminate the appearance of buckling.

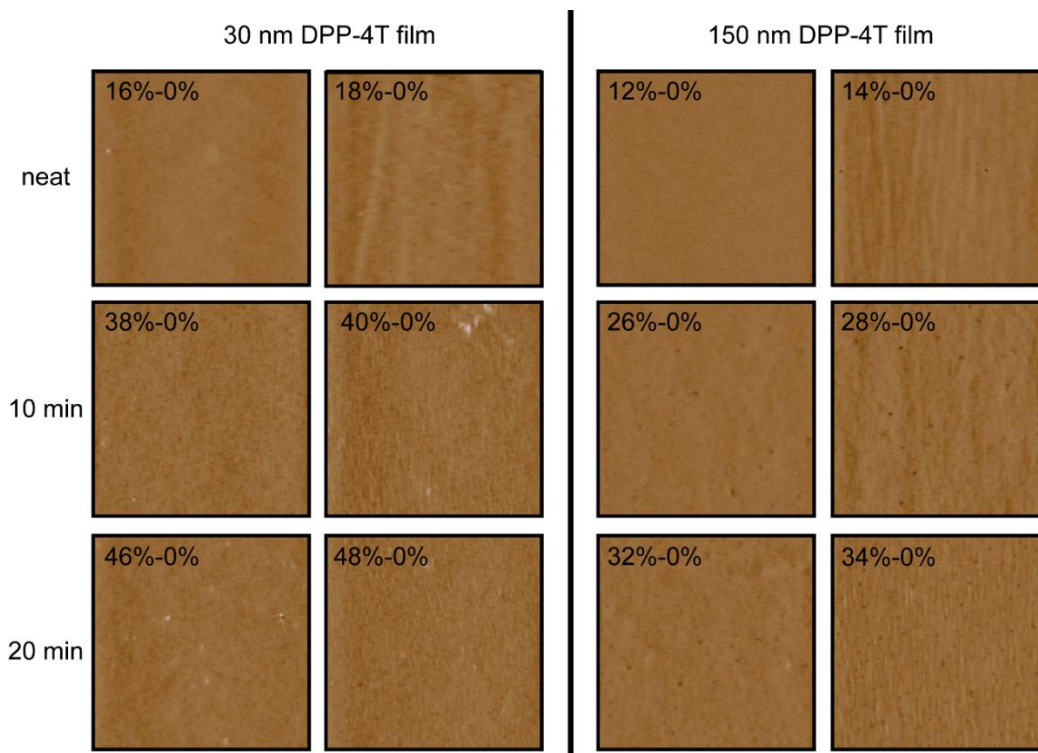


**Figure 51.** AFM scanned surface morphology for 30 nm and 150 nm DPP-4T film before and after reaching the YOE and YOW.

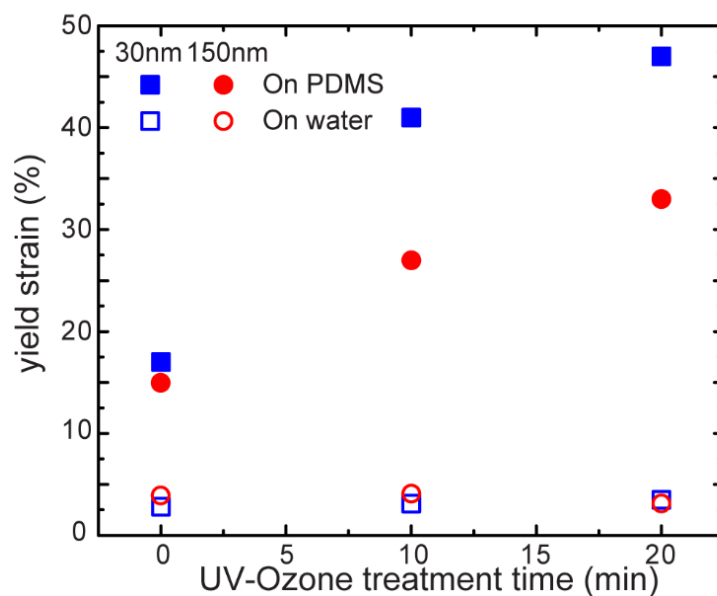


**Figure 52.** Yield point on elastomer (YOE) and yield point on water (YOW) for films onto PDMS with different UV/ozone treatment time.

### *Film Morphology under cyclic strain*

Films were first spun cast onto octyltrichlorosilane (OTS) treated silicon substrate and then printed to a free standing PDMS elastomer slab. For cyclic strain, two different strain ranges are used here: from 5% to 45% and from 20% to 60%. The film-PDMS stack was strained to either 45% or 60%, and then strain was released back to 5% or 20%, respectively, and repeated for a specified number using a motorized strain stage. All the strain values in this work are calculated relative to the film unstrained state. After the strain process was complete, the films were characterized on the PDMS substrate. The specially designed low depth profile strain stage can be easily fit under the AFM. This allows us to perform the AFM with the film-PDMS on the strain stage and continue to strain them after the scan is finished, therefore realize the in-situ characterization during cyclic strain.

The surface morphology and RMS roughness of 30 nm DPP-4T film onto PDMS with different UV-Ozone treatment time and different strain range during the cyclic strain is given in **Figure 53** and **Figure 54**. Before being strained, the topography of the film was smooth with a low RMS roughness below 1 nm. After being strained by 60%, RMS roughness for neat, 10min-UVO and 20min UVO PDMS all slightly increased above 1 nm, and stays stable even after 100 cycles. The DPP-4T we used in this work possess a crack onset strain over 80%. Therefore, when being strained under this value, cracks and large variation of RMS is not expected to appear and topography seems likely to be independent of the adhesion energy. When the strained film was released to 20% strain, the topography starts to diverge. For film onto neat PDMS, some protrusions start to show up in the AFM images which is due to localized delamination and RMS roughness increases to 6.9 nm. As the cycle number increases to 100, the protrusions become taller and wider and RMS roughness further

increases to 15.4 nm. In comparison, the RMS roughness for film onto 10 min UVO PDMS stays low at 2.2 nm at 1<sup>st</sup> cycle and moderately increases to 4.8 nm after 100 cycles with smaller protrusions than film onto neat PDMS. And when UV-Ozone treatment further increases to 20 min, only extremely small protrusions appear with amplitude less than 5 nm and the RMS roughness stays low at 2 nm even after 100 strain cycles.

During the strain reduction, the thin film onto a soft substrate may move out of the plane, forming wrinkles, buckling or delamination depending on the film intrinsic mechanical properties, adhesion to the elastomer substrate as well as substrate properties <sup>154</sup>. The dramatic difference in the cyclic strain character among films onto PDMS under different UV/ozone treatment time is mainly attributed to the increasing adhesion energy between thin film and PDMS substrate, as indicated by the peeling test result shown in the early text. For film onto neat PDMS, the delamination happens when film is being strain release for the first time indicating the stress in the film is larger than the delamination critical stress. In the following cyclic strain, the delamination propagates from the failure region, and combines into protrusions with bigger amplitude. After UV/ozone treatment, the critical stress for delamination is increased. Therefore, for film onto 20 min UV/ozone treated PDMS, no extrusion is observed indicating stress in the film is smaller than the delamination critical stress and this strong adhesion is forcing the film stays in the plane undergoing plastic compression. The continued cyclic strain induces the small increment in the RMS roughness and subtle protrusions. This is classic fatigue failure that happens even when the film stress is smaller than the critical failure stress. In this failure mode, repeating strain keeps weakening the interfacial bonding between thin film and PDMS substrate until the appearance of subcritical delamination, which is shown as subtle light region with tens of nanometer width

and several nanometer amplitudes. However, the growth and propagation of this subcritical delamination is rather slow. After 100 cycles, the subcritical delamination almost keeps its size, with slightly increasing amount. The result indicates that a strong adhesion between thin film and PDMS substrate will improve the mechanical resistance under monotonic loading as well as cyclic loading.

Besides the adhesion energy, the other reason for the reduction of wrinkles come from the change in the surface mechanical property after UV-Ozone treatment. It is well known that when a stiff thin film onto soft substrate is under compression, interfacial instability will induce the surface buckling<sup>154</sup>. The elastic modulus of 30 nm DPP-4T film was measured using aforementioned buckling method and calculated using Eqn. (24), and is determined to be 120 MPa. After 20 min UV-Ozone treatment, the surface modulus of PDMS is shown to increase from 0.81 MPa dramatical to 570 MPa, which is discussed in the early text. And the existence of high modulus thin oxidized PDMS layer increases the critical stress for buckling therefore eliminated the appearance of buckling phenomenon.

DPP-4T film was also conducted cyclic strain under a different strain range from 5% to 45%. For film onto PDMS with 10min and 20min UV/ozone treatment, the surface morphology and RMS roughness are almost identical to that of film being strained from 20% to 60%. While when the PDMS is neat, the film presents slightly lower RMS roughness when being released back to 5% than the film being released to 20%. The possible explanation could be a higher strain energy rate at 60% strain than 45% strain that results in localized weak adhesion region which is easier to delaminate under compression.

Then the change in morphology is characterized by measuring the absorbance of cyclic strained film with UV-vis spectroscopy under linearly polarized light with the film onto

PDMS substrate. DPP-4T absorb light over a range wavelength from 400 nm to 1000 nm, with a major peak at 784 nm and a secondary peak around 450 nm, as shown in **Figure 55**. The shoulder at 700 nm indicate the polymer chain forms H aggregates<sup>181</sup>. When the films are strained, the absorbance of linear polarized light parallel to the strain direction increases, while the absorbance of polarized light perpendicular to the strain direction decreases over the entire spectral range. This dichroism is associated with the alignment of the polymer backbones along the strain direction<sup>151</sup>. To quantify the alignment of the polymer during strain process, we calculated the dichroic ratio of the film at the wavelength of 784nm for both strain range (5% to 45% and 20% to 60%) and onto PDMS with different UVO treatment time. We find that the dichroic ratio is almost independent of PDMS surface treatment, as shown in **Figure 55** and **Figure 56**. At 60% strain, the dichroic ratios are found to be 1.97, 1.99 and 1.95 for film onto neat, 10min UVO and 20min UVO PDMS, respectively. When film is strain released to 20%, dichroic ratios drop down slightly faster than that during strain process, and are found to be 1.12, 1.13 and 1.13 for film onto neat, 10min UVO and 20min UVO PDMS, respectively. For films being strained to 45% then back to 5%, the dichroic ratios are found to be 1.73, 1.77 and 1.76 at 45%, and 0.93, 0.94, 0.90 at 5% for film onto neat, 10min UVO and 20min UVO PDMS, respectively. The dichroic ratio below 1 indicates the polymer chains are being aligned more along the perpendicular to the strain direction by compression. The dichroic ratios for films onto different surface under cyclic strain are also monitored and are found to be consistently repeated for all the situations, as shown in Figure 6. The consistency of the dichroic ratio indicates the morphology doesn't change much during the cyclic strain up to 100 cycles and independent of substrate surface treatment. The normalized absorbance for films being strained to 60%

and 45% the 1<sup>st</sup> time and 100 cycles, and films released back to 20% and 5% the first time and 100 cycles onto PDMS with different UVO treatment time is also shown and no significant change happens before and after 100 cycle strain. The similar absorbance features indicate the similar DPP-4T aggregation order.

### **2.4.3 Conclusion**

UV/ozone treatment on the surface of PDMS substrate prior printing the polymer semiconductor film has been shown to be an effective and easy approach to achieve stretchable semiconductors. The surface layer PDMS under UV/ozone becomes more hydrophilic with higher surface energy, and form a stronger bonding when polymer film is printed onto the PDMS surface. The higher adhesion energy increases the critical stress for delamination and greatly improve the wrinkling onset strain from 17% to 47%. However, the intrinsically property of polymer has not been change, with a constant yield point on water below 5% independent of UV/ozone treatment. The mechanical property of surface PDMS has also been changed, with a modulus increasing from 0.89 MPa to 0.57 GPa. The existence of thin oxidized PDMS layer with large modulus increases the critical stress for buckling and is expected to reduce or eliminate the buckling feature. During the strain process, both delamination onset and following propagation are suppressed with the increasing adhesion energy. After 100 strain cycles, the film that onto PDMS with 20 min UV/ozone treatment shows very subtle protrusions and stays a very low RMS roughness about 2nm compared with over 10nm for film onto neat PDMS. The local order of polymer is stable during the cyclic strain process and independent of UV/ozone treatment. In conclusion, UV/ozone surface treatment on PDMS substrate is an easy and promising method to achieve stretchable

organic semiconductor film onto soft substrate and may be potential to be applied on more than one polymer system.

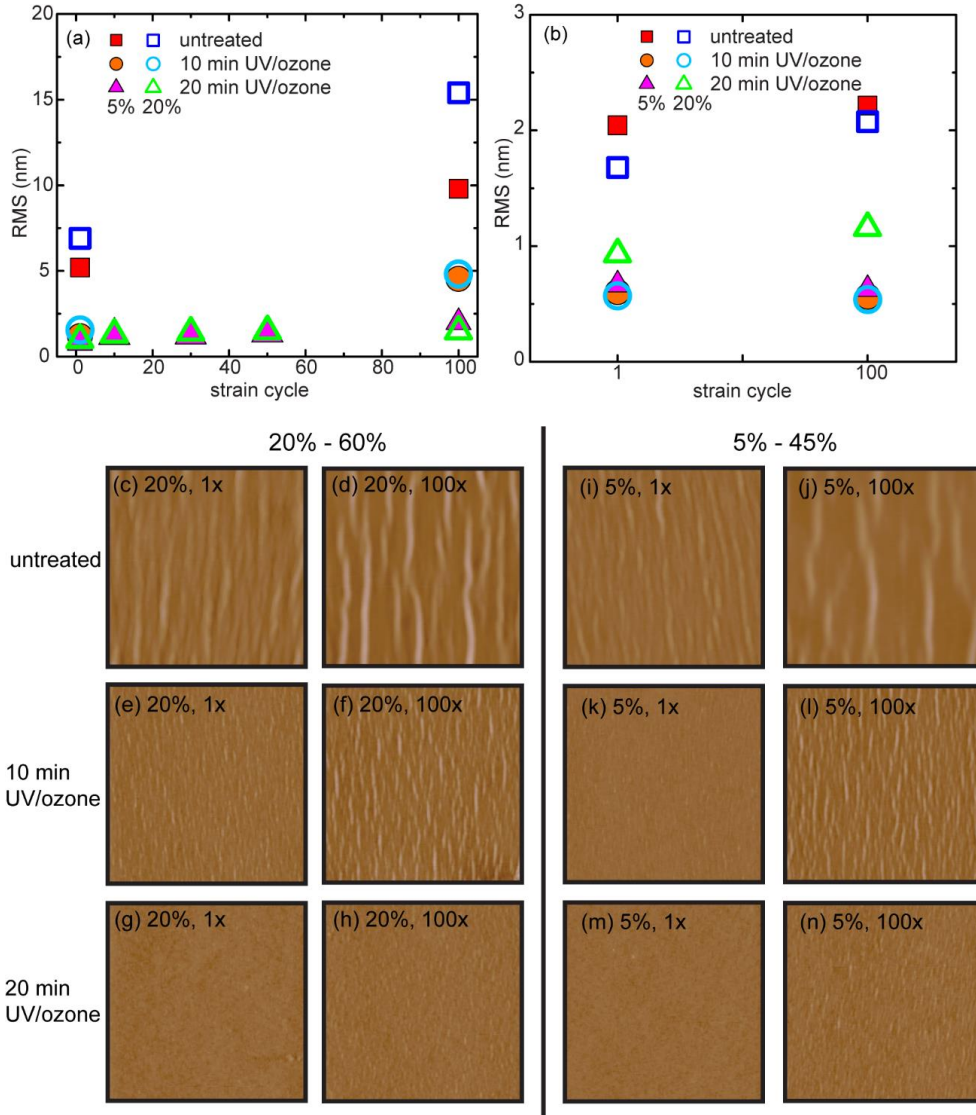


**Figure 53.** RMS roughness of films (a) being strained and (b) strain released during the cyclic strain process. AFM images films being strain released for two different strain ranges for 1 and 100 cycles onto PDMS with different treatment conditions are shown here. For strain range from 20% to 60%, AFM images are presented for films with (c) 1 cycle and (d) 100 cycles with normal PDMS, (e) 1 cycle and (f) 100 cycles with UV/ozone for 10 min, and (g) 1 cycle and (h) 100 cycles with UV/ozone for 20 min. For strain range from 5% to 45%, AFM images are presented for films with (i) 1 cycle and (j) 100 cycles with normal PDMS, (k) 1 cycle and (l) 100 cycles with UV/ozone for 10 min, and (m) 1 cycle and (n) 100 cycles with UV/ozone for 20 min.

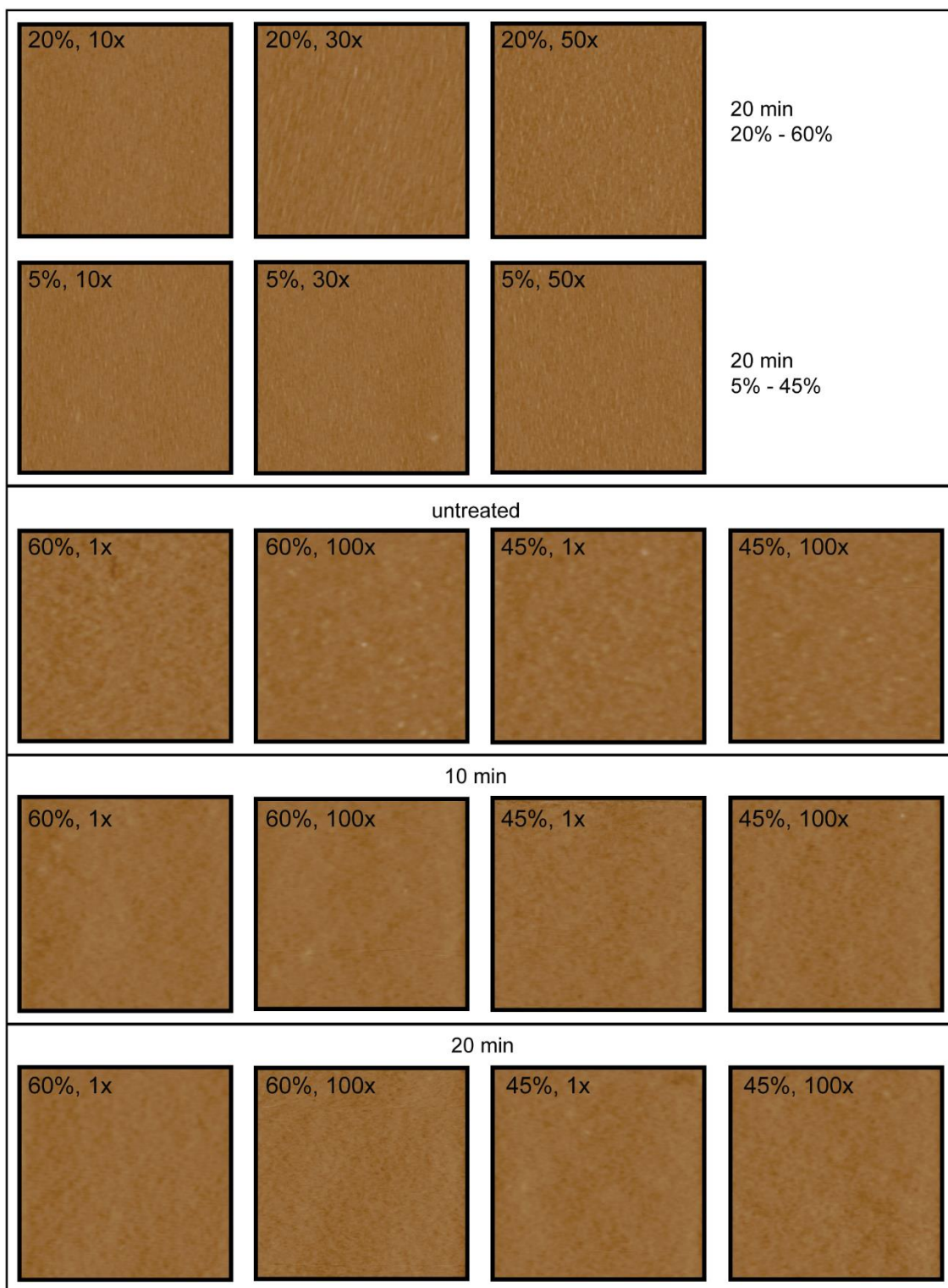


**Figure 54.** AFM images for films being strained and strain released for different cycles and different strain ranges onto PDMS with different UV/ozone treatment conditions.

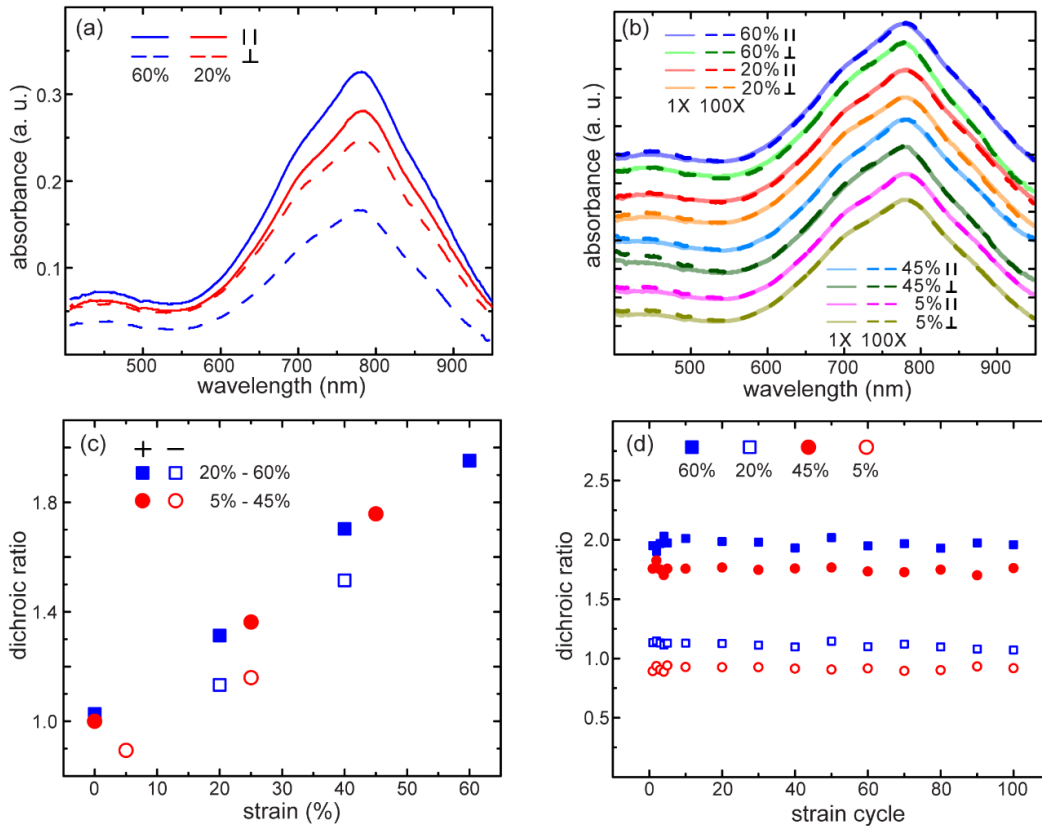


**Figure 55.** (a) Absorbance of DPP-4T film onto 20 min UV/ozone PDMS at 60% strain and film strained to 60% and then lowered to 20% under polarized light parallel ( $\parallel$ ) and perpendicular ( $\perp$ ) to the strain direction. (b) The normalized absorbance of the film onto 20 min UV/ozone PDMS substrate at 60% strain and at 20% strain for strain range of 20% - 60%, and of film at 45% strain and at 5% strain for strain range of 5% - 45%, comparing the first strain cycle (1x) to 100 cycles (100x). The measured absorbance at a specific strain state and polarized light orientation are normalized and offset for clarity. The absorbance at a specified strain state and light polarization during the first strain cycle and after 100 cycles are plotted together to compare absorbance features. (c) The dichroic ratio of the film onto 20 min UV/ozone PDMS substrate under tensile strain (+) and reduction of the applied strain (-) during the first strain cycle for strain range of 20% to 60% and 5% to 45%. The dichroic ratio is taken at 783 nm. (d) The dichroic ratio of the film onto 20 min UV/ozone PDMS substrate at 60% strain and 20% strain for 20% - 60% strain range and 45% strain and 5% strain for 5% - 45% strain range with increasing number of strain cycles.

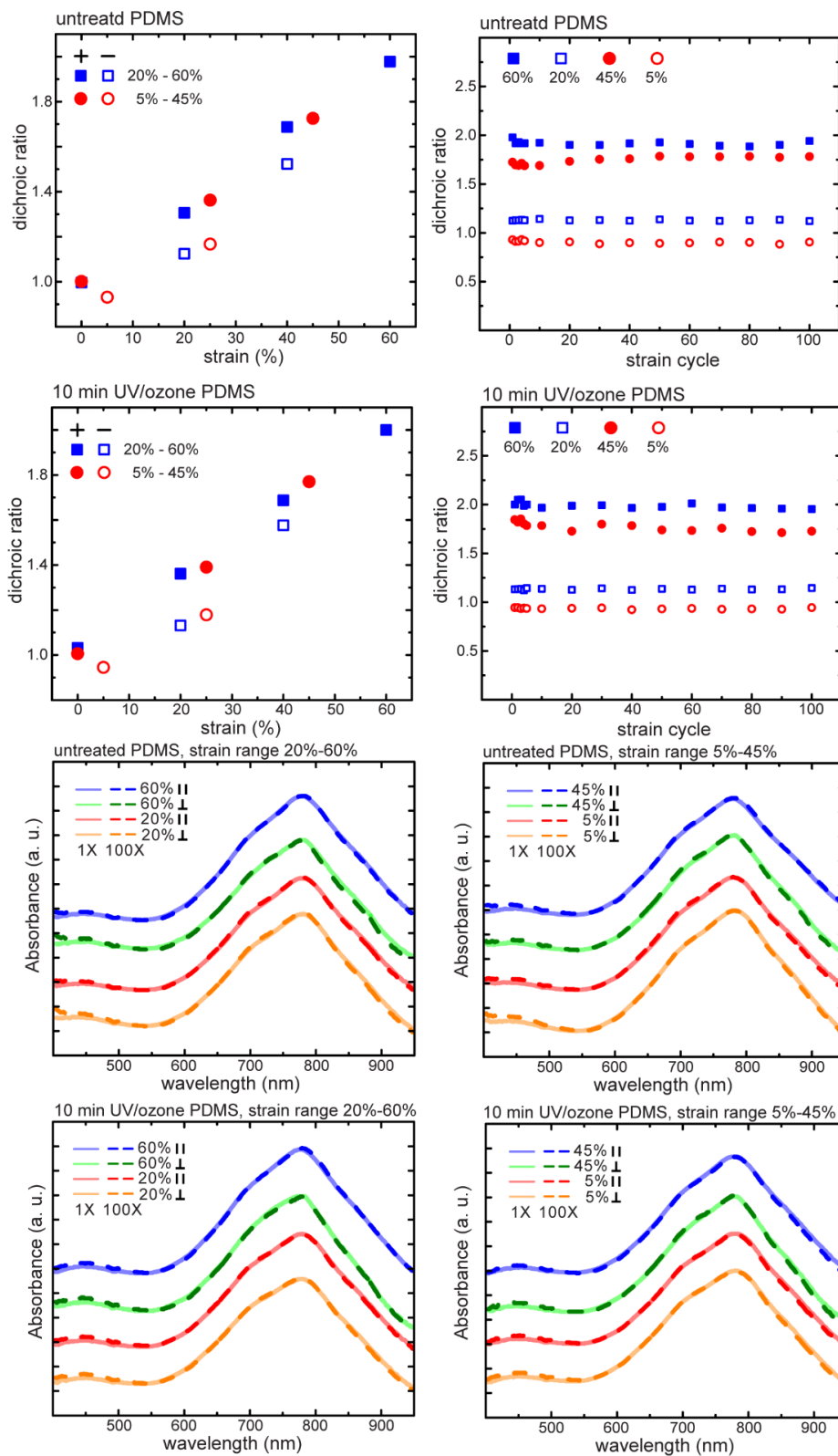


**Figure 56.** Normalized absorbance and dichroic ratio for films being strained and strain released for different cycles and different strain ranges onto PDMS with different UV/ozone treatment conditions.

#### 2.4.4 Experimental Section

**Film Processing:** The DPP4T film was cast from 3mg/ml and 8mg/ml solution dissolved in chloroform for 30nm and 150nm thick film respectively. The DPP-4T was purchased from Ossila, Ltd, with a number average molecular weight  $M_n = 76,226$  g/mol, a polydispersity of 2.45. The solution was spun cast onto OTS treated Si substrate at  $1500(2\pi)$  rad/min (1500 rpm) for 30 s at room temperature, followed by annealing at  $150^\circ\text{C}$  for 15 min. The films were then gradually cooled down in the glovebox. Then the films were transferred onto free standing PDMS slab for subsequent straining and morphological characterization. The strain process was done by motorized strain stage with the strain rate 5 %/s.

**PDMS processing:** The PDMS was Sylgard 184 and was prepared at 15:1 base to cross-linking ratio and cured in a vacuum oven held at  $\approx 85$  kPa at  $60^\circ\text{C}$  over a period of  $\approx 12$ h. The UV-Ozone treatment was done by placing free standing PDMS slab into cooled down UVO cleaner model No. 42 A from Jelight Company Inc for 10 or 20 min.

**Peeling test:** The peeling test was performed using an Instron 5943 tensile tester. The sample includes the DPP-4T thin onto PDMS slab, which is adhered to a glass substrate. A Scotch magic tape was laminated onto DPP-4T film surface and attached to the hands of tensile tester. Then a force was applied on the tape to delaminate DPP-4T film perpendicular from the PDMS substrate. The average applied load was then used to obtain the adhesion energy using Eqn. (24).

**AFM detection of yield point:** The polymer films were transferred to free standing PDMS slab as mentioned above. The polymer/PDMS was strained to a series strain and relaxed to 0%. AFM scan was performed each time when film was relaxed to 0%. The strain at which wrinkles started to show up is recorded as well as AFM images.

***Water floating determination of elastic region:*** The polymer films were first transferred to free standing PDMS slab and the original length was recorded. Then the PDMS together with polymer was strained for 50% using strain stage and length of strained polymer length was recorded. PSS thin film was cast onto clean glass slides from 1% solution in water at  $4000(2\pi)$  rad/min (4000 rpm), followed by dried at 100°C for 10min. Then the strained polymer film was transferred onto PSS/glass substrate. Water was added gently onto the polymer/PSS/glass sample. And then the floating polymer was picked up using a clean silicon substrate after about 5 min it floated on the water allowing for the shrinkage to happen. The final length of polymer was recorded and the shrinkage percent could be calculated.

***Morphology Characterization:*** UV-visible spectroscopy measurements were made using an Ocean Optics Jazz spectrometer. The absorbance of the films was measured while on a PDMS substrate and measured at multiple strain states. The AFM images were measured using an Asylum MFP-3D-BIO in tapping mode. The measurement was made with film onto PDMS substrate.

## 2.5 Summary and potential future work

### 2.5.1 Summary for present work

We introduce two efficient approaches to improve the stretchability of organic semiconductor polymers. Blending a rigid but functional polymer of PCDTPT with another more ductile polymer P3HT that possesses superior plasticity under both straining and strain-releasing condition. The electrical property of blend is comparable with neat PCDTPT due to the vertical aggregation. A reversible dichroic ratio during strain and strain release process indicate a reversible morphology. And during the cyclic strain, this reversible morphology is also maintained. Besides, the local packing order of the polymers is shown to be remarkably stable. The saturated field effect charge mobility is shown to be consistently above  $0.04 \text{ cm}^2/\text{Vs}$ . The film showed no signs of fracture for strains up to 75% for 100 cycles, but start to show delamination when strain is released to 10% for large strain cycles.

To reduce the delamination, we moderately treat the PDMS substrate with UV/ozone before printed with thin film polymer semiconductor, which we choose DPP-4T here. The surface layer PDMS under UV/ozone becomes more hydrophilic with higher surface energy, and the mechanical property is also changed. The surface treatment increases the adhesion energy between PDMS substrate and the DPP-4T film, and at the same time reduces the modulus mismatch between these two. After UV/ozone treatment, the wrinkling onset strain is greatly improved from 17% to 47%. And during the cyclic strain, the RMS roughness is shown to be consistently below 2 nm for up to 100 strain cycles with range from 5% to 45% as well as from 20% to 60%, with a stable local packing order of the polymer. This work points out the importance of adhesion energy between two layers and may suggest a potential approach for future stretchable electronics.

## 2.5.2 Suggestion for future work

Blending is an effective method to change the mechanical property of material. Our work used a ratio of 4:6 between PCDTPT and P3HT. A future research direction in optimizing the ratio of the two components may lead to a better performance. A combination of blend and surface treatment may also worth to explore. For surface treatment method, we only characterized the morphology during the cyclic strain and didn't characterize the charge carrier mobility because the film cannot be transferred to OTS treated transistor test bed from UV/ozone treated PDMS. Further exploration for mobility measurement can provide more information about the film resistance during cyclic strain when has a strong bonding with substrate. A possible way to measure the charge carrier mobility is to laminate the film together with PDMS substrate onto transistor test bed, as shown in **Figure 56**<sup>125,158</sup>.

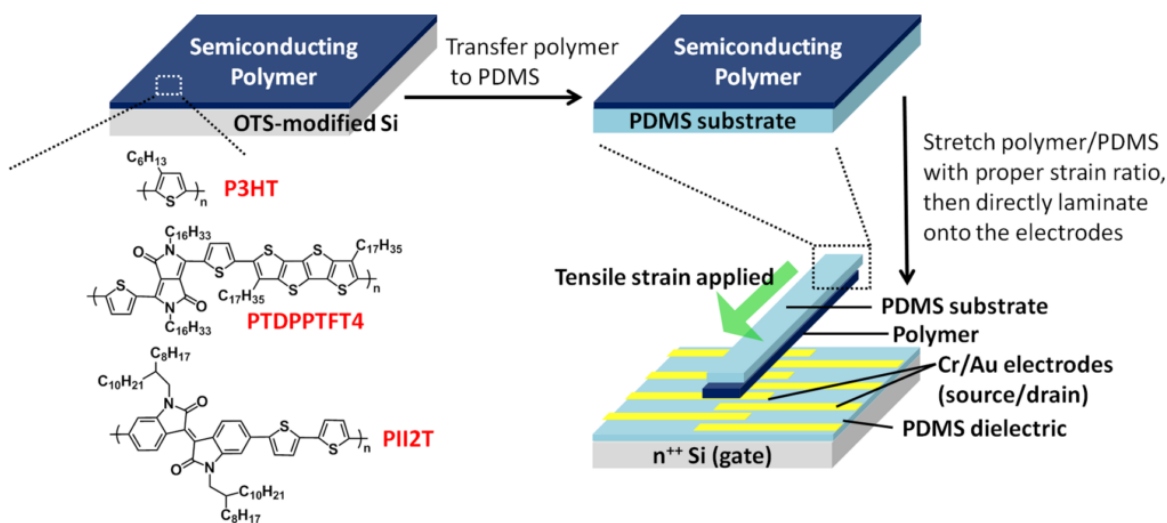


**Figure 57.** Schematic illustration of lamination method used to evaluate semiconducting polymers for stretchable electronics<sup>158</sup>.

The polymer usually possesses viscoelasticity, which cause the polymer not able to respond to the stimulus immediately. Therefore, in the dynamic measurement like cyclic

strain process, the strain rate may have a very important effect on the polymer's behavior. Future research to study the strain rate's effect on the stretchability of the film may offer more information about the effect of film's viscoelasticity on the stretchability.

We show that the stretchability of DPP-4T film onto UV/ozone treated PDMS has been greatly improved. It would be helpful to do the same measurement on other polymer systems to confirm this is a universal method instead of only be specific on DPP-4T. The potential new polymer system could be ductile polymer like P3HT that can be strained to 90% or 100% without showing crack. It would also be interesting to use some more rigid polymer like DPP-TT or N2200 to show the surface treatment's effect on the crack onset.

## REFERENCES

1. U.S. Energy Information Administration. *International Energy Outlook 2016*. *International Energy Outlook 2016* **0484(2016)**, (2016).
2. Lawrence Livermore National Laboratory. The 2015 energy flow chart. (2016).
3. Gingerich, D. & Mauter, M. Quantity, Quality, and Availability of Residual Heat from United States Thermal Power Generation. *Environ. Sci. Technol.* **49**, 8297–8306 (2015).
4. Rattner, A. S. & Garimella, S. Energy harvesting, reuse and upgrade to reduce primary energy usage in the USA. *Energy* **36**, 6172–6183 (2011).
5. Hosford Goldsmid. *Introduction to Thermoelectricity*. (2013).
6. [egr.msu.edu/morelli-research/thermoelectrics](http://egr.msu.edu/morelli-research/thermoelectrics).
7. Heremans, J. P., Dresselhaus, M. S., Bell, L. E. & Morelli, D. T. When thermoelectrics reached the nanoscale. *Nat. Nanotechnol.* **8**, 471–473 (2013).
8. Rull-Bravo, M., Moure, A., Fernández, J. F. & Martín-González, M. Skutterudites as thermoelectric material: revisited. *Optoelectron. Adv. Mater. Rapid Commun.* **4**, 1166–1169 (2010).
9. Chung, D.-Y. *et al.* A New Thermoelectric Material: CsBi<sub>4</sub>Te<sub>6</sub>. *JACS* **126**, 6414–6428 (2004).
10. Caillat, T. *et al.* Progress in the development of high efficiency segmented thermoelectric generators. *Sp. Technol. Appl. Int. Forum* **458**, 1403 (1999).
11. Snyder, G. J. Application of the compatibility factor to the design of segmented and cascaded thermoelectric generators. *Appl. Phys. Lett.* **84**, 2436–2438 (2004).
12. Cook, B. a. *et al.* High-Performance Three-Stage Cascade Thermoelectric Devices with 20% Efficiency. *J. Electron. Mater.* **44**, 1936–1942 (2015).
13. Huang, I. Y. *et al.* Development of low-cost micro-thermoelectric coolers utilizing MEMS technology. *Sensors Actuators, A Phys.* **148**, 176–185 (2008).
14. Bae, S. *et al.* 30 inch Roll-Based Production of High-Quality Graphene Films for Flexible Transparent Electrodes. **5**, 1–5 (2009).
15. Zhang, Z., Qiu, J. & Wang, S. Roll-to-roll printing of flexible thin-film organic thermoelectric devices. *Manuf. Lett.* **8**, 6–10 (2016).
16. Venkatasubramanian, R., Siivola, E., Colpitts, T. & O’Quinn, B. Thin-film thermoelectric devices with high room-temperature figures of merit. *Nature* **413**, 597–602 (2001).
17. Tang, G. H., Zhao, Y., Zhai, G. X. & Bi, C. Phonon boundary scattering effect on thermal conductivity of thin films. *J. Appl. Phys.* **110**, 1–4 (2011).

18. Kim, G.-H., Shao, L., Zhang, K. & Pipe, K. P. Engineered doping of organic semiconductors for enhanced thermoelectric efficiency. *Nat. Mater.* **12**, 719–23 (2013).
19. Rowe, D. *CRC handbook of thermoelectrics*. (1995).
20. Chen, G., Dresselhaus, M. S., Dresselhaus, G., Fleurial, J.-P. & Caillat, T. Recent developments in thermoelectric materials. *Int. Mater. Rev.* **48**, 45–66 (2003).
21. Shakouri, A. Recent Developments in Semiconductor Thermoelectric Physics and Materials. *Annu. Rev. Mater. Res.* **41**, 399–431 (2011).
22. LeBlanc, S., Yee, S. K., Scullin, M. L., Dames, C. & Goodson, K. E. Material and manufacturing cost considerations for thermoelectrics. *Renew. Sustain. Energy Rev.* **32**, 313–327 (2014).
23. Malen, J. a., Yee, S. K., Majumdar, A. & Segalman, R. a. Fundamentals of energy transport, energy conversion, and thermal properties in organic–inorganic heterojunctions. *Chem. Phys. Lett.* **491**, 109–122 (2010).
24. See, K. C. *et al.* Water-processable polymer-nanocrystal hybrids for thermoelectrics. *Nano Lett.* **10**, 4664–7 (2010).
25. Yazawa, K. & Shakouri, A. Cost-efficiency trade-off and the design of thermoelectric power generators. *Environ. Sci. Technol.* **45**, 7548–53 (2011).
26. Kim, R., Datta, S. & Lundstrom, M. S. Influence of dimensionality on thermoelectric device performance. *J. Appl. Phys.* **105**, 34506 (2009).
27. Mayer, P. M. & Ram, R. J. Optimization of Heat Sink–Limited Thermoelectric Generators. *Nanoscale Microscale Thermophys. Eng.* **10**, 143–155 (2006).
28. Navone, C., Soulier, M., Plissonnier, M. & Seiler, a. L. Development of ( Bi , Sb ) 2 ( Te , Se ) 3 -Based Thermoelectric Modules by a Screen-Printing Process. *J. Electron. Mater.* **39**, 1755–1759 (2010).
29. Kim, S. J., We, J. H., Kim, J. S., Kim, G. S. & Cho, B. J. Thermoelectric properties of P-type Sb<sub>2</sub>Te<sub>3</sub> thick film processed by a screen-printing technique and a subsequent annealing process. *J. Alloys Compd.* **582**, 177–180 (2014).
30. We, J. H., Kim, S. J., Kim, G. S. & Cho, B. J. Improvement of thermoelectric properties of screen-printed Bi<sub>2</sub>Te<sub>3</sub> thick film by optimization of the annealing process. *J. Alloys Compd.* **552**, 107–110 (2013).
31. Budak, S. *et al.* Thermoelectric properties of SiO<sub>2</sub>/SiO<sub>2</sub>+CoSb multi-nanolayered thin films modified by MeV Si ions. *J. Intell. Mater. Syst. Struct.* **24**, 1350–1356 (2012).
32. Lee, H.-B. *et al.* Thin-Film Thermoelectric Module for Power Generator Applications Using a Screen-Printing Method. *J. Electron. Mater.* **40**, 615–619 (2011).
33. Madan, D., Wang, Z. & Chen, A. High-Performance Dispenser Printed MA p-Type Bi<sub>0.5</sub>Sb<sub>1.5</sub>Te<sub>3</sub> Flexible Thermoelectric Generators for Powering Wireless Sensor Networks. *ACS Appl. Mater. ...* (2013).

34. Fan, P. *et al.* The high performance of a thin film thermoelectric generator with heat flow running parallel to film surface. *Appl. Phys. Lett.* **102**, 33904 (2013).
35. Wüsten, J. & Potje-Kamloth, K. Organic thermogenerators for energy autarkic systems on flexible substrates. *J. Phys. D. Appl. Phys.* **41**, 135113 (2008).
36. Bubnova, O. & Crispin, X. Towards polymer-based organic thermoelectric generators. *Energy Environ. Sci.* **5**, 9345 (2012).
37. Kim, H., Park, S.-G., Jung, B., Hwang, J. & Kim, W. New device architecture of a thermoelectric energy conversion for recovering low-quality heat. *Appl. Phys. A* **114**, 1201–1208 (2013).
38. Itoigawa, K., Ueno, H., Shiozaki, M., Toriyama, T. & Sugiyama, S. Fabrication of flexible thermopile generator. *J. Micromechanics Microengineering* **15**, S233–S238 (2005).
39. Francioso, L. & Pascali, C. De. Thin film technology flexible thermoelectric generator and dedicated ASIC for energy harvesting applications. *Adv. Sensors ...* 216–219 (2013).
40. Shelby, M. & Clear, S. Self-corrugating laminates and methods of making them. *US Pat. App. 13/965,288*
41. Yadav, A., Pipe, K. P. & Shtein, M. Fiber-based flexible thermoelectric power generator. *J. Power Sources* **175**, 909–913 (2008).
42. Maréchal, N. Characterization of silver films deposited by radio frequency magnetron sputtering. *J. Vac. Sci. Technol. A Vacuum, Surfaces, Film.* **12**, 707 (1994).
43. Gergen, B., Nienhaus, H., Weinberg, W. H. & McFarland, E. M. Morphological investigation of ultrathin Ag and Ti films grown on hydrogen terminated Si(111). *J. Vac. Sci. Technol. B Microelectron. Nanom. Struct.* **18**, 2401 (2000).
44. Gray, D. American institute of physics handbook. (1982).
45. Paddock, C. a. & Eesley, G. L. Transient thermoreflectance from thin metal films. *J. Appl. Phys.* **60**, 285 (1986).
46. Logeeswaran Vj *et al.* Ultrasmooth silver thin films deposited with a germanium nucleation layer. *Nano Lett.* **9**, 178–82 (2009).
47. Parker, R. L. & Krinsky, a. Electrical resistance-strain characteristics of thin evaporated metal films. *J. Appl. Phys.* **34**, 2700–2708 (1963).
48. Antonova, E. & Looman, D. Finite elements for thermoelectric device analysis in ANSYS. *Thermoelectr. 2005. ICT 2005. ...* (2005).
49. Owoyele, O., Ferguson, S. & O'Connor, B. T. Performance analysis of a thermoelectric cooler with a corrugated architecture. *Appl. Energy* **147**, 184–191 (2015).
50. Rowe, D. & Min, G. Evaluation of thermoelectric modules for power generation. *J.*

*Power Sources* **73**, 193–198 (1998).

51. Song, S., Au, V. & Moran, K. Constriction/spreading resistance model for electronics packaging. *Proc. 4th ASME/JSME Therm. ...* **4**, 199–206 (1995).
52. Song, S., Lee, S. & Au, V. Closed-form equation for thermal constriction/spreading resistances with variable resistance boundary condition. *IEPS Conf.* 111–121 (1994).
53. Incropera, F. *Introduction to heat transfer.* (2011).
54. Shiozaki, M. S. M., Sugiyama, S. S. S., Watanabe, N. W. N., Ueno, H. U. H. & Itoigawa, K. I. K. Flexible Thin-Film BiTe Thermopile for Room Temperature Power Generation. *19th IEEE Int. Conf. Micro Electro Mech. Syst.* 946–949 (2006). doi:10.1109/MEMSYS.2006.1627957
55. Kim, G.-H., Shao, L., Zhang, K. & Pipe, K. P. Engineered doping of organic semiconductors for enhanced thermoelectric efficiency. *Nat. Mater.* **12**, 719–23 (2013).
56. Riffat, S. B. & Ma, X. Thermoelectrics: A review of present and potential applications. *Appl. Therm. Eng.* **23**, 913–935 (2003).
57. Zheng, X. F., Liu, C. X., Yan, Y. Y. & Wang, Q. A review of thermoelectrics research - Recent developments and potentials for sustainable and renewable energy applications. *Renew. Sustain. Energy Rev.* **32**, 486–503 (2014).
58. Chau, K. T. & Chan, C. C. Emerging energy-efficient technologies for hybrid electric vehicles. *Proc. IEEE* **95**, 821–835 (2007).
59. Kraemer, D. *et al.* Photovoltaic-thermoelectric hybrid systems: A general optimization methodology. *Appl. Phys. Lett.* **92**, (2008).
60. Sark, W. G. J. H. M. van. Feasibility of photovoltaic - Thermoelectric hybrid modules. *Appl. Energy* **88**, 2785–2790 (2011).
61. Vorobiev, Y., Gonzalez-Hernandez, J., Vorobiev, P. & Bulat, L. Thermal-photovoltaic solar hybrid system for efficient solar energy conversion. *Sol. Energy* **80**, 170–176 (2006).
62. Wang, N., Han, L., He, H., Park, N.-H. & Koumoto, K. A novel high-performance photovoltaic–thermoelectric hybrid device. *Energy Environ. Sci.* **4**, 3676 (2011).
63. Yang, D. & Yin, H. Energy conversion efficiency of a novel hybrid solar system for photovoltaic, thermoelectric, and heat utilization. *IEEE Trans. Energy Convers.* **26**, 662–670 (2011).
64. Yang, J. & Stabler, F. R. Automotive applications of thermoelectric materials. *J. Electron. Mater.* **38**, 1245–1251 (2009).
65. Bell, L. E. Cooling, heating, generating power, and recovering waste heat with thermoelectric systems. *Science* **321**, 1457–1461 (2008).
66. Ikoma, K. *et al.* Thermoelectric module and generator for gasoline engine vehicles.

*Seventeenth Int. Conf. Thermoelectr. Proc. ICT98 (Cat. No.98TH8365)* 5–8 (1998).  
doi:10.1109/ICT.1998.740419

67. Kim, M.-K., Kim, M.-S., Lee, S., Kim, C. & Kim, Y.-J. Wearable thermoelectric generator for harvesting human body heat energy. *Smart Mater. Struct.* **23**, 105002 (2014).
68. Wang, Z., Leonov, V., Fiorini, P. & Van Hoof, C. Realization of a wearable miniaturized thermoelectric generator for human body applications. *Sensors Actuators, A Phys.* **156**, 95–102 (2009).
69. Suarez, F. *et al.* Designing thermoelectric generators for self-powered wearable electronics. *Energy Environ. Sci.* **9**, 2099–2113 (2016).
70. Lee, J. A. *et al.* Woven-Yarn Thermoelectric Textiles. *Adv. Mater.* 1–7 (2016).  
doi:10.1002/adma.201600709
71. Kim, S. J., We, J. H. & Cho, B. J. A wearable thermoelectric generator fabricated on a glass fabric. *Energy Environ. Sci.* **7**, 1959 (2014).
72. Jo, S. E., Kim, M. K., Kim, M. S. & Kim, Y. J. Flexible thermoelectric generator for human body heat energy harvesting. *Electron. Lett.* **48**, 1015 (2012).
73. Hyland, M., Hunter, H., Liu, J., Veety, E. & Vashaee, D. Wearable thermoelectric generators for human body heat harvesting. *Appl. Energy* **182**, 518–524 (2016).
74. Bahk, J.-H., Fang, H., Yazawa, K. & Shakouri, A. Flexible thermoelectric materials and device optimization for wearable energy harvesting. *J. Mater. Chem. C* **3**, 10362–10374 (2015).
75. Liang, D. X., Yang, H. R., Finefrock, S. W. & Wu, Y. Flexible Nanocrystal-Coated Glass Fibers for High-Performance Thermoelectric Energy Harvesting. *Nano Lett* **12**, 2140–2145 (2012).
76. Lu, M., Mok, L. & Bezama, R. J. A Graphite Foams Based Vapor Chamber for Chip Heat Spreading. *J. Electron. Packag.* **128**, 427 (2006).
77. Seelmann-Eggebert, M. *et al.* Heat-spreading diamond films for GaN-based high-power transistor devices. *Diam. Relat. Mater.* **10**, 744–749 (2001).
78. Zhou, Y., Paul, S. & Bhunia, S. Harvesting wasted heat in a microprocessor using thermoelectric generators: Modeling, analysis and measurement. *Proc. -Design, Autom. Test Eur. DATE* 98–103 (2008). doi:10.1109/DATE.2008.4484669
79. Sun, T., Peavey, J. L., David Shelby, M., Ferguson, S. & O'Connor, B. T. Heat shrink formation of a corrugated thin film thermoelectric generator. *Energy Convers. Manag.* **103**, 674–680 (2015).
80. Antonik, M. Performance and Design Comparison of a Bulk Thermoelectric Cooler with a Hybrid Device Architecture. **8**, 1–13 (2016).
81. Zhang, Y. *et al.* A Batteryless 19 uW MICS/ISM-Band Energy Harvesting Body Sensor Node SoC for ExG Applications. *Solid-State Circuits, IEEE J.* **48**, 199–213

(2013).

82. Misra, V. *et al.* Flexible Technologies for Self-Powered Wearable Health and Environmental Sensing. *Proc. IEEE* **103**, 665–681 (2015).
83. Sabetzadeh, N., Bahrambeygi, H., Rabbi, a. & Nasouri, K. Thermal conductivity of polyacrylonitrile nanofibre web in various nanofibre diameters and surface densities. *Micro Nano Lett.* **7**, 662 (2012).
84. Yovanovich, M. M., Culham, J. R. & Teertstra, P. Calculating interface resistance. *Electron. Cool.* 1–9 (1997). doi:[http://www.mhtlab.uwaterloo.ca/pdf\\_papers/mhtl97-4.pdf](http://www.mhtlab.uwaterloo.ca/pdf_papers/mhtl97-4.pdf)
85. Cohen, M. L. Measurement of the Thermal Properties of Human Skin. a Review. *Journal of Investigative Dermatology* **69**, 333–338 (1977).
86. Lizák, P. & Mojumdar, S. C. Thermal properties of textile fabrics. *J. Therm. Anal. Calorim.* **112**, 1095–1100 (2013).
87. Talley, L. D. *i • • x I x x.* **101**, 161–163 (1996).
88. [nobelprize.org/nobel\\_prizes/chemistry/laureates/2000](http://nobelprize.org/nobel_prizes/chemistry/laureates/2000).
89. Shirakawa, H., Louis, J. & Macdiarmid, A. G. Synthesis of Electrically Conducting Organic Polymers : Halogene Derivatives of Polyacetylene, (CH)<sub>x</sub>. *J. C. S. Chem. Comm* 578–580 (1977). doi:10.1039/C39770000578
90. Keum, H., McCormick, M., Liu, P., Zhang, Y. & Omenetto, F. G. Epidermal Electronics. *Science (80-. )*. **333**, (2011).
91. Ren, K., Liu, S., Lin, M., Wang, Y. & Zhang, Q. M. A compact electroactive polymer actuator suitable for refreshable Braille display. *Sensors Actuators, A Phys.* **143**, 335–342 (2008).
92. Shabani Shayeh, J., Ehsani, A., Ganjali, M. R., Norouzi, P. & Jaleh, B. Conductive polymer/reduced graphene oxide/Au nano particles as efficient composite materials in electrochemical supercapacitors. *Appl. Surf. Sci.* **353**, 594–599 (2015).
93. Kim, W. H. *et al.* Molecular organic light-emitting diodes using highly conducting polymers as anodes. *Appl. Phys. Lett.* **80**, 3844–3846 (2002).
94. Wakim, S. *et al.* Highly efficient organic solar cells based on a poly(2,7-carbazole) derivative. *J. Mater. Chem.* **19**, 5351 (2009).
95. Meier, R., Birkenstock, C., Palumbiny, C. M. & Müller-Buschbaum, P. Efficiency-improved organic solar cells based on plasticizer assisted soft embossed PEDOT:PSS layers. *Phys. Chem. Chem. Phys.* **14**, 15088 (2012).
96. Lipomi, D. J., Tee, B. C.-K., Vosgueritchian, M. & Bao, Z. Stretchable organic solar cells. *Adv. Mater.* **23**, 1771–5 (2011).
97. Jung, Y. S., Jung, W., Tuller, H. L. & Ross, C. A. Nanowire Conductive Polymer Gas Sensor Patterned Using Self-Assembled Block Copolymer Lithography. 25–27 (2008).

98. Cochrane, C., Koncar, V., Lewandowski, M. & Dufour, C. Design and Development of a Flexible Strain Sensor for Textile Structures Based on a Conductive Polymer Composite. *Sensors* **7**, 473–492 (2007).
99. Nambiar, S. & Yeow, J. T. W. Conductive polymer-based sensors for biomedical applications. *Biosens. Bioelectron.* **26**, 1825–1832 (2011).
100. Krebs, F. C. All solution roll-to-roll processed polymer solar cells free from indium-tin-oxide and vacuum coating steps. *Org. Electron. physics, Mater. Appl.* **10**, 761–768 (2009).
101. Kim, D.-H. *et al.* Materials and noncoplanar mesh designs for integrated circuits with linear elastic responses to extreme mechanical deformations. *Proc. Natl. Acad. Sci. U. S. A.* **105**, 18675–80 (2008).
102. Menard, E., Lee, K. J., Khang, D. Y., Nuzzo, R. G. & Rogers, J. A. A printable form of silicon for high performance thin film transistors on plastic substrates. *Appl. Phys. Lett.* **84**, 5398–5400 (2004).
103. Choi, W. M., Song, J., Khang, D. & Jiang, H. Biaxially stretchable wavy silicon nanomembranes.pdf. (2007).
104. Khang, D.-Y., Jiang, H., Huang, Y. & Rogers, J. A. A Stretchable Form of Single-Crystal. *Science (80-. )*. **311**, 208–212 (2006).
105. Li, J. *et al.* A stable solution-processed polymer semiconductor with record high-mobility for printed transistors. *Sci. Rep.* **2**, 754 (2012).
106. Sirringhaus, H. Device physics of solution-processed organic field-effect transistors. *Adv. Mater.* **17**, 2411–2425 (2005).
107. Peng, R. *et al.* An ABA triblock copolymer strategy for intrinsically stretchable semiconductors †. *J. Mater. Chem. C* **3**, 3599–3606 (2015).
108. Printz, A. D. & Lipomi, D. J. Competition between Deformability and Charge Transport in Semiconducting Polymers for Flexible and Stretchable Electronics. *Appl. Phys. Rev.* **3**, 21302 (2016).
109. O'Connor, B. *et al.* Correlations between mechanical and electrical properties of polythiophenes. *ACS Nano* **4**, 7538–7544 (2010).
110. Son, S. Y. *et al.* High-Field-Effect Mobility of Low-Crystallinity Conjugated Polymers with Localized Aggregates. *J. Am. Chem. Soc.* **138**, 8096–8103 (2016).
111. Sun, T. *et al.* Plastic Deformation of Polymer Blends as a Means to Achieve Stretchable Organic Transistors. *Adv. Electron. Mater.* **201600388**, 1600388 (2016).
112. Xu, J. *et al.* Highly stretchable polymer semiconductor films through the nanoconfinement effect. *Science (80-. )*. (2017).
113. Choi, D. *et al.* Elastomer-Polymer Semiconductor Blends for High-Performance Stretchable Charge Transport Networks. *Chem. Mater.* **28**, 1196–1204 (2016).

114. Müller, C. *et al.* Tough, semiconducting polyethylene-poly(3-hexylthiophene) diblock copolymers. *Adv. Funct. Mater.* **17**, 2674–2679 (2007).
115. Shin, M. *et al.* Polythiophene nanofibril bundles surface-embedded in elastomer: A route to a highly stretchable active channel layer. *Adv. Mater.* **27**, 1255–1261 (2015).
116. Qiu, L. *et al.* Organic thin-film transistors based on polythiophene nanowires embedded in insulating polymer. *Adv. Mater.* **21**, 1349–1353 (2009).
117. Scott, J. I. *et al.* Significantly Increasing the Ductility of High Performance Polymer Semiconductors through Polymer Blending. *ACS Appl. Mater. Interfaces* acsami.6b01852 (2016). doi:10.1021/acsami.6b01852
118. Savagatrup, S. *et al.* Plasticization of PEDOT:PSS by Common Additives for Mechanically Robust Organic Solar Cells and Wearable Sensors. *Adv. Funct. Mater.* **25**, 427–436 (2015).
119. Oh, J. Y., Kim, S., Baik, H. K. & Jeong, U. Conducting Polymer Dough for Deformable Electronics. *Adv. Mater.* (2015). doi:10.1002/adma.201502947
120. Vosgueritchian, M., Lipomi, D. J. & Bao, Z. Highly conductive and transparent PEDOT:PSS films with a fluorosurfactant for stretchable and flexible transparent electrodes. *Adv. Funct. Mater.* **22**, 421–428 (2012).
121. Ichikawa, S. & Toshima, N. Improvement of thermoelectric properties of composite films of PEDOT-PSS with xylitol by means of stretching and solvent treatment. *Polym. J.* **47**, 522–526 (2015).
122. Wei, Q., Mukaida, M., Naitoh, Y. & Ishida, T. Morphological change and mobility enhancement in PEDOT:PSS by adding co-solvents. *Adv. Mater.* **25**, 2831–2836 (2013).
123. Savagatrup, S. *et al.* Viability of stretchable poly(3-heptylthiophene) (P3HpT) for organic solar cells and field-effect transistors. *Synth. Met.* **203**, 208–214 (2015).
124. Savagatrup, S., Makaram, A. S., Burke, D. J. & Lipomi, D. J. Mechanical properties of conjugated polymers and polymer-fullerene composites as a function of molecular structure. *Adv. Funct. Mater.* **24**, 1169–1181 (2014).
125. Lu, C. *et al.* Effects of Molecular Structure and Packing Order on the Stretchability of Semicrystalline Conjugated Poly(Tetrathienoacene-diketopyrrolopyrrole) Polymers. *Adv. Electron. Mater.* **201600311**, 1600311 (2016).
126. Savagatrup, S., Printz, A. D., Rodriguez, D. & Lipomi, D. J. Best of both worlds: Conjugated polymers exhibiting good photovoltaic behavior and high tensile elasticity. *Macromolecules* **47**, 1981–1992 (2014).
127. Jin, Y. J. *et al.* Room temperature fluorescent conjugated polymer gums. *Adv. Funct. Mater.* **24**, 1928–1937 (2014).
128. O'Connor, B. T. *et al.* Morphological origin of charge transport anisotropy in aligned polythiophene thin films. *Adv. Funct. Mater.* **24**, 3422–3431 (2014).

129. teachers.stanford.edu/activities/SPMReference/.
130. Smith, J. *et al.* Solution-processed organic transistors based on semiconducting blends. *J. Mater. Chem.* **20**, 2562 (2010).
131. Newman, C. R. *et al.* Introduction to Organic Thin Film Transistors and Design of n-Channel Organic Semiconductors. *Chem. Mater.* **16**, 2236–4451 (2004).
132. Song, E. *et al.* Stretchable and Transparent Organic Semiconducting Thin Film with Conjugated Polymer Nanowires Embedded in an Elastomeric Matrix. *Adv. Electron. Mater.* **2**, n/a-n/a (2016).
133. Hammock, M. L., Chortos, A., Tee, B. C. K., Tok, J. B. H. & Bao, Z. 25th anniversary article: The evolution of electronic skin (E-Skin): A brief history, design considerations, and recent progress. *Adv. Mater.* **25**, 5997–6038 (2013).
134. Kaltenbrunner, M. *et al.* Ultrathin and lightweight organic solar cells with high flexibility. *Nat. Commun.* **3**, 770 (2012).
135. Wang, J., Yan, C., Chee, K. J. & Lee, P. S. Highly stretchable and self-deformable alternating current electroluminescent devices. *Adv. Mater.* **27**, 2876–2882 (2015).
136. Liang, J., Li, L., Niu, X., Yu, Z. & Pei, Q. Elastomeric polymer light-emitting devices and displays. *Nat. Photonics* **7**, 817–824 (2013).
137. Park, J. *et al.* Giant tunneling piezoresistance of composite elastomers with interlocked microdome arrays for ultrasensitive and multimodal electronic skins. *ACS Nano* **8**, 4689–4697 (2014).
138. Lee, Y., Shin, M., Thiyagarajan, K. & Jeong, U. Approaches to Stretchable Polymer Active Channels for Deformable Transistors. *Macromolecules* acs.macromol.5b02268 (2015). doi:10.1021/acs.macromol.5b02268
139. Chortos, A. *et al.* Highly stretchable transistors using a microcracked organic semiconductor. *Adv. Mater.* **26**, 4253–4259 (2014).
140. Kim, D. H., Xiao, J., Song, J., Huang, Y. & Rogers, J. A. Stretchable, curvilinear electronics based on inorganic materials. *Adv. Mater.* **22**, 2108–2124 (2010).
141. Liang, J. *et al.* Intrinsically stretchable and transparent thin-film transistors based on printable silver nanowires, carbon nanotubes and an elastomeric dielectric. *Nat. Commun.* **6**, 7647 (2015).
142. R. J. Young, P. A. L. *Introduction to Polymers.* (CRC Press, 2011).
143. Wang, G.-J. N. *et al.* Inducing Elasticity through Oligo-Siloxane Crosslinks for Intrinsically Stretchable Semiconducting Polymers. *Adv. Funct. Mater.* 7254–7262 (2016). doi:10.1002/adfm.201602603
144. Printz, A. D., Savagatrup, S., Burke, D. J., Purdy, T. N. & Lipomi, D. J. Increased elasticity of a low-bandgap conjugated copolymer by random segmentation for mechanically robust solar cells. *RSC Adv.* **4**, 13635–13643 (2014).

145. Savagatrup, S., Printz, A. D., O'Connor, T. F., Zaretski, A. V. & Lipomi, D. J. Molecularly stretchable electronics. *Chem. Mater.* **26**, 3028–3041 (2014).
146. Awartani, O. *et al.* Correlating stiffness, ductility, and morphology of polymer:Fullerene films for solar cell applications. *Adv. Energy Mater.* **3**, 399–406 (2013).
147. Scaccabarozzi, A. D. & Stingelin, N. Semiconducting:insulating polymer blends for optoelectronic applications-a review of recent advances. *J. Mater. Chem. A* **2**, 10818–10824 (2014).
148. Lipomi, D. J. *et al.* Electronic Properties of Transparent Conductive Films of PEDOT:PSS on Stretchable Substrates. *Chem. Mater.* **24**, 373–382 (2012).
149. Moulton, J. & Smith, P. Gel Processing of Electrically Conductive Blends of Poly (3-octylthiophene) and Ultrahigh Molecular Weight Polyethylene. *J. Polym. Sci. Part B ...* **30**, 871–878 (1992).
150. Pyridal, R. *et al.* Regioregular Pyridal[2,1,3]thiadiazole  $\pi$  -Conjugated Copolymers. 18538–18541 (2011).
151. O'Connor, B. *et al.* Anisotropic structure and charge transport in highly strain-aligned regioregular poly(3-hexylthiophene). *Adv. Funct. Mater.* **21**, 3697–3705 (2011).
152. Gargi, D. *et al.* Charge Transport in Highly Face-On Poly ( 3-hexylthiophene ) Films. (2013).
153. Clark, J., Chang, J. F., Spano, F. C., Friend, R. H. & Silva, C. Determining exciton bandwidth and film microstructure in polythiophene films using linear absorption spectroscopy. *Appl. Phys. Lett.* **94**, 2007–2010 (2009).
154. Stafford, C. M. *et al.* A buckling-based metrology for measuring the elastic moduli of polymeric thin films. *Nat. Mater.* **3**, 545–550 (2004).
155. Heriot, S. Y. & Jones, R. a L. An interfacial instability in a transient wetting layer leads to lateral phase separation in thin spin-cast polymer-blend films. *Nat. Mater.* **4**, 782–786 (2005).
156. Awartani, O. M. *et al.* Anisotropic Elastic Modulus of Oriented Regioregular Poly(3-hexylthiophene) Films. *Macromolecules* **49**, 327–333 (2015).
157. Stafford, C. M. *et al.* Elastic Moduli of Ultrathin Amorphous Polymer Films. 5095–5099 (2006).
158. Wu, H.-C. *et al.* A Rapid and Facile Soft Contact Lamination Method: Evaluation of Polymer Semiconductors for Stretchable Transistors. *Chem. Mater.* **26**, 4544–4551 (2014).
159. Xue, X. *et al.* Oriented Liquid Crystalline Polymer Semiconductor Films with Large Ordered Domains. *ACS Appl. Mater. Interfaces* **7**, 26726–26734 (2015).
160. *Certain commercial equipment or materials are identified in this paper in order to specify the experimental procedure adequately. Such identification is not intended to*

*imply recommendation or endorsement by the National Institute of Standards and Technol.*

161. Leterrier, Y. Mechanical integrity of thin films on flexible substrates. *Training* 1–11 (2006).
162. Balar, N. & O'Connor, B. T. Correlating Crack Onset Strain and Cohesive Fracture Energy in Polymer Semiconductor Films. *Macromolecules* acs.macromol.7b01282 (2017). doi:10.1021/acs.macromol.7b01282
163. Ha, J. S., Kim, K. H. & Choi, D. H. 2,5-bis(2-octyldodecyl)pyrrolo[3,4-c]pyrrole-1,4-(2H,5H)-dione-based donor-acceptor alternating copolymer bearing 5,5'-Di(thiophen-2-yl)-2,2'-biselenophene exhibiting 1.5 cm<sup>2</sup>V<sup>-1</sup>s<sup>-1</sup> hole mobility in thin-film transistors. *J. Am. Chem. Soc.* **133**, 10364–10367 (2011).
164. Li, Y., Sonar, P. & Singh, S. Annealing-Free High-Mobility Diketopyrrolopyrrole–Quaterthiophene Copolymer for Solution-Processed Organic Thin Film Transistors. *J. Am. Chem. Soc.* 2198–2204 (2011). doi:10.1021/ja1085996
165. Sun, B. *et al.* Dramatically enhanced molecular ordering and charge transport of a DPP-based polymer assisted by oligomers through antiplasticization. *J. Mater. Chem. C* **1**, 4423–4426 (2013).
166. Printz, A. D., Zaretski, A. V., Savagatrup, S., Chiang, A. S. C. & Lipomi, D. J. Yield Point of Semiconducting Polymer Films on Stretchable Substrates Determined by Onset of Buckling. *ACS Appl. Mater. Interfaces* **7**, 23257–23264 (2015).
167. Young Oh, J. *et al.* Intrinsically stretchable and healable semiconducting polymer for organic transistors. *Nat. Publ. Gr.* **539**, 411–415 (2016).
168. Berdichevsky, Y., Khandurina, J., Guttman, A. & Lo, Y. H. UV/ozone modification of poly(dimethylsiloxane) microfluidic channels. *Sensors Actuators, B Chem.* **97**, 402–408 (2004).
169. Efimenko, K., Wallace, W. E. & Genzer, J. Surface Modification of Sylgard-184 Poly(dimethyl siloxane) Networks by Ultraviolet and Ultraviolet/Ozone Treatment. *J. Colloid Interface Sci.* **254**, 306–315 (2002).
170. Özçam, A. E., Efimenko, K. & Genzer, J. Effect of ultraviolet/ozone treatment on the surface and bulk properties of poly(dimethyl siloxane) and poly(vinylmethyl siloxane) networks. *Polym. (United Kingdom)* **55**, 3107–3119 (2014).
171. Chan, E. P. & Crosby, A. J. Spontaneous formation of stable aligned wrinkling patterns. *Soft Matter* **2**, 324 (2006).
172. Oláh, A., Hillborg, H. & Vancso, G. J. Hydrophobic recovery of UV/ozone treated poly(dimethylsiloxane): Adhesion studies by contact mechanics and mechanism of surface modification. *Appl. Surf. Sci.* **239**, 410–423 (2005).
173. Hillborg, H., Tomczak, N., Oláh, A., Schönherr, H. & Vancso, G. J. Nanoscale hydrophobic recovery: A chemical force microscopy study of UV/ozone-treated cross-linked poly(dimethylsiloxane). *Langmuir* **20**, 785–794 (2004).

174. Kendall, K. Thin-film peeling-the elastic term. *J. Phys. D. Appl. Phys.* **8**, 1449–1452 (1975).
175. Kim, H., Yoon, B., Sung, J., Choi, D.-G. & Park, C. Micropatterning of thin P3HT films via plasma enhanced polymer transfer printing. *J. Mater. Chem.* **18**, 3489 (2008).
176. B efahy, S. *et al.* Thickness and elastic modulus of plasma treated PDMS silica-like surface layer. *Langmuir* **26**, 3372–3375 (2010).
177. Ouyang, M., Yuan, C., Muisener, R. J., Boulares, A. & Koberstein, J. T. Conversion of some siloxane polymers to silicon oxide by UV/ozone photochemical processes. *Chem. Mater.* **12**, 1591–1596 (2000).
178. Lee, D., Barber, J. R. & Thouless, M. D. Indentation of an elastic half space with material properties varying with depth. *Int. J. Eng. Sci.* **47**, 1274–1283 (2009).
179. Pan, K., Ni, Y., He, L. & Huang, R. Nonlinear analysis of compressed elastic thin films on elastic substrates: From wrinkling to buckle-delamination. *Int. J. Solids Struct.* **51**, 3715–3726 (2014).
180. Read, D. T. & Volinsky, A. a. Measurements for mechanical reliability of thin films \*. *Meas. Mech. Reliab. Thin Film.* 337–358 (2009).
181. Liu, F. *et al.* Efficient polymer solar cells based on a low bandgap semi-crystalline DPP polymer-PCBM blends. *Adv. Mater.* **24**, 3947–3951 (2012).